

**Monolithic Scintillator Detectors  
for High-Resolution  
Positron Emission Tomography**

**Cover:**

Artist's impression of the process of PET imaging, showing the two main components of the detectors described in this thesis: a trapezoidal monolithic  $\text{LYSO}:\text{Ce}^{3+}$  crystal and an APD array. A stylised PET-CT image of the rat is visible through the crystal.

*Model: Nikki*

*Design: C. D. Rans*

The research presented in this thesis was performed at the Radiation Detection & Matter (RDM) section of the department of Radiation, Radionuclides & Reactors ( $\text{R}^3$ ), Faculty of Applied Sciences, Delft University of Technology, Delft, The Netherlands.

Visiting address: Mekelweg 15, 2629 JB Delft, The Netherlands.

# **Monolithic Scintillator Detectors for High-Resolution Positron Emission Tomography**

## **Proefschrift**

ter verkrijging van de graad van doctor  
aan de Technische Universiteit Delft,  
op gezag van de Rector Magnificus prof. dr. ir. J.T. Fokkema,  
voorzitter van het College voor Promoties,  
in het openbaar te verdedigen op maandag 10 november 2008 om 12:30 uur

door  
Marnix Christiaan MAAS

natuurkundig ingenieur  
Technische Universiteit Delft  
geboren te Utrecht

*Dit proefschrift is goedgekeurd door de promotoren:*

Prof. dr. ir. C.W.E. van Eijk,

Prof. dr. F.J. Beekman.

*Copromotor:*

Dr. D.R. Schaart.

*Samenstelling promotiecommissie:*

Rector Magnificus,	voorzitter
Prof. dr. ir. C.W.E. van Eijk,	Technische Universiteit Delft, promotor
Prof. dr. F.J. Beekman,	Technische Universiteit Delft, promotor
Dr. ir. D.R. Schaart,	Technische Universiteit Delft, copromotor
Prof. dr. A.M.J. Paans,	Rijksuniversiteit Groningen
Prof. dr. M.B. van Herk,	Universiteit van Amsterdam
Prof. dr. S. Taverier,	Vrije Universiteit Brussel, België
Prof. dr. W. J. Niessen,	Technische Universiteit Delft
Prof. dr. ir. T.H.J.J. van der Hagen,	Technische Universiteit Delft, reservelid

Copyright © 2008 M.C. Maas and IOS Press

All rights reserved. No part of this book may be reproduced, stored in a retrieval system, or transmitted, in any form or by any means, without prior permission from the publisher.

ISBN: 978-1-58603-935-6

Keywords: Monolithic scintillator detectors, avalanche photodiode (APD) arrays, depth-of-interaction (DOI) correction, positron emission tomography (PET)

*Published and distributed by IOS Press under the imprint Delft University Press*

*Publisher*

IOS Press

Nieuwe Hemweg 6b

1013 BG Amsterdam

The Netherlands

tel: +31-20-688 3355

fax: +31-20-687 0019

email: [info@iospress.nl](mailto:info@iospress.nl)

[www.iospress.nl](http://www.iospress.nl)

[www.dupress.nl](http://www.dupress.nl)

## LEGAL NOTICE

The publisher is not responsible for the use which might be made of the following information.

PRINTED IN THE NETHERLANDS

*to my parents and sister,  
in loving memory of my grandparents*



# Contents

<b>1</b>	<b>Introduction</b>	<b>1</b>
1.1	Molecular imaging and PET . . . . .	1
1.1.1	Multi-modality imaging . . . . .	2
1.2	PET imaging . . . . .	4
1.2.1	Imaging principles . . . . .	4
1.2.2	Image quality and scanner performance . . . . .	6
1.3	Small animal PET imaging . . . . .	9
1.4	Research objectives . . . . .	10
1.5	Thesis outline . . . . .	11
<b>2</b>	<b>PET detectors</b>	<b>13</b>
2.1	Introduction . . . . .	13
2.2	Scintillators . . . . .	14
2.3	Photodetectors . . . . .	17
2.3.1	Photomultiplier tubes . . . . .	17
2.3.2	Avalanche photodiodes . . . . .	19
2.4	Existing animal PET systems . . . . .	21
2.4.1	Early developments . . . . .	21
2.4.2	MicroPET . . . . .	22
2.4.3	ClearPET . . . . .	24
2.4.4	APD-based systems . . . . .	25
2.5	Monolithic Scintillator Detectors . . . . .	27
<b>3</b>	<b>Materials and methods</b>	<b>31</b>
3.1	Introduction . . . . .	31
3.2	Hardware description . . . . .	31
3.3	Detector performance measurements . . . . .	35
3.3.1	Spatial resolution . . . . .	35

3.3.2	Energy resolution . . . . .	37
3.3.3	Timing resolution . . . . .	37
<b>4</b>	<b>Detector performance</b>	<b>39</b>
4.1	Introduction . . . . .	40
4.2	Materials and Methods . . . . .	40
4.2.1	Crystals . . . . .	40
4.2.2	Energy resolution . . . . .	42
4.2.3	Timing resolution . . . . .	42
4.2.4	Spatial resolution . . . . .	42
4.3	Results & Discussion . . . . .	44
4.3.1	Energy resolution . . . . .	44
4.3.2	Timing resolution . . . . .	46
4.3.3	Spatial resolution . . . . .	46
4.4	Conclusions . . . . .	53
<b>5</b>	<b>Signal to noise ratio</b>	<b>55</b>
5.1	Introduction . . . . .	56
5.2	Models . . . . .	57
5.2.1	Energy resolution . . . . .	57
5.2.2	Equivalent noise charge . . . . .	58
5.2.3	Timing resolution . . . . .	59
5.2.4	Spatial resolution . . . . .	60
5.3	Materials . . . . .	62
5.3.1	Crystals . . . . .	62
5.3.2	LAAPD . . . . .	62
5.3.3	APD arrays . . . . .	63
5.4	Methods . . . . .	65
5.4.1	Scintillation photon variance . . . . .	65
5.4.2	LAAPD energy resolution . . . . .	65
5.4.3	APD arrays . . . . .	67
5.5	Results and discussion . . . . .	68
5.5.1	Scintillation photon variance . . . . .	68
5.5.2	LAAPD energy resolution . . . . .	69
5.5.3	APD arrays . . . . .	69
5.6	Conclusions . . . . .	79



<b>6</b>	<b>Model analysis of the detector PSF</b>	<b>81</b>
6.1	Introduction . . . . .	82
6.2	Point spread function models . . . . .	82
6.2.1	Detector PSF . . . . .	82
6.2.2	Influence of test beam diameter . . . . .	85
6.2.3	Background . . . . .	86
6.2.4	PSF model summary . . . . .	86
6.3	Materials and methods . . . . .	87
6.3.1	Detector . . . . .	87
6.3.2	PSF measurements . . . . .	88
6.3.3	Simulation of photon beam and intra-crystal scattering . .	89
6.3.4	Fitting procedure . . . . .	90
6.4	Results . . . . .	90
6.4.1	Detector PSF . . . . .	91
6.4.2	Influence of test beam diameter . . . . .	91
6.4.3	Model validation . . . . .	93
6.4.4	Signal to noise ratio . . . . .	95
6.4.5	Discussion . . . . .	96
6.5	Conclusions . . . . .	98
<b>7</b>	<b>Simulated scanner performance</b>	<b>101</b>
7.1	Introduction . . . . .	102
7.2	Methods . . . . .	103
7.2.1	Monte Carlo simulations . . . . .	103
7.2.2	Intrinsic detector PSF . . . . .	105
7.2.3	Scanner performance . . . . .	105
7.3	Results . . . . .	107
7.3.1	Spatial resolution . . . . .	107
7.3.2	Sensitivity . . . . .	110
7.3.3	Count rate performance . . . . .	110
7.4	Discussion . . . . .	111
7.5	Conclusions . . . . .	114
<b>8</b>	<b>General discussion</b>	<b>115</b>
<b>A</b>	<b>Characterisation of setup components</b>	<b>119</b>
A.1	APD arrays . . . . .	119
A.2	Preamplifiers . . . . .	120
A.3	Shaping amplifiers . . . . .	123

A.3.1	Linearity . . . . .	123
A.3.2	Gain dispersion . . . . .	124
A.3.3	Offset . . . . .	124
A.3.4	Shaping constants . . . . .	125
A.4	Multichannel ADCs . . . . .	127
<b>B</b>	<b>Positioning algorithm</b>	<b>129</b>
B.1	Algorithm optimisation . . . . .	129
B.1.1	Number of nearest neighbours . . . . .	129
B.1.2	Number of reference events . . . . .	130
B.2	Resolution uncertainty . . . . .	130
<b>C</b>	<b>Equivalent noise charge of the fast amplifier branch</b>	<b>133</b>
	<b>Bibliography</b>	<b>135</b>
	<b>Nomenclature</b>	<b>147</b>
	<b>Summary</b>	<b>151</b>
	<b>Samenvatting</b>	<b>155</b>
	<b>Acknowledgements</b>	<b>161</b>
	<b>Curriculum Vitae</b>	<b>165</b>

# Chapter 1

## Introduction

### 1.1 Molecular imaging and PET

Molecular imaging techniques enable the visualisation of biological processes in living organisms. These techniques rely on synthetic biomolecules ('tracers') that specifically target a physiological process of interest without significantly disturbing it, and that possess some property which allows them to be detected externally. If the detectable property is radioactivity, the molecules are referred to as radiotracers, and the imaging technique is referred to as nuclear imaging.

Positron emission tomography (PET) is such a nuclear imaging technique. The tracers used for this technique are labelled with radioactive isotopes emitting positrons (anti-electrons). The word tomography is composed of the Greek words 'tomos', meaning 'slice', and 'graphein', meaning 'to write'. In short, PET makes images of slices of a subject, using emission of positrons. The positron-emitting radiotracer is injected into the subject and accumulates in the areas of interest. The radiation emanating from the subject is then collected and is used to calculate an image of the activity concentration of the radionuclide.

Various molecular imaging techniques exist aside from PET, each with specific applications and possibilities. Another widely used nuclear imaging technique is Single Photon Emission Computed Tomography (SPECT); other, non-nuclear techniques include optical fluorescence imaging and Magnetic Resonance Imaging (MRI) with molecular contrast agents. Compared to SPECT and MRI, PET has a high sensitivity, allowing the detection of very small concentrations of the tracer. Clinical PET systems furthermore offer a higher spatial resolution than clinical SPECT systems.

PET studies are frequently used in oncology to identify primary tumours and

metastases. Quantitative imaging of the uptake of glucose in the tumour using the  $^{18}\text{F}$ -labelled glucose analogue 2-fluoro-2-deoxy-D-glucose (FDG) provides information on tumour growth and internal structure. This information can be used to determine a treatment strategy and to evaluate therapeutic response. In cardiology, PET can be used for the detection of coronary artery disease by measurement of myocardial blood flow and perfusion. Furthermore, it is an established method for identifying recoverable myocardial tissue in damaged regions of the heart. In neurology, PET is an important tool in the detection and diagnosis of e.g. Alzheimer's disease, Parkinson's disease and epilepsy. In addition to these examples, PET is routinely used in a broad diversity of other clinical applications.

PET also plays an increasingly important role in molecular biology research and drug development. This type of research often involves laboratory animals such as non-human primates, rats and mice. An advantage of PET in this context is that the distribution of a radiotracer can be followed as a function of time in a single living animal, allowing the investigation of the kinetics of biomolecules *in vivo*. The same animal can furthermore be used at a later stage to follow disease models and interventions over extended periods of time, eliminating variability due to inter-animal differences. In contrast, more traditional invasive techniques such as autoradiography involve killing and sectioning multiple animals. The number of animals used in PET experiments can thus be greatly reduced compared to such techniques. PET can be used to investigate a wide range of biological processes, owing to the large variety of available positron-emitting radiotracers. The same type of experiments can be performed on animals and humans using PET, facilitating direct comparison of animal models of disease with humans.

This thesis focuses on a new type of detector for high-resolution PET.

### 1.1.1 Multi-modality imaging

Although PET and SPECT images provide valuable information on physiological processes, they do not provide detailed information on the anatomy of the patient or subject. If such information is needed also, for example in the identification of tumour volumes, the functional PET or SPECT images need to be combined with morphological images created by e.g. X-ray Computed Tomography (CT) or MRI. This can be achieved by correlating the functional and the morphological images using software registration techniques.

Excellent results can be achieved using these software registration techniques, which are however limited by small differences in the anatomy and setup of the subject between the different scans. These differences can be reduced using integrated multi-modality (e.g. PET-CT or SPECT-CT) imaging systems. The first

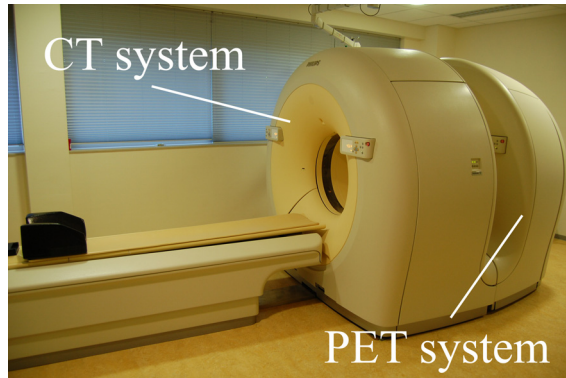


Figure 1.1: A modern PET-CT scanner, providing access to the patient between the CT subsystem (front) and the PET subsystem (back) (Philips Gemini TF, Philips Medical Systems, Best, The Netherlands).

PET-CT system for clinical use was installed in 1998 [1]. A few years later, the first PET-CT and SPECT-CT systems became commercially available, and currently the majority of PET systems sold have an integrated CT scanner. These systems are commonly set up with one common scanner axis, permitting positioning of the patient in either scanner by a translation of the patient couch (see Fig. 1.1). In addition to providing accurate anatomical information with the functional images, the CT images can be used to apply a correction for attenuation and scattered events in the PET images (see Section 1.2.2).

Combined small-animal PET-CT scanners have recently also become available. Fig. 1.2a shows a PET image acquired with such a system (Siemens Inveon Preclinical PET/CT, Siemens Medical Solutions, Erlangen, Germany), of a mouse with a subcutaneous human colonic tumour. The image was created by injecting the mouse with a bispecific pre-targeting antibody targeting the tumour, followed after several days by a  $^{68}\text{Ga}$ -labelled peptide binding with the antibody. Fig. 1.2b shows the corresponding CT image, and Fig. 1.2c the fused PET-CT image.

Integrated PET-MRI systems are not yet commercially available due to the much greater technical challenges associated with this combination compared to PET-CT. However, prototype MRI-compatible PET inserts have been developed for small-animal imaging, and promising results have been obtained with these systems [2–4]. One of the motivations for the development of a PET-MRI system is the superior and flexible contrast for soft tissue of MRI compared to CT. The combination of PET with MRI additionally permits the simultaneous acquisi-

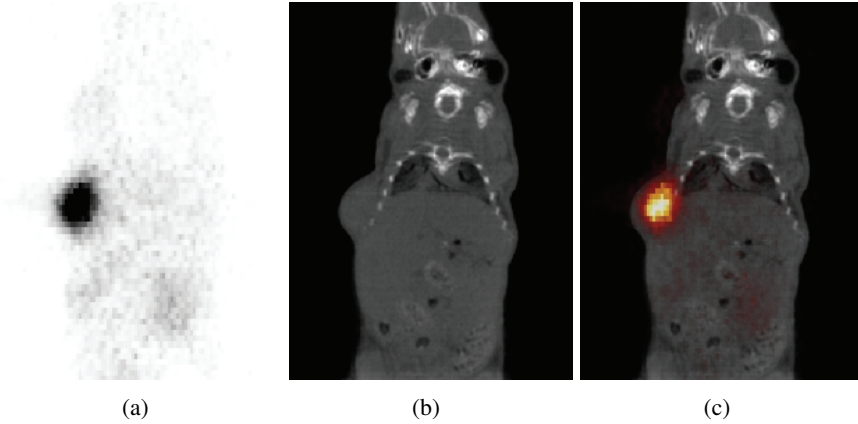


Figure 1.2: (a) PET image of a mouse with a subcutaneous tumour created using a  $^{68}\text{Ga}$ -labelled peptide, (b) corresponding CT image, and (c) fused PET-CT image. *Images courtesy of P. Laverman, UMCN St. Radboud, Nijmegen, The Netherlands. Printed with permission.*

tion of dual-modality functional information, e.g. by combining PET with blood-oxygen level dependent (BOLD) MRI or MR spectroscopic imaging (MRSI).

## 1.2 PET imaging

### 1.2.1 Imaging principles

A PET exam starts with the injection of the radiotracer into the blood stream of the subject. The tracer is distributed within the subject, accumulating in the targeted areas. The radionuclides disintegrate, emitting positrons. When emitted, a positron travels a certain distance through the surrounding tissue, losing energy along its path. When it has lost sufficient energy, the positron annihilates with an electron, giving rise to the emission of two annihilation photons with an energy of 511 keV, travelling in nearly opposite directions. This process is illustrated in Fig. 1.3a. The photons are then detected by radiation detectors surrounding the subject, see Fig. 1.3b. The coincident detection of the pair of annihilation photons defines the line along which the annihilation must have taken place: the line of response (LOR). A collection of many such LORs can be used to reconstruct the spatial distribution of the radiopharmaceutical.

Most PET scanners consist of one or more rings of detector modules. The

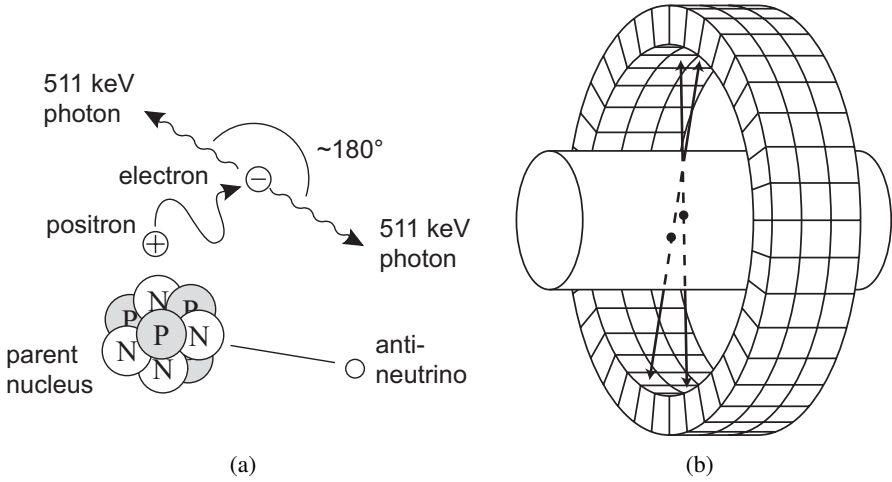


Figure 1.3: Imaging principles of positron emission tomography: positron emission and annihilation (a) and a PET scanner with example lines of response (LORs) (b).

detector modules commonly consist of a 2-dimensional (2D) matrix of scintillator crystal segments coupled to one or more – possibly position-sensitive – photosensors (see also Section 2.4). The energy of the incident 511 keV photons is converted into photons in the ultraviolet (UV) and visible range of light in the scintillator. These photons are then detected by the photosensor(s). In this common crystal-matrix design, each ring of modules can be considered to contain several detector rings, each consisting of many individual crystal elements. An example of such a design is the ECAT EXACT HR scanner (CTI-Siemens, Knoxville, TN, USA), which consists three rings of modules, where each module ring contains 8 rings of 784 crystal elements [5].

In PET data acquisition, a distinction is made between two modes of operation: 2D mode and 3D mode. In 2D mode, coincidences are only recorded between detector elements within the same ring or closely neighbouring rings. In 3D mode, coincidences between detector elements in any combination of rings are recorded. Systems operating in 2D mode often use thin plates of lead or tungsten (‘septa’) between the detector rings to reduce the effect of scattered and random coincidences (see Section 1.2.2). Image reconstruction in 2D mode is considerably simpler and faster than in 3D mode. However, 3D mode has the advantage of a much higher sensitivity compared to 2D mode, resulting in an improved image quality and shorter acquisition times.

Many different methods are available for reconstructing the collected data into an image. These methods are commonly categorised into analytical and iterative methods. The most common analytical method in 2D mode is the filtered backprojection (FBP) algorithm, and its 3D analogue is known as the 3D reprojection with filtered backprojection (3D-RP) algorithm. To reduce the calculation times required by 3D-RP, an adaptation of this method known as Fourier Rebinning (FORE) was developed later, finding widespread use [6]. Although these analytical methods are relatively simple to implement and fast, they have the drawbacks of being based on an oversimplified model of photon transport and detection processes and amplifying image noise.

To overcome these issues, iterative methods using models of statistics, blurring and attenuation effects in the image formation process have been developed. More accurate results can be obtained with these algorithms compared to analytical methods, at the expense of a significantly increased computation cost. Popular examples of such algorithms are maximum likelihood expectation maximisation (MLEM) [7] and ordered subsets expectation maximisation (OSEM) [8] and their variations. Many other methods have been, and are continuing to be developed.

### **1.2.2 Image quality and scanner performance**

The quality of a PET image can be described in terms of its spatial resolution and its signal to noise ratio. This section describes the factors determining these two parameters and the way they relate to scanner performance characteristics.

#### **Image spatial resolution**

The image spatial resolution represents the size of the spatial features that can be distinguished. It depends on the design of the scanner and its detectors and on the image reconstruction algorithm used. This dependence on the reconstruction algorithm complicates direct comparison between different PET systems. Therefore, reference is often made throughout this work to the ‘system resolution’, defined as the image resolution that can be obtained using a standard filtered backprojection (FBP) algorithm with a ramp filter with the cutoff at the Nyquist frequency.

One of the most important factors determining the image spatial resolution is the intrinsic spatial resolution of the detectors. Most scanners currently use detectors containing matrices of individual crystal segments (see Chapter 2), and the dimensions of these segments thus play an important role in the spatial resolution of the PET image.



Table 1.1: Maximum energy and width of the 1-D end point distribution for positron point sources of several commonly used PET isotopes. (Data from [9])

Isotope	$E_{max}$ (MeV)	FWHM (mm)	FWTM (mm)
$^{18}\text{F}$	0.635	0.102	1.03
$^{11}\text{C}$	0.970	0.188	1.86
$^{13}\text{N}$	1.190	0.282	2.52
$^{15}\text{O}$	1.720	0.501	4.14

The image resolution is fundamentally limited by the physics of positron decay and annihilation. A positron emitted by a radioisotope travels a certain distance before annihilating with an electron in the surrounding material. This distance depends on the material in which the positron travels and on its initial energy, which depends on the emitting isotope. The radial distribution of annihilation points around the position of positron emission in a homogeneous medium is sharply peaked and isotropic. The blurring effect caused by the positron range in any direction of the final image can be described by the 1-dimensional (1D) histogram of this distribution. The full width at half maximum (FWHM) and full width at tenth maximum (FWTM) of such histograms are listed for several commonly used PET isotopes in water in Table 1.1 [9]. The positron range effect sets a fundamental limit on the spatial resolution attainable in a PET image.

When a positron and an electron annihilate, their combined center of mass may have a residual momentum with respect to the laboratory coordinate system. As the total momentum is preserved in the annihilation process, a slight deviation from  $180^\circ$  in the angle between the paths of the two annihilation photons may occur. The angular uncertainty in the direction of the two 511 keV photons resulting from this effect is on the order of a few mrad, depending on the material [10, 11]. This photon non-collinearity has a blurring effect on the final image that increases with increasing scanner diameter.

An additional degradation of the image spatial resolution occurs due to an effect referred to as parallax error. When a 511 keV photon deposits its energy in a detector crystal, a single point of interaction is assigned to it by the system, e.g. the centre of the front surface of the crystal. For obliquely incident photons, this may result in a mispositioning of the LOR, see Fig. 1.4, resulting in radial blurring in the reconstructed image. The effect increases with increasing distance to the central scanner axis, because more photons enter the crystals at oblique angles on average at those positions. Parallax errors can be reduced if the detectors provide a way of estimating the depth of interaction (DOI) inside the crystals.

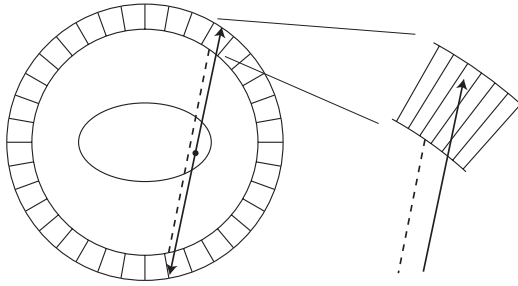


Figure 1.4: Illustration of the parallax effect. Without depth of interaction information, errors in LOR positioning may occur at off-centre source positions.

### Scanner sensitivity

The signal to noise ratio (SNR) in an image voxel determines the accuracy of the estimate of the activity concentration in that voxel. It depends on the SNR of the measured data and on the image reconstruction method used [12–14]. Given the noise properties of the detectors, the SNR of the measured data can be improved by increasing the number of detected coincident events. To obtain the highest image SNR in the shortest amount of time, a PET scanner should therefore have a high sensitivity, which can be defined as the ratio of the number of coincident counts registered per second in a particular volume, to the true number of radioactive decays per second in the same volume.

A high efficiency of the detectors is essential for a high scanner sensitivity, because the efficiency for coincident detection is proportional to the square of the efficiency of a single detector. Furthermore, the scanner sensitivity improves with increasing geometric efficiency, i.e., with increasing solid angle coverage of the field of view (FOV). This can be achieved by reducing the scanner diameter and increasing its axial extent. However, reducing the scanner diameter will also aggravate the effects of parallax errors, causing a tradeoff between scanner sensitivity and image resolution.

### Count rate performance

When an event is registered by the PET scanner's coincidence electronics, this can be due to any of three types of events, illustrated in Fig. 1.5. When both 511 keV photons resulting from a single nuclear decay are detected in two opposite detectors without being scattered, this is referred to as a true coincidence. When one or both of the photons undergo Compton scattering within the subject before

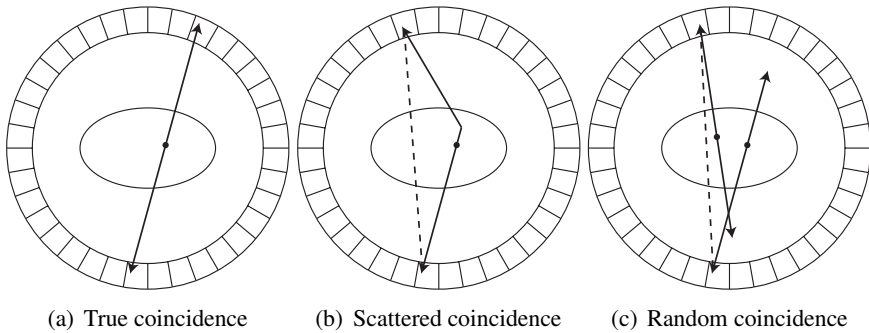


Figure 1.5: Three possible types of coincidences in a PET scanner

being registered in the detectors, the event is classified as a scattered coincidence. A third type of coincidence may occur when two almost simultaneous nuclear decays take place, and one annihilation photon from each decay is registered in a detector while the other two photons are not. If the two photons are detected closely enough in time to appear simultaneous to the system electronics, they are registered as a coincident event, referred to as a random coincidence.

A commonly used characteristic of PET scanner performance is the noise equivalent count rate (NECR) [15], which describes the ability of the system to distinguish between true, scattered and random coincidences. The rate of true, scattered and random coincidences depends on the system, on the subject, and on the activity within the subject. The NECR can be used to determine the maximum useful activity for a particular subject: the highest NECR is usually obtained at a lower activity than the one corresponding to the highest true coincidence count rate. Furthermore, the NECR can serve as a comparison between different scanners. This can however only be done using standardised phantoms and protocols, as the NECR is subject dependent [16].

### 1.3 Small animal PET imaging

PET is increasingly being used for pre-clinical studies on small animals such as rats and mice. Development of dedicated small-animal PET systems requires facing a number of challenges related to the small size of these animals.

To obtain a similar level of detail in mice as in humans, the ratio between the body masses of the subjects and the image volumetric resolutions (defined as the product of the resolutions in the three orthogonal image directions) should be

roughly equal. An average human weighs approximately 7 kg, and the image resolution in a typical human PET image is  $< 5$  mm in all directions, corresponding to a volumetric resolution of  $< 0.125$  ml. A mouse typically weighs approximately 30 g, implying that a volumetric resolution of  $0.05 \mu\text{l}$  would be desirable for this case. This corresponds to an image resolution of approximately 0.4 mm in all orthogonal directions. So far, such resolutions have not yet been achieved in small animal PET. Sub-millimetre image resolutions have however been reported [17]. This was achieved both by using detectors with a very high spatial resolution, and by using advanced iterative reconstruction methods.

To obtain a similar SNR per voxel per time frame as in human studies, the number of events registered per unit volume per time frame in a mouse study should be increased proportionally to the reduction in voxel volume, typically a factor  $\sim 1000$ . This can be achieved by increasing the activity per unit body mass injected into the mouse; however, there are limitations to this approach. Firstly, reliable data can only be obtained if the tracer concentration is low enough to not significantly perturb the biological process under investigation. Secondly, the maximum volume that can be safely injected is limited to only  $\sim 1$  ml, as the blood volume of a mouse is only  $\sim 25$  ml. In spite of these limitations, activity concentrations of more than 1000 MBq/kg body mass are used in mice (in a typical human FDG-PET scan, this is approximately 3 MBq/kg). Typically, only a few percent of the injected activity is detected by current small-animal PET systems (see Section 2.4). Increasing the scanner sensitivity by increasing the detector efficiency and solid angle coverage of the FOV may therefore contribute significantly to an improved image quality.

As a final challenge, a small-animal PET system should be able to process the high count rates associated with the high activity concentrations and high sensitivity needed to create high quality images. Its detectors should therefore have good timing characteristics, and its system electronics should have a short dead time.

## 1.4 Research objectives

The above discussion indicates that detectors for PET should meet a range of different requirements in order to provide a good image quality. The research presented in this thesis focuses on a new type of detectors, meant to provide the highest scanner sensitivity possible while still providing a spatial resolution adequate for high-resolution imaging. The detectors consist of a monolithic piece of scintillation material, coupled on one or more sides to position sensitive avalanche

photodiode (APD) arrays [18, 19]. The position of 511 keV photons incident on the detector is estimated from the distribution of scintillation light on the APD array(s) produced in their interactions with the crystal.

Most PET scanners currently use detectors consisting of matrices of scintillation crystals separated by some reflective material, coupled to photomultiplier tubes (PMTs). The monolithic design of the detectors presented in this thesis avoids the dead volume occupied by reflective materials, improving the detection efficiency over segmented designs. Furthermore, the compactness of the APD arrays allows placing the detectors closely together, necessary for a high scanner sensitivity. Finally, the operation of the APD arrays is not strongly affected by the presence of magnetic fields, providing an opportunity to combine a PET scanner based on these devices with an MRI scanner.

The aims of the research presented in this thesis were (1) to determine experimentally the spatial resolution, energy resolution and time resolution attainable with monolithic scintillator detectors, (2) to analyse the dependence of these detector properties on physical quantities such as the scintillator light yield, the APD gain and the noise characteristics of the frontend electronics, and (3) to predict the performance of a small animal PET system based on these detectors.

## 1.5 Thesis outline

The research presented in this thesis is primarily based on experimental work on prototype detector modules. Simulation studies have been carried out in parallel; these are presented elsewhere [20]. Some of the results of these simulation studies are also used in this work.

An introduction to PET detectors is presented in **Chapter 2**. The performance characteristics of such detectors and their components are discussed. **Chapter 3** gives an overview of the hardware of detectors that have been used throughout this thesis, and describes an experimental setup that has been built to characterise them. It furthermore introduces the methods that have been used to measure the energy, timing and spatial resolution of the detectors. **Chapter 4** presents an overview of the performance of the detectors. The spatial resolution obtained with crystals in various readout geometries and with various surface finishes is investigated, and the intrinsic spatial resolution of these detectors is estimated by correcting the measurements for the finite width of the test beam. In addition, the ability of the detectors to correct for the depth-of-interaction (DOI) of the 511 keV photons is studied, and the energy and timing resolutions obtained with the detectors are presented. In **Chapter 5**, an analysis is presented of the influence of signal

variances on the detector energy, timing and spatial resolutions. This is done by modelling the signal to noise ratio (SNR) applicable to each of these detector characteristics in terms of physical quantities such as the scintillator light yield, the APD gain and the noise characteristics of the frontend electronics. **Chapter 6** describes an detailed analysis of the detector spatial resolution. A model is derived for the detector point spread function (PSF), describing the probability distribution of estimated entry points on the detector front surface, given a true entry point. A validation of this model is presented, and it is demonstrated how the model can be used to estimate the PSF of the detectors in response to a zero-width pencil beam (the intrinsic detector PSF), which describes the distribution of positioning errors exhibited by a detector in a PET system. A pilot study using Monte-Carlo simulations to investigate the performance of small-animal PET systems based on monolithic scintillator detectors is presented in **Chapter 7**. The simulations use experimentally determined PSFs and other detector characteristics as input. The image resolution, point source sensitivity and count rate performance of these systems are investigated. Finally, **Chapter 8** summarises the findings of the preceding chapters, and discusses the further steps that should be taken to develop a PET scanner prototype based on monolithic scintillator detectors.

# Chapter 2

## PET detectors

### 2.1 Introduction

As has been briefly introduced in the previous chapter, the detectors of a PET scanner strongly influence the image quality that can be attained with it. To describe the performance of PET detectors, four primary characteristics can be identified: the detector spatial resolution, the energy resolution, the time resolution and the detection efficiency. A high intrinsic spatial resolution of the detectors is needed to achieve a high spatial resolution in the PET image. For a good uniformity of the spatial resolution throughout the field of view, parallax errors should be minimised, implying for most detector designs that information on the depth of interaction (DOI) is needed. A high energy resolution of the detectors assures efficient discrimination between scattered events and true coincident events, and a high time resolution is needed for an effective rejection of random coincidences. A high efficiency for the detection of 511 keV photons is needed in order to achieve a high scanner sensitivity to true coincidences. For the same reason, the detectors should have a compact geometry, so that they can be placed closely together leaving as little dead area between the detectors as possible. One of the primary challenges in the advancement of PET technology lies in this wide variety of detector requirements, all of which should be met if a good scanner performance is to be obtained.

In addition to the primary requirements outlined above, a number of other aspects that are important in the detector design can be identified. For instance, combination of a PET system with other imaging modalities can be of great advantage because of the lack of anatomical information provided by PET. Combined PET-CT systems have recently been developed for this purpose and have quickly

gained widespread use [1]. In addition, increasing effort is being put into the development of combined PET-MRI systems, stimulated by the poor contrast for soft tissues provided by CT [3,4,21]. For this latter application, the PET detectors should on one hand be able to function in the strong and rapidly changing magnetic fields prevalent in MRI systems; on the other hand, the PET detectors should not disturb these fields in such a way that the MRI image quality is degraded.

Finally, the cost of fabrication, operation and maintenance of the PET detector modules should be as low as possible. They should be operable around room temperature, easily exchangeable in case of malfunction, and their performance should be stable in time.

Most designs investigated in the past to reach a suitable compromise between all of these requirements have been based on scintillation detectors. In such detectors, the incident radiation is absorbed and its energy converted into photons in the visible and ultraviolet range of light using a scintillator, usually a crystalline compound. The scintillation photons are then detected by a photosensitive device coupled to the scintillator. The detectors investigated in this thesis also consist of a scintillation crystal coupled to a photosensor, and the discussions in the remainder of this chapter are therefore limited to this type of detectors. It is noted, however, that other detector concepts have been, and are being investigated also [22–25].

In Section 2.2, the properties of scintillators relevant for their application in PET detectors are discussed. In Section 2.3, two photodetector types are introduced: photomultiplier tubes (PMTs), which are the most commonly used photodetectors in PET, and avalanche photodiodes (APDs), which are increasingly receiving attention as alternatives for PMTs. In Section 2.4, a brief outline of the development of high resolution PET detectors over the last years is presented, by reviewing several recent detector designs and their performance in PET systems. Finally, monolithic scintillator detectors – the focus of this thesis – are introduced in more detail in Section 2.5.

## 2.2 Scintillators

A scintillator is a material that upon interaction with a quantum of ionising radiation, converts its energy into photons in the visible and ultraviolet range of light. For a scintillation detector to provide a high signal to noise ratio (SNR), the scintillator should emit a large number of photons per absorbed radiation quantum, and the photosensor should detect a large fraction of these photons. The scintillator should thus have low self-absorption, and the wavelength range of the photons it emits should match with the sensitivity range of the photosensor. As an illus-



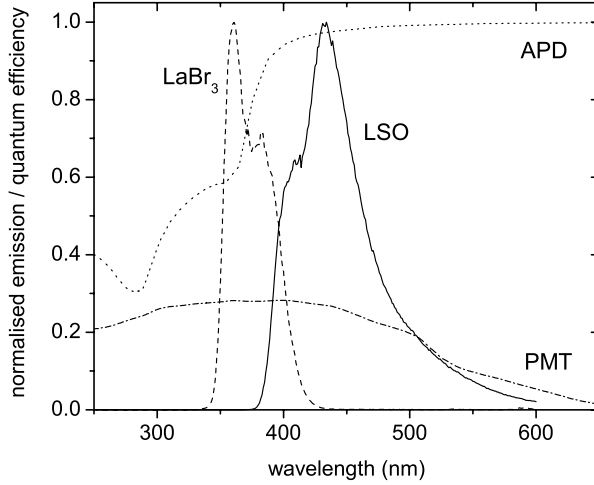


Figure 2.1: Emission spectra of LSO and  $\text{LaBr}_3$ , and quantum efficiency of a PMT (Hamamatsu R1791) and an APD (Advanced Photonix 630-70-72-510).

tration, X-ray excited emission spectra of two scintillators (LSO and  $\text{LaBr}_3$ ) and the detection quantum efficiencies of a PMT (Hamamatsu R1791) and an APD (Advanced Photonix 630-70-72-510) are shown as a function of the wavelength in Fig. 2.1. For good timing properties and suitability for high count rate applications such as PET, the scintillator should furthermore have short signal rise and decay times. For photosensors equipped with a protective window in front of the sensitive layer, the indices of refraction of the scintillator and the window should match as closely as possible, in order to minimise reflections at the crystal-window interface.

The efficiency of a photon detector is determined by the detector material and its thickness. The attenuation of a narrow photon beam in a piece of material is approximated by:

$$\frac{\Phi(x)}{\Phi(0)} = e^{-\mu x}, \quad (2.1)$$

where  $\Phi(0)$  and  $\Phi(x)$  are the photon flux at depth 0 and depth  $x$ , respectively, and  $\mu$  is the total linear attenuation coefficient, representing the sum of the attenuation coefficients for the different possible interaction mechanisms. At 511 keV, the

photon energy used in PET, the main interaction mechanisms are photoelectric absorption and Compton scattering. Hence:

$$\mu \approx \mu_p + \mu_C \quad \text{at 511 keV,} \quad (2.2)$$

where  $\mu_p$  and  $\mu_C$  are the linear attenuation coefficients for photoelectric absorption and Compton scattering, respectively.

The following proportionalities approximately hold for these two coefficients:

$$\mu_p \propto \rho Z^{3-4} \quad (2.3)$$

and

$$\mu_C \propto \rho, \quad (2.4)$$

where  $\rho$  is the density and  $Z$  is the atomic number of the material. From these expressions, it follows that a high detection efficiency can be obtained by choosing a scintillation material with a high density and a high atomic number. Furthermore, they show that the fraction of total interactions that occur by photoelectric absorption ('photo fraction') increases with increasing  $Z$ . This is important for PET detectors because the lower energy deposited in a Compton interaction compared to a photoelectric absorption results in a reduced signal to noise ratio. The secondary Compton photon may furthermore be detected elsewhere, e.g. in the same or in another detector, giving rise to an uncertainty in the positioning of the event. The relevance of this is illustrated by the observation that in Bismuth Germanate (BGO), a widely used PET scintillator based on the element bismuth which has an atomic number  $Z = 83$ , the photo fraction at 511 keV is only 40% [26].

In addition to the above requirements, the scintillation crystals should be relatively easy to grow and cut, and should preferably not be hygroscopic. Furthermore, the scintillator should not consist of elements which naturally contain radioactive isotopes in too high concentrations. Absorption of the radiation emitted by such isotopes within the scintillator can cause a natural background of events. An example is LSO, in which the lutetium naturally contains 2.6% of the isotope  $^{176}\text{Lu}$ . If the concentration of such isotopes is too high, they may give rise to a background of random coincidences in the PET system.

Summarising, the ideal PET scintillator emits a high number of optical photons per absorbed 511 keV photon at the right wavelength in a short time, has a high density, a high effective atomic number, no natural background radiation and is easy to grow and handle. The development of scintillation materials that combine as many of these properties as possible is an active field of research. The properties of several scintillation materials used in PET are summarised in

Table 2.1: Properties of several scintillators applied in PET. (Data from [26])

	NaI:Tl	BGO	LSO	LuAP	LaBr <sub>3</sub>
Material	NaI:Tl	Bi <sub>4</sub> Ge <sub>3</sub> O <sub>12</sub>	Lu <sub>2</sub> SiO <sub>5</sub> :Ce	LuAlO <sub>3</sub> :Ce	LaBr <sub>3</sub>
Light yield (ph/MeV)	41000	9000	26000	12000	61000
$\lambda_{max}$ (nm)	365	480	420	410	358
decay time (ns)	230	300	40	18	35
$\rho$ (g/cm <sup>3</sup> )	3.67	7.1	7.4	8.3	5.3
att. length 511 keV (cm)	29.1	10.4	11.4	10.5	21.3
$Z_{eff}$	50.8	75.2	66.3	64.9	46.9
Photo-fraction 511 keV (%)	17	40	32	30	13
Hygroscopic	yes	no	no	no	yes
Backgr. counts (cps/cm <sup>3</sup> )	—	—	240 <sup>1</sup>	—	—

<sup>1</sup> Data from [27]

Table 2.2. From these data, it is clear that none of these compounds has the best properties in every category. For example, the first PET scanners were constructed using the NaI(Tl) scintillator [28]. This crystal has a very high light yield, but its low density and effective atomic number limited the sensitivity of these scanners. Later designs employed the bismuth germanate (BGO) compound, which has a very high density and effective atomic number, resulting in detectors with a higher detection efficiency. However, the low light yield and relatively long scintillation decay time of this crystal make it less suitable for fast timing applications. The more recently developed cerium-doped compound lutetium oxyorthosilicate (LSO:Ce) [29] is the scintillator of choice for most modern high resolution PET scanners because of its favourable combination of high light yield, fast scintillation decay time and high density (see also Section 2.4).

## 2.3 Photodetectors

### 2.3.1 Photomultiplier tubes

Photomultiplier tubes (PMTs) are the most widely used photodetectors in emission tomography applications. Fig. 2.2 shows a schematic representation of a PMT. Scintillation photons incident on the PMT entrance window give rise to ionisations in the photocathode, causing the emission of primary electrons. These photoelectrons are focused by an electron-optical system and accelerated towards the first dynode by a strong electric field. Upon impact of an electron, the dynode emits several secondary electrons (typically  $\geq 6$  for the first dynode, and  $\sim 4$  at the following dynodes), which are then accelerated towards the next dynode, etcetera.

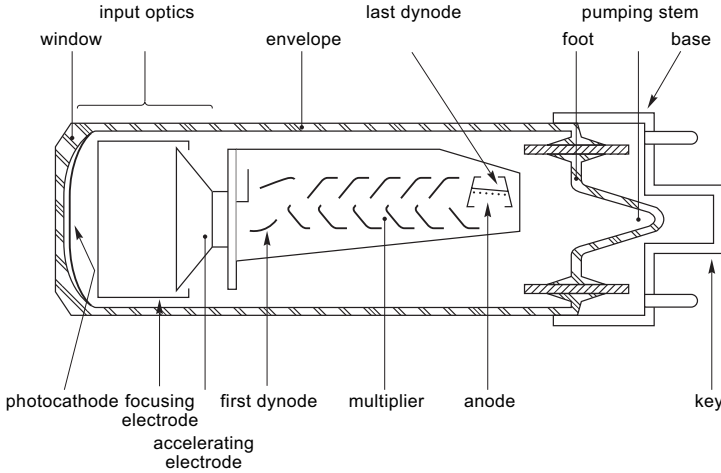


Figure 2.2: Schematic of a photomultiplier tube (adapted from Photonis, 2002, *Photomultiplier tubes: Principles and Applications*, with permission).

The electrons emitted from the final dynode are collected at the anode, producing the signal. The gains achieved in this way are of the order of  $10^6$ – $10^7$ .

The high gain of these devices can provide a good signal to noise ratio. PMTs furthermore have a fast signal rise time of typically 0.5–3 ns, making them suitable for timing applications such as PET. PMTs are stable in their operation and reliable.

A drawback of PMTs is their limited quantum efficiency (QE) of typically  $\sim 25\%$  (see Fig. 2.1), although PMTs with a QE of up to 43% have been developed recently [30]. Furthermore, the devices are bulky, making close packing of detector modules based on PMTs difficult. Finally, PMTs are very sensitive to magnetic fields, complicating their operation in close proximity to an MRI machine.

Position sensitive PMTs (PS-PMTs) are increasingly being used in high-resolution biomedical imaging applications. Various types of these devices have been developed, which have the common feature of having multiple anodes, providing information on the position of the detected scintillation light [31–33]. Their performance in terms of gain, quantum efficiency and rise time is comparable to that of conventional PMTs. Drawbacks of PS-PMTs are the large variation in gain between channels within the same device (typically 1:3 or 1:4) and their relatively high cost [31]. Furthermore, most designs have a relatively large dead area

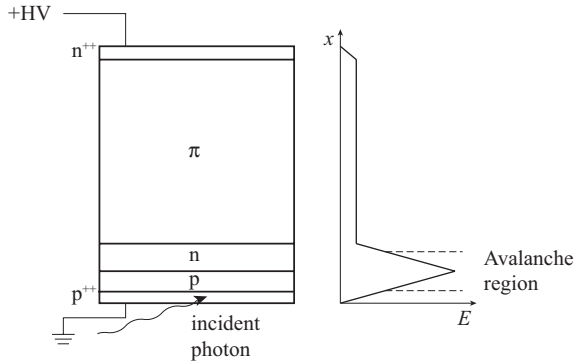


Figure 2.3: Schematic of a reverse reach-through APD

around the photocathode, although more compact devices have been developed recently [34].

### 2.3.2 Avalanche photodiodes

Avalanche photodiodes are increasingly being considered as photosensors for PET. These devices have a higher quantum efficiency (up to  $\sim 100\%$  [35]) than PMTs, and their compactness permits close packing of detector modules. Furthermore, they are insensitive to magnetic fields, making them suitable for combination with an MRI device [36]. However, their lower gain ( $10^2$ – $10^3$ ) compared to PMTs makes them more susceptible to electronic noise. The APD signals should therefore be amplified as closely as possible to the diode with low-noise charge sensitive preamplifiers (CSPs).

APDs consist of a *pn*-junction with several layers of differently doped material. The doping concentrations are such that when a reverse bias voltage is applied to the device, a region with a very high electric field strength is created. Many different types of APD structures have been developed, each with specific characteristics and applications. Fig. 2.3 shows a schematic of an APD of the reverse reach-through type, which is assumed to be similar to the structure of the Hamamatsu S8550 APDs used in this work [37]. The electric field strength as a function of the depth in the device is also shown.

A photon incident in the first layer, conventionally referred to as the conversion layer, can ionise the material and give rise to a primary electron-hole (e-h) pair. The applied electric field accelerates the electron towards the anode and the hole towards the cathode. In the structure depicted in Fig. 2.3, the electrons thus

cross the high-field region before reaching the anode. In this region, the kinetic energy they acquire between collisions is sufficient to allow impact ionisation of atoms in the material, giving rise to secondary e-h pairs. The avalanche multiplication created in this way results in an amplification of the measured signal.

The APD gain, commonly denoted by  $M$ , can be written as [38]:

$$M(x) = \frac{\exp\left[-\int_x^w (\alpha - \beta) dx'\right]}{1 - \int_0^w \alpha \exp\left[-\int_{x'}^w (\alpha - \beta) dx''\right] dx'} \quad (2.5)$$

where  $x$  is the position within the depletion layer where the multiplication process starts, and  $w$  is the width of the depletion layer. In this equation, the probabilities of generating new e-h pairs within a path length  $dx$  are represented by the ionisation coefficients for electrons and holes,  $\alpha$  and  $\beta$ , respectively [38]. These coefficients depend on the electric field strength, and therefore also on  $x$ . They are also material dependent. In Si, the material that constitutes the Hamamatsu S8550 APDs,  $\alpha \gg \beta$ , so that the holes only start contributing to the avalanche gain at much higher field strengths than the electrons. When both electrons and holes contribute to the avalanche, the response may become strongly non-linear, causing large signal variances, and currents of possibly destructive magnitude.

The variance associated with the stochastic multiplication process is usually expressed in terms of the excess noise factor  $J$ , defined as:

$$J = \frac{\text{var}\{M\}}{\overline{M}^2}, \quad (2.6)$$

where  $\overline{M}$  denotes the mean number of output e-h pairs per primary e-h pair. The excess noise factor depends on the ionisation coefficients for electrons and holes, and can thus be minimised by appropriate choice of the diode material. At lower field strengths, the excess noise factor is approximately linear with  $M$ , but if the electric field is increased enough to allow multiplication by electrons as well as holes, it increases rapidly [39, 40].

APD signals are affected by various types of electronic noise, the effect of which depends on the preamplifier and the way it is connected to the diode. In this work, each APD anode was DC-coupled to the gate of the FET at the input stage of a preamplifier, as shown schematically in Fig. 2.4.

Leakage currents through the APD and the input field effect transistor (FET) of the preamplifier give rise to shot noise. These currents may arise from thermally generated e-h pairs in the diode depletion layer, e-h pairs generated at the

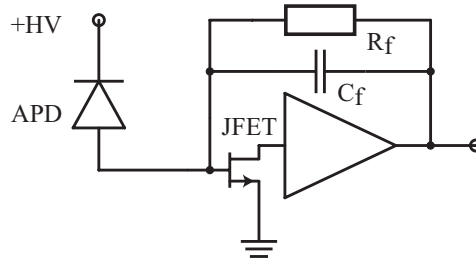


Figure 2.4: Schematic of the APD connection to the charge-sensitive preamplifier.

surface of the diode by the Shockley-Read mechanism [41] and diffusion currents between the different junctions in the diode [42]. Part of the leakage currents is amplified in the APD avalanche layer, and is consequently also affected by the excess noise factor.

Another important contribution to electronic noise is due to thermal noise of the input FET channel. The extent to which this noise affects the final signal increases with increasing input capacitance of the APD-preamplifier system; hence, APDs with a low capacitance are advantageous for low-noise applications. The way these noise sources affect the signals after further amplification and pulse shaping is discussed in more detail in Chapter 5.

## 2.4 Existing animal PET systems

The following section gives an overview of several existing animal PET systems based on scintillation detectors. Rather than a complete overview of past and current developments in small animal PET technology, a selection of designs is presented, meant to illustrate the strategies that have been followed in the design of scintillation detectors in order to improve various aspects of the scanner performance.

### 2.4.1 Early developments

The first animal PET scanners were designed for imaging non-human primates, and were based on the bismuth germanate (BGO) scintillator. An example of such a scanner is the ECAT-713 designed at CTI PET Systems Inc. (Knoxville, TN) [43]. It consisted of a single ring of detector modules with an inner diameter of 64 cm and an axial field of view (FOV) of 5.4 cm. It was equipped with

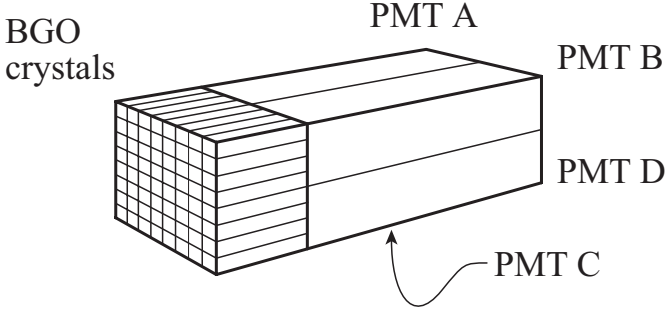


Figure 2.5: Schematic of the classic block detector design

60 mm deep by 0.5 mm thick tungsten septa and operated in 2D mode only. The detector modules consisted of  $6 \times 8$  matrices of  $3.5 \times 6.25 \times 30$  mm deep crystals, mounted on two dual-anode PMTs. This classic design is commonly referred to as the 'BGO block detector design', and is illustrated in Fig. 2.5. The position of each event was derived using Anger-type logic, i.e., using the ratio of the signals produced at each of the four PMT anodes with each interaction, according to:

$$X = \frac{(B + D) - (A + C)}{A + B + C + D} \quad Y = \frac{(A + B) - (C + D)}{A + B + C + D}, \quad (2.7)$$

where  $A$ ,  $B$ ,  $C$  and  $D$  respectively represent the top left, top right, bottom left and bottom right anodes.

The system resolution (i.e. the image resolution obtained using FBP reconstruction) at the centre of the field of view (CFOV) was  $3.8 \text{ mm} \times 3.8 \text{ mm} \times 4.2 \text{ mm}$  (radial  $\times$  tangential  $\times$  axial) [43]. At 12 cm radial distance from scanner central axis, this deteriorated to  $6.7 \text{ mm} \times 3.8 \text{ mm} \times 4.2 \text{ mm}$ . The maximum sensitivity reported was  $68.6 \text{ kcps}/\mu\text{Ci/cc}$  at a 250 keV lower energy threshold, measured with a  $\varnothing 20$  cm cylindrical phantom uniformly filled with a solution of  $^{68}\text{Ge}$ - $^{68}\text{Ga}$  at an activity concentration of  $0.084 \mu\text{Ci/cc}$ . The maximum NECR, measured using a  $\varnothing 10$  cm cylinder filled with a homogeneous solution of  $^{18}\text{F}$ , was reported to be approximately 70 kcps at an activity concentration of  $6 \mu\text{Ci/cc}$ .

## 2.4.2 MicroPET

More recent designs moved from the block-type detector design described above to matrices of scintillator crystals coupled to position-sensitive PMTs (PS-PMTs). An example of such a design is the MicroPET I system [44]. This system uses



the scintillation material LSO:Ce [29], which has a much higher light yield and a shorter scintillation decay time constant than BGO, and only a slightly longer attenuation length at 511 keV, see Table 2.2 [26].

The MicroPET I system consists of a single ring with an inner diameter of 17.2 cm containing 30 detector modules. It has a transaxial field of view of 11.2 cm, an axial field of view of 18.0 mm and operates in 3D mode only [44]. Each detector module consists of an  $8 \times 8$  matrix of  $2 \times 2 \times 10 \text{ mm}^3$  LSO:Ce crystals at a pitch of 2.25 mm, coupled to a 64-channel PS-PMT. The scintillation light is transmitted to the PMTs via 10 cm long optical fibres to allow closer packing of the modules.

The system resolution obtained with a  $\varnothing 0.5 \text{ mm}$  spherical  $^{22}\text{Na}$  point source at the CFOV is roughly 1.8 mm FWHM in all directions. At 50 mm radial distance from the CFOV, this degrades to  $3.8 \text{ mm} \times 2.5 \text{ mm} \times 2.3 \text{ mm}$  radial  $\times$  tangential  $\times$  axial. The point source sensitivity at the CFOV is 0.56% at an energy window setting of 250–650 keV. The maximum reported NECR obtained with a  $\varnothing 50.8 \times 108.5 \text{ mm}^3$  phantom representing a rat body filled with a solution of  $^{13}\text{N}$  at the same energy window setting is 4 kcps [45].

Several models improving upon the original MicroPET design have later been developed [46–49]. One of these, the MicroPET II, aims for an improved spatial resolution by using smaller crystal elements [48]. It consists of three rings of detector modules with an inner diameter of 16 cm and a total axial length of 4.9 cm. Each module consists of a  $14 \times 14$  array of LSO crystals measuring  $0.957 \times 0.975 \times 12.5 \text{ mm}^3$ , at a crystal pitch of 1.15 mm.

The system resolution reported for the MicroPET II, measured with a needle source with an outer diameter of 0.33 mm filled with  $^{18}\text{F}$ , is  $0.86 \text{ mm} \times 0.83 \text{ mm} \times 1.25 \text{ mm}$  radially  $\times$  tangentially  $\times$  axially at the CFOV [48]. At 20 mm radial distance from the CFOV, this degrades to  $1.97 \text{ mm} \times 1.22 \text{ mm} \times 1.50 \text{ mm}$ . The point source sensitivity at the CFOV is 2.29% at an energy window setting of 250–750 keV and a coincidence time window of 10 ns [17]. The maximum reported NECR obtained with a  $\varnothing 25 \times 70 \text{ mm}^3$  water phantom filled with a homogeneous solution of  $^{18}\text{F}$  is 235 kcps at an energy window of 150–750 keV and a coincidence time window of 10 ns.

The MicroPET II has a significantly improved system resolution compared to the original MicroPET system, due to the smaller lateral dimensions of its crystal elements. However, parallax effects cause a significant degradation of the radial system resolution at source positions away from the central scanner axis (see Chapter 1). A higher scanner sensitivity is achieved due to the improved geometrical efficiency and the thicker layer of scintillation material.

Another recent member of the MicroPET family, the MicroPET Focus, was designed to improve the scanner sensitivity while maintaining a very good spatial resolution [49]. This scanner has been made commercially available by Siemens in the Inveon series of preclinical imaging systems. The system consists of four rings with a diameter of 25.8 cm, each containing 42 detector modules. Each module consists of  $12 \times 12$   $1.51 \times 1.51 \times 10$  mm<sup>3</sup> LSO crystals at a pitch of 1.59 mm. The layer of optically reflective material used in the modules is thinner than in the MicroPET I, significantly reducing dead space.

The system resolution at the CFOV, measured with a  $\varnothing 0.5$  mm <sup>22</sup>Na-source, is 1.3 mm radially  $\times$  1.3 mm tangentially  $\times$  1.46 mm axially. At a radial distance of 60 mm from the scanner central axis, this degrades to 1.97 mm  $\times$  1.22 mm  $\times$  1.50 mm. The point source sensitivity at the CFOV, measured using an energy window of 250–750 keV and a coincidence time window of 10 ns, is 3.4%. The NECR of this scanner was evaluated using a  $\varnothing 30 \times 70$  mm<sup>3</sup> high-density polyethylene phantom simulating a mouse, containing a  $\varnothing 3$  mm glass capillary tube filled with <sup>11</sup>C at 7.5 mm radial offset from the centre. The maximum NECR reported is 650 kcps at an activity of  $\sim 150$  MBq.

The point source sensitivity of the MicroPET Focus is increased by almost 50% compared to the MicroPET II, in spite of its larger scanner diameter and reduced scintillator thickness. This is attributable both to the reduced dead space in its detectors and to its larger axial scanner length.

All spatial resolutions quoted above were obtained using analytical filtered backprojection algorithms in order to facilitate comparison between the different systems. Considerably better results have however been achieved using iterative algorithms that use models of statistics, blurring and attenuation effects in the image reconstruction. For instance, the image resolution of the MicroPET I system was improved from  $\sim 2$  mm FWHM at the CFOV to  $\sim 1.2$  mm FWHM using a 3D Bayesian maximum a-posteriori (MAP) algorithm, also achieving a much better resolution uniformity [50]. With the MicroPET II, an improvement of the image resolution was reported from  $1.1 \times 1.1 \times 1.4$  mm<sup>3</sup> FWHM at the CFOV with FBP to  $0.62 \times 0.62 \times 1.15$  mm<sup>3</sup> FWHM at the CFOV with a MAP algorithm [17].

### 2.4.3 ClearPET

A higher scanner sensitivity can be obtained with a thicker layer of scintillator material and a smaller ring diameter, at the expense of increased parallax error. To avoid these errors, several designs with different methods of depth of interaction (DOI) encoding have been proposed [51–53]. One of these is the ClearPET

system, of which several different versions have been made [54–56], including a commercial version built by Raytest [57] and a dedicated mammography system called ClearPEM [52]. In the ClearPET systems (except ClearPEM), DOI information is obtained by using a so-called phoswich configuration, in which two layers of different Ce-doped lutetium-based scintillators (LSO:Ce and LuYAP:Ce) are stacked on top of each other. Differentiation between the layers is achieved based on the different scintillation decay times of the two materials. Each detector consist of two layers of  $8 \times 8$  matrices of  $2 \times 2 \times 10 \text{ mm}^3$  crystals at a pitch of 2.3 mm, coupled to position-sensitive PMTs with an  $8 \times 8$  anode structure.

The commercially available Raytest ClearPET consists of four rings of 20 detector modules each. The modules can be moved radially to allow for scanner diameters between 135 mm and 250 mm [57].

The FWHM reconstructed spatial resolution of this system at its smallest diameter, measured with a  $\varnothing 1 \text{ mm}$  spherical  $^{22}\text{Na}$  point source, is approximately 1.25 mm radially at the CFOV using an iterative reconstruction algorithm (OS-MAPOSL [58]). This degrades to 3.0 mm radially  $\times$  2.3 mm tangentially at a radial distance of 40 mm from the CFOV [57], in spite of the DOI capability of this system. The point source sensitivity at the CFOV is 3.5% at an energy window setting of 250–750 keV and a coincidence time window of 20 ns. At the time of writing, no data on the axial spatial resolution or the counting rate performance of this system was available.

#### 2.4.4 APD-based systems

Before the development of detectors based on LSO and PS-PMTs, the development of APD-based PET systems was stimulated by the limited spatial resolution obtainable with BGO-block detectors. The low light yield of the BGO scintillator and the inability to decode inter-crystal scattered events in these detectors led to positioning errors that limited further improvement of the detector spatial resolution by reduction of the crystal dimensions. The compact size of APDs and their suitability to detect the scintillation light produced by BGO enabled the individual coupling of light sensors to small crystal elements, offering a solution to this issue.

The first successfully built scanner using APDs instead of PMTs is the Animal PET system developed at the Université de Sherbrooke [59]. This scanner consists of two rings with a diameter of 31 cm, each containing 256 detector elements. Each detector element consists of a  $3 \times 5 \times 20 \text{ mm}^3$  BGO-crystal coupled to a single-channel APD.

The compact size of APDs was exploited in different ways in later designs, as

exemplified by the RatCAP, developed at Brookhaven National Laboratories [60]. This very small scanner with a ring diameter of only 4 cm can be mounted directly onto the head of a rat, permitting neurophysiological studies to be carried out on awake animals. This avoids the need for anaesthetics which severely suppress the animal's brain functions and behaviour. The detector modules of the RatCAP consist of  $8 \times 4$  matrices of  $2 \times 2 \times 2 \text{ mm}^3$  LSO crystals, each coupled to one pixel of a Hamamatsu S8550 APD array, the same type of APD array used in this thesis.

A member of the ClearPET family designed for positron emission mammo-graphy (PEM), the ClearPEM, also uses this type of APD arrays [52]. This scanner consists of two parallel plates of detector modules. Each module consists of a  $8 \times 4$  matrix of  $2 \times 2 \times 20 \text{ mm}^3$  LYSO crystals coupled to two Hamamatsu S8550 APD arrays on opposite sides. Information on the depth of interaction in a crystal is extracted from the ratio of signal amplitudes measured by the two opposing APD pixels coupled to it. In this scanner, the annihilation photons have to pass through the APDs before reaching the scintillator. Because of the small size and low  $Z_{\text{eff}}$  of the APD material (Si), only a minimum of scattering and attenuation of the 511 keV photons occurs.

A recent APD-based small-animal scanner is the MadPET II, developed at the Technische Universität München [61]. It consists of a single ring with a diameter of 7.2 cm and an axial extent of 18.1 mm, containing 18 detector modules. Each module consists of two radially stacked detector layers, of which the inner layer consists of a  $8 \times 4$  matrix of  $2 \times 2 \times 6 \text{ mm}^3$  LSO crystals, and the outer layer consists of a  $8 \times 4$  matrix of  $2 \times 2 \times 8 \text{ mm}^3$  LSO crystals. Each crystal matrix is coupled to a Hamamatsu S8550 APD array, so that the two layers can be differentiated for DOI information. Integrated 16-channel low-noise preamplifiers specifically designed for this application are used to amplify the APD signals [62].

At the time of writing of this thesis, only preliminary results obtained with this scanner were available [63]. A spatial resolution of 1.25 mm FWHM is reported using an iterative reconstruction algorithm (3D MLEM), constant throughout the radial FOV, indicating good DOI correction. A system-wide energy resolution and time resolution of 22% and 9 ns, respectively, are achieved. Monte Carlo simulations predict a point source sensitivity of 2.8% [64]. These results indicate that PET scanners can be designed based on APD arrays and LSO crystals, that reach a performance similar to that of modern PMT-based high-resolution systems.

## 2.5 Monolithic Scintillator Detectors

Many high-resolution PET detector designs, including those discussed in the previous section, consist of individual crystal elements optically separated by reflective material. Although these designs aim to improve resolution by preventing light spreading, their performance is still limited by inter-crystal scattering. Designs which do not provide DOI correction always represent a tradeoff between system resolution (short crystals) and sensitivity (long crystals). In designs with DOI correction, the benefits of DOI are often gained at the expense of other performance parameters such as energy resolution and/or detection efficiency. Furthermore, the reflective material separating the crystals may take up a considerable fraction of the detector volume, reducing the detection efficiency. For example, the detectors of the MicroPET I system contain 19% of dead space due to reflective material; the detectors of the MicroPET Focus, which uses thinner reflectors, still have 9% of dead space.

Detectors with monolithic scintillators coupled to one or several position-sensitive light sensors can offer a solution to these issues [18, 19]. In this thesis, we consider detectors consisting of a few  $\text{cm}^3$  of LSO:Ce or LYSO:Ce, optically coupled to one or two Hamamatsu S8550 APD array(s), see Fig. 2.6. The distributions of scintillation light that arise due to the interactions of the annihilation photons within the crystal can be used to estimate the coordinates at which these photons crossed the front surface of the detector (the ‘entry point’). Together with the angle of incidence, which can be estimated from the positions of the two detectors triggering in coincidence in the PET ring, the entry point defines the path of the incident photon, and therefore the line of response.

An advantage of using unsegmented scintillators is the improved detection efficiency due to the absence of dead space in the detector modules. The compactness of the APD arrays additionally permits placing the modules closely together, further improving the scanner sensitivity. The implicit DOI correction provided by the proposed readout method may furthermore result in a reduction of parallax errors. This would lead to an improved image resolution at positions off the scanner central axis, and would allow the use of a thicker layer of scintillation material to further improve the scanner sensitivity. Finally, the detectors may be suitable for combination with an MRI device because of the insensitivity of the APDs to magnetic fields.

Implementation of these detectors requires overcoming a number of technical challenges. Because the scintillation light is spread over all APD pixels, the average number of photons detected per pixel is on the order of only a few hundred per event. In addition, the APDs have an internal gain of the order of only  $\sim 100$ .

The detected signals are therefore low, making amplification of each individual APD channel with a low-noise charge-sensitive preamplifier necessary. The sharing of scintillation light among the APD pixels furthermore results in a large signal dynamic range per channel, setting an additional requirement on the front-end electronics. Because the preamplifiers need to be placed as closely as possible to the APDs in order to minimise noise, limitations in space and power consumption point towards an application specific integrated circuit (ASIC) solution. The design of an ASIC that meets all the necessary requirements is a challenging task, but several integrated front-end solutions have already been successfully developed by other groups [65–67]. When using charge sensitive preamplifiers, the rise time of the measured signal is in general not determined by the scintillator rise time, but by its much slower decay time. The timing accuracy obtainable with APDs is therefore in general not as good as that obtainable with PMTs, but it has been shown that time resolutions adequate for PET can be obtained with LSO-APD detectors [61]. Finally, the positioning of the individual events on the detectors requires extra data processing steps, possibly leading to a very large data stream and increased processing time.

Achieving a significantly improved scanner sensitivity at image spatial resolutions comparable to current state-of-the-art systems would represent a major step forward in the development of dedicated high resolution PET technology. A detailed analysis of the performance characteristics of monolithic scintillator detectors is therefore presented in this thesis. This analysis is used to optimise the performance of the present detectors, and may aid the design of future PET systems based on detectors consisting of unsegmented scintillators with position-sensitive light sensor readout. Furthermore, the applicability of monolithic scintillator detectors in a high resolution PET system is investigated.

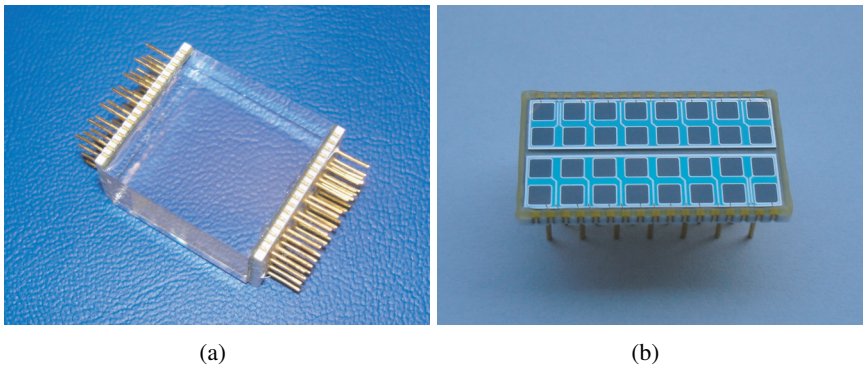


Figure 2.6: A monolithic scintillator detector (a) consisting of a  $20\times10\times20\text{ mm}^3$  LYSO:Ce crystal coupled to two Hamamatsu S8550 APD arrays (b).





# Chapter 3

## Materials and methods

### 3.1 Introduction

This chapter provides an overview of the experimental methodology used throughout this thesis. Section 3.2 describes the detector hardware and an experimental setup designed to characterise the detectors. In Section 3.3, the methods used for measuring the detector spatial, energy and timing resolutions are outlined. A characterisation of the key components of the experimental setup is presented in Appendix A.

### 3.2 Hardware description

The scintillator crystals investigated in this thesis consist of monolithic L(Y)SO:Ce blocks of several  $\text{cm}^3$ . The scintillation light created in the interactions with 511 keV photons is detected by one or two Hamamatsu S8550-SPL APD arrays (Hamamatsu Photonics, Japan), coupled to the crystals using the optical coupling fluid Meltmount (Cargille Laboratories, Cedar Grove, NJ, USA), see Fig. 2.6a. The APD arrays consist of a  $4 \times 8$  matrix of  $1.6 \times 1.6 \text{ mm}^2$  APD pixels at a pitch of 2.3 mm (see Fig. 2.6b). Depending on the crystal thickness, the scintillation light is collected either with a single APD array coupled to the front or the back surface of the crystal, or with two APD arrays coupled to opposite sides, see Fig. 3.1. The sides of the crystals not coupled to an APD array are wrapped in several layers of Teflon to maximise light collection.

Each bank of an APD array has a specific bias voltage  $V_{50}$  at which the gain  $M = 50$  according to the manufacturer specifications. Differences in  $V_{50}$  of 10–20 V are common between banks in the same array and between different arrays.

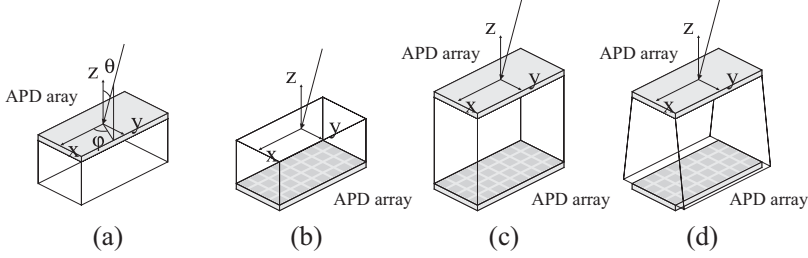


Figure 3.1: Schematic representation of rectangular 10 mm thick detectors, a rectangular 20 mm thick detector and a trapezoidal 20 mm thick detector. The APD array of the 10 mm detector is placed either on the back side of the crystal (a) or on the side facing the beam (b); the 20 mm detector have APD arrays on opposing sides (c and d). The coordinate system defining oblique angles of incidence is indicated in (a).

Throughout this work, the APD bias voltage therefore is expressed in terms of  $\Delta V \equiv V - V_{50}$ , where  $V$  is the applied bias voltage. It is shown in Appendix A that although  $V_{50}$  varies significantly between the different banks of the APD arrays used, the average gains per bank are equal within 4% when measured as a function of  $\Delta V$ .

The APD arrays are mounted onto custom made printed circuit boards (PCBs), each containing 32 Cremat CR-110 (Cremat Inc., Watertown, MA, USA) low-noise charge sensitive preamplifiers (CSPs) which individually preamplify the signal from each APD channel, see Fig. 3.2a. The input of each preamplifier is fitted with a test capacitance of  $\sim 1.8$  pF; the test capacitances are connected to a common test input on the PCB.

The detectors and PCBs are contained in a light-tight Al box, see Fig. 3.2b. The box has outer dimensions of  $160 \times 160 \times 160$  mm<sup>3</sup>. Two perpendicular sides of the box are fitted with 0.5 mm Al windows. The temperature of the box is regulated with Peltier coolers on two opposite sides, controlled by a PID controller connected to a temperature sensor placed fitted to the outside of the box with thermal paste. The temperature on the inside of the box is homogenised using a small, low-noise fan. Four LM35D temperature sensors inside the box monitor the temperature close to the APDs, between the preamplifiers, and in the air surrounding the PCBs. The lid of the box is fitted with two micro-switches that ensure that no bias voltage can be applied to the APD arrays when the box is open.

All signals going in and out of the detector box pass through a signal feed-through box, fixed to the lid of the detector box. The APD bias voltage supplies, the power supplies for the preamplifiers and the fan, the temperature sensor leads

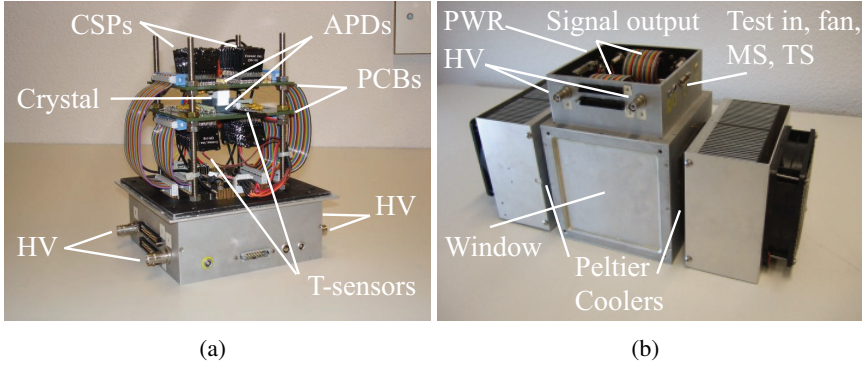


Figure 3.2: (a): Monolithic scintillator detector mounted on two PCBs. (b): Detector box and signal feed-through box. CSP: charge-sensitive preamplifier; HV: high voltage input; MS: micro switch; PWR: preamplifier power supply; TS: temperature sensor.

and the lead for the micro-switches are filtered in the feed-through box in order to minimise interference on the APD signals. The test input signals and the output preamplifiers signals pass through the feed-through box unfiltered.

An illustration of the setup is presented in Fig. 3.3. A  $^{22}\text{Na}$ -source (MMS06, Isotope Products, Valencia, CA, USA), consisting of a  $\varnothing 0.5 \times 1 \text{ mm}^3$  ion exchange bead containing  $^{22}\text{Na}$  embedded in a  $\varnothing 2.54 \times 5 \text{ mm}^3$  PMMA cylinder, is used as a source of 511 keV photons. A narrow photon beam is created by electronic collimation, using a second detector in coincidence with the APD detector. This second detector consists of a  $\varnothing 19 \times 35 \text{ mm}^3$  BGO crystal coupled to a PMT (XP2020) fitted with a 60 mm thick Pb collimator with a  $\varnothing 5 \text{ mm}$  aperture. The detector box is placed on an  $\text{XY}\Omega$ -stage controlled by stepper motors, with either of its thin Al windows facing the source. This permits scanning of the detector through the photon beam at many different orientations and incidence angles.

The diameter of the test beam can be controlled by varying the distances between source, PMT, and APD detector. The photon fluence profile is assumed to be circularly symmetric about the beam axis. The diameter  $d_b$  of the (slightly divergent) beam is defined as the full width at half maximum (FWHM) of the fluence profile at the front surface of the crystal. Values of  $d_b$  are determined by Monte Carlo simulation of the experimental setup (see Chapter 6).

The output tail pulses from the preamplifiers are fed through twisted-pair flat-cables to four CAEN N568BB 16-channel spectroscopy amplifiers for further amplification and shaping (CAEN S.p.A., Viareggio, Italy). These amplifiers have a fast and a slow output branch for each channel. The fast output branch is a fixed-

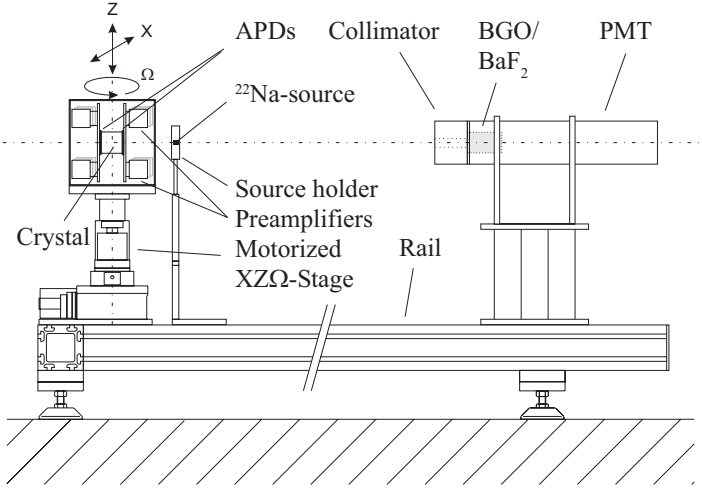


Figure 3.3: Schematic representation of the experimental setup.

gain single differentiation stage with a time constant of 100 ns. The slow branch contains a shaping network with a response resembling that of a  $\text{CR}-(\text{RC})^2$  shaper, with an adjustable gain and nominal shaping times of 0.1, 0.2, 1 and 3  $\mu\text{s}$ . More details concerning the response of these amplifiers are presented in Appendix A.

A schematic representation of the front-end electronics is shown in Fig. 3.4. The signals from the fast amplifier outputs are fed into a summing amplifier built in-house for time pickoff. Depending on the type of measurement to be performed, the shaped output pulses from the slow branch of the spectroscopy amplifiers can either be fed into a summing amplifier, or into two CAEN V785 multi-channel analogue-to-digital converter (MC-ADC) modules, see Section 3.3. Each MC-ADC module has 32 input channels with individual peak sensing circuits, of which the outputs are multiplexed and converted by two fast 12-bit ADCs. The input voltage range of the MC-ADCs is 0–4 V.

Control of the setup (stepper motors, shaping amplifiers and MC-ADCs) and data acquisition is performed by a LabVIEW (National Instruments, Austin, TX, USA) program running on a PC. Communication with the stepper motors and the amplifiers is established using interfaces provided by the manufacturers, the output signals from the MC-ADCs are read out via a VME interface (Wiener GmbH, Burscheid, Germany).

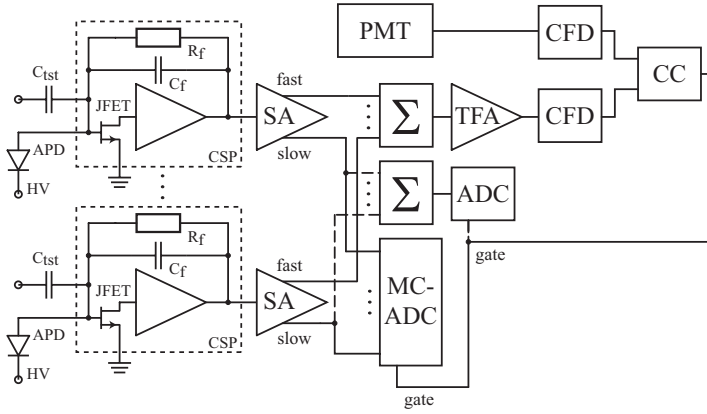


Figure 3.4: Schematic representation of the front-end electronics. CSP: charge-sensitive preamplifier; SA: shaping amplifier; TFA: timing filter amplifier; MC-ADC: multichannel ADC; CC: coincidence circuit;  $\Sigma$ : summing amplifier.

### 3.3 Detector performance measurements

#### 3.3.1 Spatial resolution

##### Event positioning

The entry point of an unknown event is estimated by comparing its measured light distribution, consisting of the 32 or 64 output values of the MC-ADCs, to a set of reference data. These reference data are collected by irradiating the detector with 511 keV photons at a series of known positions  $\mathbf{x}_i = (x_i, y_i)$ , see Fig. 3.1, and recording the light distributions of  $n_{ref}$  events at each position. The light distribution of each event in the reference set is then normalised such that the sum of all detector signals equals unity.

The entry point of an unknown annihilation photon can then be estimated by calculating the sum-of-squares difference of its (also normalised) light distribution with the light distributions of all events in the reference set. A subset of the reference data consisting of the  $L$  closest matches (‘nearest neighbours’) is selected, and the most frequently occurring entry point within this subset is assigned to the unknown event.

This method is known as the  $L$ -nearest neighbour method. It has the advantage that the probability of misclassification approaches the theoretical minimum, the Bayes error probability, for sufficiently large reference sets [68]. The algorithm is

therefore expected to yield results close to the best achievable with the available reference data, provided that a suitable value of  $L$  be used.

### Detector point spread function

After estimating the entry points of a series of test events, a normalised, two-dimensional (2D) histogram of the errors  $\Delta \mathbf{x}_j = (\hat{\mathbf{x}}_j - \mathbf{x}_t)$  can be created, where  $\hat{\mathbf{x}}_j$  is the estimated entry point of the  $j$ -th test event recorded at  $\mathbf{x}_t = (x_t, y_t)$ . This histogram approaches the detector point-spread function  $PSF(x, y)$  at  $\mathbf{x}_t$  if the number of test events is sufficiently large. The FWHM and FWTM of the point spread function, found by linear interpolation of the histogram, are used as measures for the detector spatial resolution.

The width of the PSF depends on the number of reference events recorded per position, decreasing asymptotically to a minimum with increasing  $n_{\text{ref}}$ , and on  $L$ . The optimum value of  $L$  is usually on the order of  $0.5n_{\text{ref}}$ , but can fluctuate strongly between measurements. Optimisation of the PSF was performed in each experiment by finding the value of  $L$  minimising the width of the histogram, expressed as  $\langle \sigma_{\text{PSF}}^* \rangle \equiv 1/2 (\sigma_{\text{PSF},x}^* + \sigma_{\text{PSF},y}^*)$ , the average of its sample standard deviations in the  $x$ - and  $y$ - directions. The asterisk is used to indicate that PSF values below 1% of the peak amplitude are disregarded in order to reduce the effect of outliers. An example of such an optimisation is presented in Appendix A; an estimation of the uncertainty of the PSF FWHM and FWTM obtained with this algorithm is presented there as well.

### Parameter studies

Throughout this thesis, the influence of various parameters (such as the crystal type, the angle of incidence, etc.) on the spatial resolution is investigated by varying the parameter of interest in a series of measurements. For efficiency, this was done in a one-dimensional (1D) form of the above experiment, in which reference data were collected along one of the crystal axes, and only the coordinate corresponding to that axis was taken into consideration. For example, reference data were collected at a set of coordinates  $\{\mathbf{x}_i\} = (\{x_i\}, y = 0)$ , the  $x$ -coordinates of a set of events recorded at test position  $\mathbf{x}_t = (x_t, y = 0)$  were estimated, and a normalised 1D histogram of errors  $\Delta x_j = (\hat{x}_j - x_t)$  was derived. This histogram is referred to as the one-dimensional point spread function 1D-PSF( $x$ ).

### Leave-one-out method

In experiments with equal parameters for the reference and the test data, the same data set was used for both in order to reduce measurement times. This was done by estimating the entry point of each test event  $j$  recorded at  $\mathbf{x}_t$  using the remaining  $n_{\text{ref}} - 1$  events recorded at  $\mathbf{x}_i = \mathbf{x}_t$ , as well as all events collected at all other positions  $\{\mathbf{x}_i\}$ , as reference data. This approach is referred to as the leave-one-out method.

#### 3.3.2 Energy resolution

Energy resolution measurements were performed by feeding the slow output signals of the amplifiers through a summing amplifier built in-house. Pulse height spectra were measured on the resulting analogue sum signal with an ADC (Ortec AD413A). The spectra were then fitted with a Gaussian function, and the FWHM of the fit divided by the peak position was used as a measure of the energy resolution.

#### 3.3.3 Timing resolution

Timing resolution measurements were performed by replacing the BGO-PMT detector with a  $\varnothing 25.4 \times 25.4 \text{ mm}^3$  BaF<sub>2</sub> crystal coupled to an XP2020Q PMT (see Fig. 3.3). The PMT signal was fed directly into a constant fraction discriminator (CFD, Ortec 934) for time pickoff. For the APD detectors, the analogue sum signal of the fast outputs was fed through a timing filter amplifier (TFA, Ortec 454) with variable differentiation and integration time constants. The filtered signal was fed into a CFD (Ortec 934) for time pickoff. Time spectra were measured using a time-to-amplitude converter (TAC, Ortec 476) and an Ortec AD413A ADC. A calibration of the time axis was made with an Ortec 462 time calibrator. The time spectra were fitted with a Gaussian function, and the FWHM of the fit was used as a measure of the detector timing resolution.





# Chapter 4

## Detector performance<sup>1</sup>

### Abstract

This chapter presents an overview of the performance of monolithic scintillator detectors. A method is introduced to correct the PSF for the finite test beam diameter in order to obtain the intrinsic detector spatial resolution. A comparison is made between detectors with various crystal surface finishes and readout geometries, including detectors with a trapezoidal shape. These detectors can be placed in a PET ring with a minimum of dead space, maximising the scanner sensitivity. The correction for depth-of-interaction (DOI) of the annihilation photons is tested by measuring the spatial resolution as a function of the angle of incidence. Energy and timing resolutions of the detectors are also reported.

An intrinsic detector spatial resolution of 1.05 mm FWHM is shown to be feasible, after correction for the influence of the  $\sim 0.9$  mm FWHM measurement beam. This is comparable to the spatial resolution of detectors in modern high-resolution systems. The spatial resolution measured with trapezoidal detectors is almost the same as with rectangular detectors. The spatial resolution is found to be essentially independent of the angle of incidence, for angles up to  $30^\circ$ . For a scanner, this means that the usual tradeoff between detector thickness and spatial resolution is removed. The scanner sensitivity can thus be maximised without degrading the image resolution towards the edges of the field of view (FOV). Energy resolutions of around 11% FWHM are measured, with  $\sim 75\%$  of the events falling in the full-energy peak. The estimated coincidence timing resolution of

---

<sup>1</sup>Parts of the results presented in this chapter are to be published as M. C. Maas, D. R. Schaart, D. J. van der Laan *et al.*, “Monolithic Scintillator PET Detectors with Intrinsic Depth-of-Interaction Correction”

2.8 ns is sufficient for adequate rejection of random coincidences.

## 4.1 Introduction

This chapter presents an overview of the performance of monolithic scintillator detectors based on L(Y)SO:Ce crystals and Hamamatsu S8550 APD arrays. The energy resolution, timing resolution and spatial resolution of the detectors are investigated. Detector designs with different geometries and crystal surface treatments are compared, including detectors with a trapezoidal shape, which allow the construction of a detector ring with almost no dead space. A method is introduced to obtain the intrinsic detector spatial resolution by correcting for the finite test beam diameter. Correction for the depth-of-interaction (DOI) is tested by measuring the detector spatial resolution as a function of the angle of incidence.

## 4.2 Materials and Methods

### 4.2.1 Crystals

A list of the crystals investigated is presented in Table 4.1. The sample names are comprised of the material name, the crystal thickness in mm, a code representing the surface finish, an optional code for the crystal shape, and a sample number. The surface finish is coded as follows: crystals marked 'P' are mechanically polished, crystals marked 'E' are treated with a chemical etching procedure described in [69], while crystals marked 'A' received no special surface treatment after cutting. Most crystals have a rectangular shape, but crystals marked 'T' are trapezoidal, and are read out with the small surface facing the beam (see Fig. 4.1). Their dimensions are chosen in such a way that they can form a closed ring of 32 detectors with a distance of 123.8 mm between the inner surfaces of two directly opposing detectors. Fig. 4.1 shows a schematic representation of the detector geometries investigated.

The absolute light yield of the crystals was measured on a calibrated PMT setup, using an Ortec 627 shaping amplifier set to a shaping time of  $1\ \mu\text{s}$  and an Ortec AD114 ADC. The crystals, wrapped in Teflon tape, were irradiated with 662 keV photons from a  $^{137}\text{Cs}$  source, and the photoelectron yield was obtained by comparison of the position of the full-energy peak of the pulse-height spectrum with that of the single-electron spectrum. Absolute light yields were calculated by correcting for the effective PMT reflectivity and quantum efficiency [35].

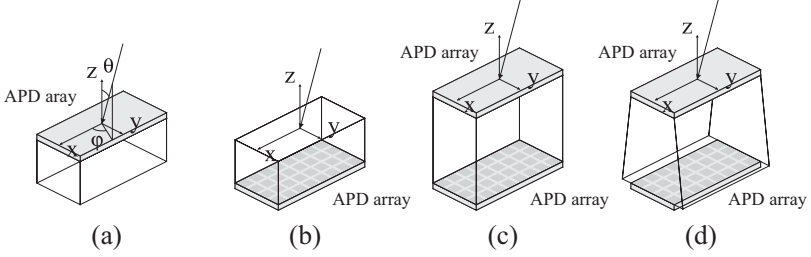


Figure 4.1: Schematic representation of the detector geometries investigated: (a) front-side readout, (b) back-side readout, (c) double-sided rectangular, (d) double-sided trapezoid. In (a), the coordinate system used to specify the scan directions and angles of incidence is also indicated.

Table 4.1: Properties of the scintillation crystals investigated.

Sample	Material	Surface treatment	Dimensions ( $x \times y \times z$ mm <sup>3</sup> )	Vendor
LYSO10-P1	LYSO:Ce	polished	$20 \times 10 \times 10$	Photonic Materials
LYSO10-P2	LYSO:Ce	polished	$20 \times 10 \times 10$	Crystal Photonics
LSO10-A	LSO:Ce	as-cut	$20 \times 10 \times 10$	Hilger Crystals <sup>1</sup>
LSO10-E	LSO:Ce	etched	$20 \times 10 \times 10$	Hilger Crystals <sup>1</sup>
LYSO20-P1	LYSO:Ce	polished	$20 \times 10 \times 20$	Photonic Materials
LYSO20-P2	LYSO:Ce	polished	$20 \times 10 \times 20$	Crystal Photonics
LSO20-A	LSO:Ce	as-cut	$20 \times 10 \times 20$	Hilger Crystals <sup>1</sup>
LSO20-E	LSO:Ce	etched	$20 \times 10 \times 20$	Hilger Crystals <sup>1</sup>
LYSO20T-P	LYSO:Ce	polished	$19.5 \times 11.2(15.4) \times 20$	Crystal Photonics
LYSO20T-A	LYSO:Ce	as-cut	$19.5 \times 11.2(15.4) \times 20$	Crystal Photonics

<sup>1</sup> Base material provided by CTI.

### 4.2.2 Energy resolution

Pulse height spectra of the assembled detectors were measured using a  $\varnothing 5$  mm FWHM beam of 511 keV photons aimed at the detector centre. The measurements were performed at  $T = 23.3 \pm 3.6$  °C, where  $T$  refers to the temperature close to the APD array(s). For detectors with 2 APD arrays,  $T$  was measured near the array on the back surface of the crystal. All measurements were carried out using a shaping time of  $\tau = 0.2$   $\mu$ s. FWHM energy resolutions were obtained by fitting the full-energy peaks with Gaussian fundtions.

### 4.2.3 Timing resolution

Time spectra were recorded using the procedure outlined in Section 3.3.3. The timing filter amplifier was set to an integration time constant of 2 ns, while the differentiation time constant was set to ‘out’. An energy threshold  $E_{\text{th}} \sim 250$  keV was applied in all experiments. FWHM timing resolutions were obtained by fitting the spectra with Gaussian functions.

### 4.2.4 Spatial resolution

Spatial resolution measurements were performed according to the procedure outlined in Section 3.3.1. In each measurement, all events above an energy threshold  $E_{\text{th}} = 100$  keV were accepted. The beam diameter  $d_b$  was determined for each measurement using Monte Carlo simulations of a detailed model of the experimental setup. These simulations are described in detail in Chapter 6. All spatial resolution measurements were performed at  $\Delta V = 0$  V,  $\tau = 0.2$   $\mu$ s and  $T = 23.2 \pm 3.6$  °C.

### Point spread function

The PSF of crystal LYSO20-P2 was measured by collecting  $n_{\text{ref}} = 500$  reference events on a regular, rectangular grid covering slightly more than half of the crystal: between  $-10 \leq x \leq 10$  mm and  $-2 \leq y \leq 5$  mm (see Fig. 4.1 for the definition of the coordinates). The grid spacing was 0.25 mm in both the  $x$ - and the  $y$ - direction. The test data were drawn from the same data set (leave-one-out approach), covering all  $x$ -coordinates and  $0 \leq y \leq 5$  mm. The reference data between  $-2 \leq y \leq 0$  mm were collected to avoid truncating the error histogram at  $y = 0$ . These data were collected using a beam diameter  $d_b = 0.96$  mm.

### Correction for test beam diameter

The measured PSF includes the influence of the test beam diameter  $d_b$ . In this chapter, the measured result is therefore denoted as the uncorrected point spread function  $PSF_b(x,y)$  to distinguish it from the corrected result that will be written without the subscript ‘b’. Correcting  $PSF_b$  for the test beam diameter by straightforward deconvolution has appeared to be difficult because of the divergence of the beam. Instead, a correction was made using a simple model of the PSF, which is presented in detail in Chapter 6, and summarised briefly here.

The model applies to in the central part of the detector and describes the PSF as a convolution of two 2D distributions plus a small background:

$$PSF_b(x,y) = \{\gamma_b * N_\Sigma\} + B \quad (4.1)$$

The first distribution in this equation,  $\gamma_b$ , describes the spatial distribution of the energy deposited within the crystal due to interaction processes following the absorption of a 511 keV photon, such as Compton scattering and X-ray fluorescence. The second distribution,  $N_\Sigma$ , accounts for the positioning error resulting from the finite signal-to-noise ratio of the detector signals (as determined by photon statistics, APD dark current, excess noise factor, electronic noise, etc.). The third distribution,  $B$ , models a small background contribution which accounts for events that scatter on materials present between the  $^{22}\text{Na}$  source and the crystal, such as an APD array on the front surface of the crystal.

The 2D distribution  $\gamma_b$  is estimated by means of a Monte Carlo simulation. This has been done both for a detailed model of the test beam used in our experiments (Chapter 6), and for the case of a ‘pencil’ beam having zero diameter, the result of which is denoted by  $\gamma_0$ . The distribution  $N_\Sigma$  is modelled by a 2D Gaussian function with covariance matrix  $\Sigma$ , of which the off-diagonal elements are assumed to be equal to zero. It is shown in Chapter 6 that this is a valid approximation at the low noise levels at which these experiments are carried out. Using these distributions, the measured  $PSF_b(x,y)$  is least-squares fitted to the model (4.1), using the diagonal elements of  $\Sigma$  and the amplitude of  $B$  as fit parameters. The corrected  $PSF(x,y)$  is subsequently estimated by convolving  $\gamma_0$  and  $N_\Sigma$ , and adding  $B$ .

### Geometry and surface finish comparison

The point spread functions of the crystals listed in Table 4.1 were compared in a series of measurements in which the APD arrays and other parameters were kept the same. The PSFs of crystals with different surface finishes were compared,

and the effect of the detector geometry (see Fig. 4.1) on the PSF was investigated. These studies were performed in 1D for efficiency, see Chapter 3. It is noted that the resulting 1D resolutions cannot be compared directly to the 2D results given in the above sections; the 1D results tend to be a few tenths of a mm FWHM larger than the 2D results in otherwise equal measurements. Nevertheless, the 1D-PSFs are useful to study the variation of the spatial resolution with the parameter of interest.

In this study, reference data were collected on a grid between  $-10 \leq x \leq 10$  mm at  $y = 0$  with a grid spacing of 0.25 mm, using  $d_b = 0.84$  mm FWHM. At each beam coordinate,  $n_{\text{ref}} = 1500$  events were collected. The  $x$ -coordinate of each event in the reference set was estimated using the leave-one-out method, so that the resulting 1D-PSF contained data from all coordinates. Each PSF was calculated using the value of  $L$  that minimised  $\sigma_{\text{PSF}}^*$ . These measurements were performed at  $\Delta V = 0$  V,  $T = 23.2 \pm 2.1$  °C and  $E_{\text{th}} \approx 100$  keV

### Depth of interaction correction

The depth of interaction (DOI) correction of the detectors was tested by measuring PSFs as a function of the angle of incidence  $\theta$ , at  $\phi = 0^\circ$  and  $\phi = 90^\circ$ . At each incidence angle,  $n_{\text{ref}} = 1500$  events per position were collected over a 1D grid covering the detector  $x$ - or  $y$ -axis, with a grid spacing of 0.25 mm. At  $\theta \neq 0^\circ$ , the crystal side facing the beam was included in the scans. The 1D-PSFs were again made using the leave-one-out method, so that the coordinate of each test event was estimated using reference data collected at the same incidence angle.

At normal incidence, the positioning errors expressed in terms of the coordinates  $x$  and  $y$  defined within the plane of the crystal front surface (see Fig. 4.1) coincide with the errors in the position of the line of response (LOR) in a PET system. To study the PSF as a function of the angle of incidence  $\theta$ , however, the errors must be projected onto a plane perpendicular to the LOR (or the beam axis in our test setup). We therefore define coordinates  $x'$  and  $y'$  within this plane such that  $x' = x \cos(\theta)$  and  $y' = y$  at  $\phi = 0^\circ$ , while  $x = x$  and  $y = y \cos(\theta)$  at  $\phi = 90^\circ$ .

## 4.3 Results & Discussion

### 4.3.1 Energy resolution

Table 4.2 shows the energy resolution of the detectors investigated, measured at 511 keV. The absolute light yields of the crystals are also listed. Fig. 4.2 shows an

Table 4.2: Light yield per MeV and energy resolution at 511 keV of the crystals studied. The light yields were measured with a calibrated PMT setup, the energy resolutions with the APD arrays. The absolute light yields have an uncertainty of approximately 10%, the energy resolutions have an uncertainty of approximately 0.2 % FWHM.

Sample	Abs. LY ( $10^3$ ph/MeV)	APD arrays	$\Delta E/E$ (%)
LYSO10-P1	15.2	1	11.0
LYSO10-P2	21.2	1	10.4
LSO10-A	13.4	1	12.6
LSO10-E <sup>1</sup>	–	1	–
LYSO20-P1	14.2	2	12.0
LYSO20-P2	20.2	2	10.5
LSO20-A	13.6	2	16.5
LSO20-E	17.1	2	13.3
LYSO20T-P	22.8	2	11.0
LYSO20T-A	21.5	2	10.5

<sup>1</sup> Measured spectra had strongly non-Gaussian photo peaks, precluding determination of light yield and energy resolution.

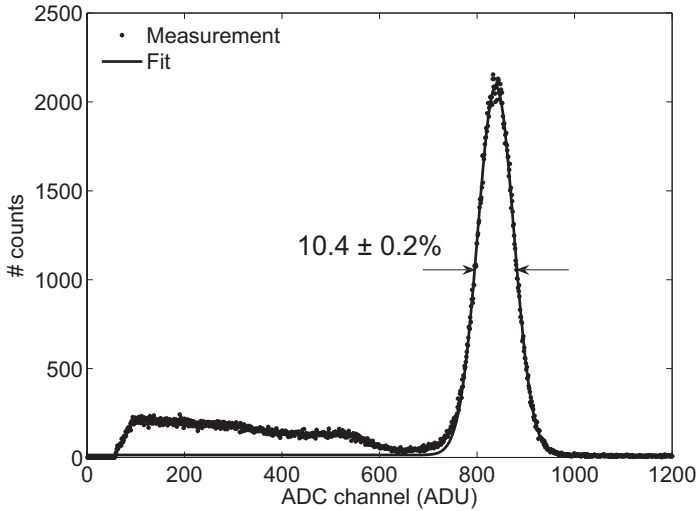


Figure 4.2: Measured pulse height spectrum (circles) with Gaussian fit (solid curve) of sample LYSO10-P2 at 511 keV, recorded at  $\Delta V = 0$  V and  $T = 22.2 \pm 0.2$  °C.

example of a pulse height spectrum, measured at 511 keV with detector LYSO10-P2, a  $20 \times 10 \times 10 \text{ mm}^3$  polished LYSO crystal coupled to one APD array. The corresponding energy resolution is  $10.4 \pm 0.2\%$  FWHM.

In Fig. 4.2, the full-energy peak contains  $\sim 70\%$  of the events, although the probability of photoelectric interaction of 511 keV photons in LYSO is only  $\sim 30\%$  of the total probability of interaction. With 20 mm thick detectors, the fraction of full-energy events is  $\sim 75\%$ . This is due to the large fraction of Compton-scattered photons that are re-absorbed within the relatively large crystal. In a PET system, this has the advantage that the application of an energy threshold to reduce the influence of intra-subject scattering has a relatively small effect on the sensitivity to true events.

A detailed analysis of how different factors such as the scintillation photon statistics, APD dark current, APD excess noise factor, electronic noise, etc., influence the energy resolution of the detectors is presented in Chapter 5.

### 4.3.2 Timing resolution

Fig. 4.3 shows a coincidence timing spectrum measured with detector LYSO20-P2 ( $20 \times 10 \times 20 \text{ mm}^3$  polished LYSO coupled to two APD arrays) against a  $\text{BaF}_2$ -PMT detector. A timing resolution of  $2.0 \pm 0.1 \text{ ns}$  FWHM is obtained with this detector. Assuming that the contribution of the  $\text{BaF}_2$ -PMT detector is negligible, the coincidence timing resolution of two of these detectors equals  $\Delta t = 2.8 \text{ ns}$  FWHM. A detailed analysis of how the timing resolution depends on the various factors determining the signal-to-noise ratio of the detector signals is presented in Chapter 5.

### 4.3.3 Spatial resolution

#### Point spread function

Fig. 4.4 shows the uncorrected point spread function  $PSF_b(x, y)$  of crystal LYSO20-P2 measured at normal incidence. This 2D error histogram is averaged over the central region of the detector ( $-3 \leq x \leq 3, 0 \leq y \leq 1.5$ ) mm, in order to minimise the statistical fluctuations in the histogram.

Fig. 4.5 shows the FWHM of  $PSF_b(x)$ , the cross-section of  $PSF_b(x, y)$  in the  $x$ -direction at zero  $y$ -error (a), and  $PSF_b(y)$ , the cross-section of  $PSF_b(x, y)$  in the  $y$ -direction at zero  $x$ -error (b), as a function of the beam position for  $y \geq 0$ .  $PSF_b(x)$  and  $PSF_b(y)$  appear to be roughly constant in the central part of the detector, except for statistical fluctuations arising from the limited number of data points per histogram.



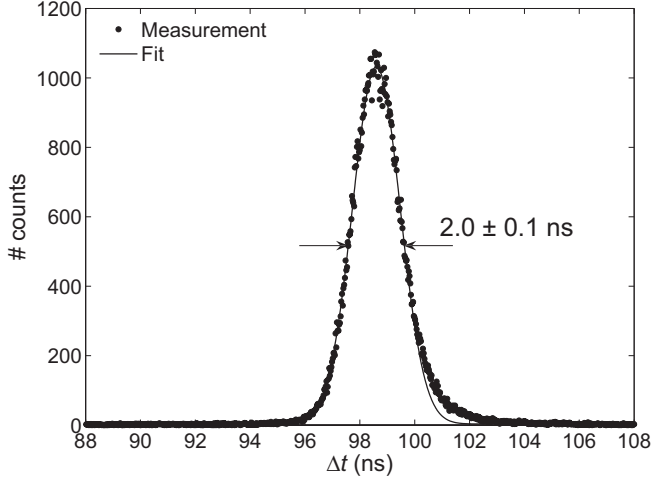


Figure 4.3: Measured timing spectrum (circles) and Gaussian fit (solid curve) of LYSO20-P2, recorded at  $\Delta V = 19$  V,  $E_{\text{th}} = 250$  keV and  $T = 24.3 \pm 0.2$  °C.

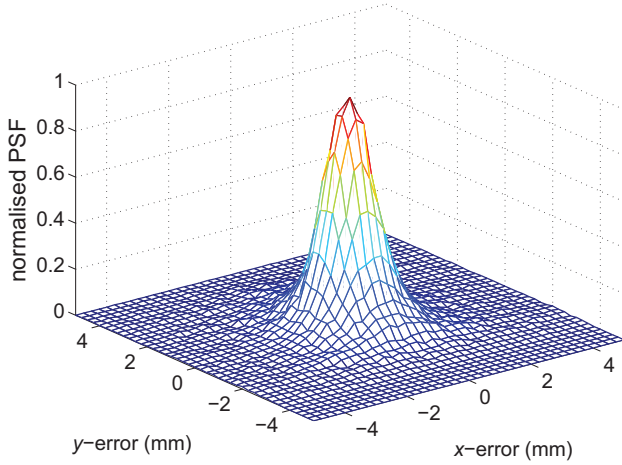


Figure 4.4: Measured point spread function  $PSF_b(x, y)$  of crystal LYSO20-P2 at the detector centre, obtained at normal incidence using  $L = 500$ . This PSF is not corrected for the beam diameter  $d_b = 0.96$  mm FWHM.

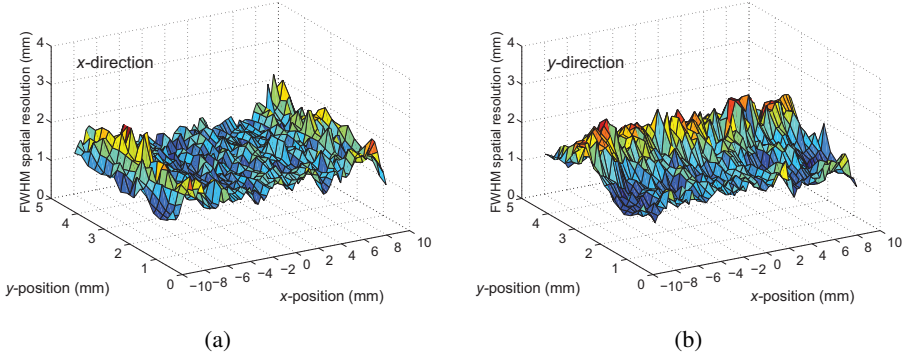


Figure 4.5: FWHM of  $PSF_b(x)$  (a) and  $PSF_b(y)$  (b) of LYSO20-P2 measured at normal incidence as a function of the test beam position. Values are derived from PSFs averaged over  $1 \times 1 \text{ mm}^2$  segments and are not corrected for  $d_b = 0.96 \text{ mm}$  FWHM.

The spatial resolution in the  $x$ -direction deteriorates near the two crystal surfaces perpendicular to the  $x$ -axis. At a distance of about 3–4 mm from these crystal edges, the FWHM starts to increase, up to an average value of 1.9 mm at  $\sim 2 \text{ mm}$  from the crystal edges. At still smaller distances the FWHM decreases again, as the PSF becomes truncated on one side due to the absence of reference data beyond the crystal edges. Similar results are observed in the  $y$ -direction: the FWHM of  $PSF_b(y)$  is best in the central part of the detector, while some deterioration of the spatial resolution in the  $y$ -direction is found near the crystal edges perpendicular to the  $y$ -axis only. These effects have been predicted by optical simulations [70] and have also been reported for 1-D PSFs elsewhere [71].

### Intrinsic detector spatial resolution

The results presented in the previous section include the influence of the finite test beam diameter. This influence can be corrected for using the PSF model described in Section 4.2.4. Here we illustrate the correction procedure with the PSF shown in Fig. 4.4; a validation of the model is presented in Chapter 6.

Fig. 4.6 shows the cross-sections  $PSF_b(x)$  of both the measured (closed circles) and the model (dotted curve) PSF. Excellent agreement is observed between the model and the measurements. The cross-section  $PSF(x)$  of the corrected detector PSF is indicated by the solid curve in the same figure.

Table 4.3 shows the FWHM and FWTM in the  $x$ - and  $y$ -directions of cross-sections through the measured and the corrected PSF at  $y = 0$  and  $x = 0$ , respec-

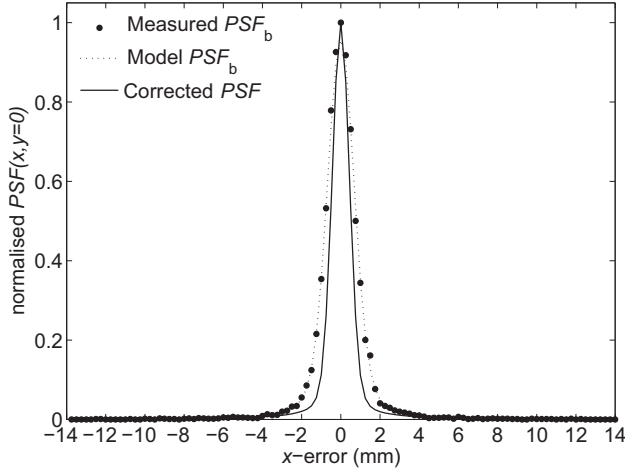


Figure 4.6: Cross-sections of the measured (closed circles) and modelled (dotted curve)  $PSF_b(x,y)$  at  $y=0$ , and cross-section through the corrected  $PSF(x,y)$  (solid curve). These results are derived from the PSF measured at the centre of crystal LYSO20-P2 which is shown in Fig. 4.4.

tively. In the  $x$ -direction, a very good spatial resolution of 1.05 mm FWHM is found. In the  $y$ -direction, the PSF is slightly wider. This is probably due to the reduced number of APD pixels and the smaller dimensions of the crystal in this direction compared to the  $x$ -direction.

### Geometry and surface finish

The spatial resolutions of the 10 mm thick detectors with different surface finishes and readout geometries are compared in Table 4.4. Results for the 20 mm thick detectors are presented in Table 4.5. The tables show the FWHM and the

Table 4.3: FWHM and FWTM of cross-sections through measured and corrected PSFs of detector LYSO20-P2, obtained with  $L = 500$ .

	$PSF(x)$		$PSF(y)$	
	FWHM	FWTM	FWHM	FWTM
Measured	1.54	3.33	1.61	3.80
Corrected	1.05	2.09	1.25	2.42

Table 4.4: FWHM and FWTM of global 1D-PSFs measured along the  $x$ - and  $y$ -axis of 10 mm thick detectors with different surface finishes and readout geometries. Results are not corrected for  $d_b = 0.85$  mm FWHM. The estimated uncertainty is  $\sim 0.05$  mm for the FWHM and  $\sim 0.2$  mm for the FWTM ( $2\sigma$ ).

Crystal	Geometry	Peak position (normalised)	1D- $PSF_b(x)$ (mm)		1D- $PSF_b(y)$ (mm)	
			FWHM	FWTM	FWHM	FWTM
LYSO10-P1	front	1.00	1.70	4.52	1.79	4.95
	back	1.09	1.87	5.03	2.08	5.64
LYSO10-P2	front	1.30	1.66	4.54	1.70	4.69
	back	1.25	1.83	5.22	1.93	5.14
LSO10-A	front	0.94	1.73	4.77	1.82	5.31
	back	1.02	2.00	5.56	2.26	6.93
LSO10-E	front	–	1.73	4.57	1.81	4.83
	back	–	1.91	5.20	2.06	5.75

full width at tenth maximum (FWTM) of  $1D-PSF_b(x)$  and  $1D-PSF_b(y)$ , i.e. the 1-dimensional detector PSFs measured along the  $x$ - and  $y$ -axis, respectively. Each 1D-PSF is averaged over all beam positions ('global' PSF) and has been obtained using the value of  $L$  that minimises  $\sigma_{PSF}^*$  (typically,  $100 < L < 1000$ ). The results are not corrected for the beam diameter, which was kept at  $d_b = 0.85$  mm FWHM in all measurements. The estimated  $2\sigma$ -uncertainties of these results are  $\sim 0.05$  mm for the FWHM and  $\sim 0.2$  mm for the FWTM (see Appendix B).

For all 10 mm thick crystals, front-side readout performs better than back-side readout, in agreement with optical simulations presented earlier [70]. Approximately 61% of all 511 keV photons that interact in a 10 mm L(Y)SO crystal do so within the first 5 mm, because of the exponential attenuation of the photon fluence within the scintillator. Events occurring closer to the APD array produce a more sharply peaked light distribution and can be positioned more accurately than events occurring further away. The differences in spatial resolution observed between 10 mm thick crystals with different surface finishes are small compared to the measurement uncertainties. Only the as-cut crystal in back-side readout performs significantly worse than the other crystals.

Average resolutions in the  $y$ -direction (the short crystal axis) are slightly worse than in the  $x$ -direction for both the 10 mm and the 20 mm thick crystals, as was also observed in Table 4.3.

The relative position of the full-energy peak, determined from the analogue sum of the slow outputs of the spectroscopy amplifiers (see figure 4) and normalised to LYSO10-P1, is also given for each crystal in Tables 4.4 and 4.5. The

Table 4.5: FWHM and FWTM of global 1D-PSFs measured along the  $x$ - and  $y$ -axis of 20 mm thick detectors with different surface finishes and geometries. Results are not corrected for  $d_b = 0.85$  mm FWHM. The estimated uncertainty is  $\sim 0.05$  mm for the FWHM and  $\sim 0.2$  mm for the FWTM ( $2\sigma$ ).

Crystal	Peak position (normalised)	1D- $PSF_b(x)$ (mm)		1D- $PSF_b(y)$ (mm)	
		FWHM	FWTM	FWHM	FWTM
LYSO20-P1	0.87	1.81	5.05	1.93	5.56
LYSO20-P2	1.17	1.78	5.07	1.93	5.68
LSO20-A	0.86	1.83	5.19	1.99	6.53
LSO20-E	1.01	1.85	5.27	1.88	5.69
LYSO20T-P	1.35	1.84	5.15	1.88	6.17
LYSO20T-A	1.35	1.86	5.73	1.92	7.09

two 10 mm polished crystals (LYSO10-P1 and LYSO10-P2) perform quite similarly, despite the 30% difference in peak position. The same is observed for the two 20 mm polished rectangular crystals (LYSO20-P1 and LYSO20-P2). It follows that differences in the light yield of several tens of % between the crystals used in a PET system should not significantly affect the uniformity of the spatial resolution of the reconstructed image.

For most 20 mm thick rectangular crystals, the spatial resolution is  $\sim 0.2$  mm FWHM worse than for 10 mm thick detectors in front-side readout, but  $\sim 0.05$  mm FWHM better than for the 10 mm thick detectors in back-side readout. The differences between 20 mm thick rectangular crystals with different surface finishes do not exceed the estimated measurement uncertainties, as was also observed with the 10 mm thick crystals.

The trapezoidal detectors perform similarly well as the rectangular ones. The scans in the  $y$ -direction include the oblique sides of the crystals. In this direction the FWTM of the polished trapezoidal crystal is slightly worse than that of the polished rectangular crystals. The same is found for the as-cut trapezoidal and rectangular crystals. The FWHM values of the as-cut trapezoidal crystal do not differ significantly from those of the polished trapezoidal crystal, but its FWTM values are significantly larger.

### Depth of interaction correction

The DOI correction of the detectors was studied in a series of 1D measurements. Fig. 4.7 shows the FWHM and FWTM of 1D- $PSF_b(x')$  and 1D- $PSF_b(y')$  of the polished trapezoidal crystal LYSO20T-P as a function of the incidence angle  $\theta$ .

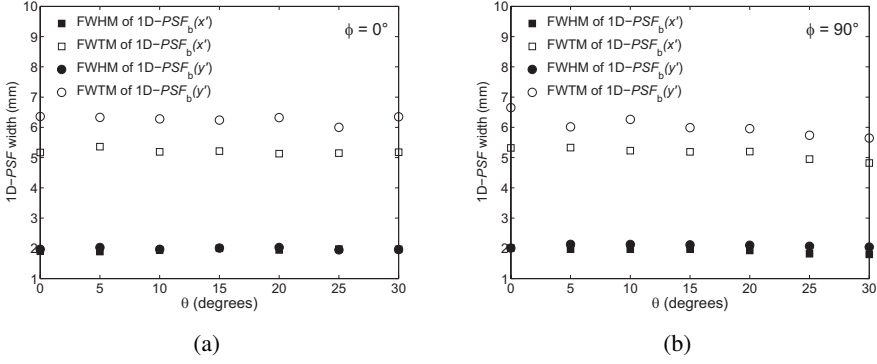


Figure 4.7: FWHM and FWTM of measured 1D-PSFs of LYSO20T-P projected on a plane perpendicular to the test beam, as a function of the angle of incidence  $\theta$ , at (a)  $\phi = 0^\circ$  and (b) at  $\phi = 90^\circ$ . The beam diameter was  $d_b = 0.96$  mm FWHM.

The results are presented in terms of the coordinates  $x'$  and  $y'$  perpendicular to the beam direction, see Section 4.2.4. As in the previous section, the error histograms were averaged over the crystal length to represent the overall detector performance. The values are not corrected for the beam diameter, but care was taken to keep  $d_b$  constant in all measurements. The source was moved some distance away from the detector box to accommodate for its rotation, so that  $d_b = 0.96$  mm FWHM. As a result, the values presented here cannot be directly compared to those in Table 4.5.

At  $\phi = 0^\circ$ , both  $1D-PSF_b(x')$  and  $1D-PSF_b(y')$  are essentially independent of  $\theta$ . At  $\phi = 90^\circ$ ,  $1D-PSF_b(x')$  can even be seen to slightly improve with increasing  $\theta$ . This is attributed to the fact that the beam exits the side surface of the crystal at large values of  $\theta$ , reducing the average distance of interaction from the front APD array. Similar results were found for the rectangular crystals, although the difference between the FWTMs of  $1D-PSF_b(x')$  and  $1D-PSF_b(y')$  were smaller for these crystals, in accordance with the results given in the previous section.

The DOI correction of these detectors requires that the angle of incidence of the unknown photon be known, so that the appropriate set of reference data can be used to estimate its entry point coordinates. It has been shown elsewhere that this angle can be derived from the positions of the two detectors triggering in coincidence in a PET ring [72]. The excellent intrinsic DOI correction of these detectors can therefore be expected to yield essentially parallax-free image reconstruction for angles of incidence of up to at least  $30^\circ$ .

## 4.4 Conclusions

In this chapter, the performance of monolithic scintillator PET detectors has been characterised experimentally in terms of the detector spatial, temporal and energy resolutions. At the centre of the detector and at normal incidence, the FWHM of the detector PSF obtained with a rectangular crystal is as good as  $\sim 1.05$  mm in the  $x$ -direction, after correction for the  $\sim 0.9$  mm FWHM diameter test beam of annihilation photons. Some resolution loss occurs near the edges of the detectors, in the direction perpendicular to the crystal edge.

Trapezoidal crystals were found to perform almost as well as rectangular ones. A trapezoidal crystal shape minimises the dead space within a detector ring, resulting in a high and uniform scanner sensitivity.

No loss of spatial resolution is observed for angles of incidence of up to at least  $30^\circ$ . Hence, an excellent and highly uniform PET system resolution may be expected using this monolithic detector design.

These promising results were obtained at  $E_{\text{th}} \approx 100$  keV, implying that a low energy threshold can be used to maximise system sensitivity when imaging small subjects (with low intra-subject scattering), without loss of resolution. Energy resolutions of  $\sim 11\%$  FWHM are measured with  $\sim 75\%$  of the events in the full-energy peak. The estimated coincidence timing resolution of  $\sim 2.8$  ns FWHM is sufficient for adequate rejection of random coincidences [73].

The intrinsic detector spatial resolution of 1.05 mm FWHM obtained with the  $20 \times 10 \times 20$  mm<sup>3</sup> detector is not as narrow as the smallest crystal pitch currently reported in high-resolution PET detectors based on matrices of small scintillator crystals [48]. However, the results presented here suggest that a high and uniform spatial resolution of the reconstructed image at a very high scanner sensitivity may be achievable with monolithic scintillator detectors. This makes these detectors promising candidates for future high-resolution PET scanner designs. A Monte Carlo simulation study of small-animal PET scanners based on these detectors, using measured 1D-PSFs and other parameters as input, is presented in Chapter 7.





# Chapter 5

## Signal to Noise Ratio<sup>1</sup>

### Abstract

Monolithic scintillator detectors, consisting of several cm<sup>3</sup> of scintillating material coupled to one or more Hamamatsu S8550 avalanche photodiode (APD) arrays are proposed as detectors for high resolution positron emission tomography (PET). In this chapter, the factors contributing to the variance on the signals are investigated, and their effects on the energy, time and spatial resolutions are analysed.

Good agreement is found between a model of the energy resolution and experiments with a 20×10×10 mm<sup>3</sup> LYSO:Ce crystal coupled to a single channel large-area APD (LAAPD). With the same crystal coupled to an APD array, differences between model and experiment are observed at high APD gain.

The measured energy resolution of ~11% FWHM is shown to be dominated by scintillation photon statistics, with less important roles for excess noise factor and electronic noise. On the other hand, electronic noise is an important factor both for the time and the spatial resolutions. The timing resolution is found to depend strongly on the APD bias voltage, and is best at the highest bias. A timing resolution of 1.6 ns full width at half maximum (FWHM) is measured against a BaF<sub>2</sub>-PMT detector. The best spatial resolution measured is 1.64 mm FWHM, without correction for the ~0.9 mm FWHM measurement beam. It is estimated that an intrinsic spatial resolution of 1.26 mm FWHM can be achieved at the

---

<sup>1</sup>This chapter is adapted from M. C. Maas, D. R. Schaart, D. J. van der Laan, H. T. van Dam, J. Huizenga, J. C. Brouwer, P. Bruyndonckx, C. Lemaître and C. W. E. van Eijk, "Signal to noise ratio of APD-based monolithic scintillator detectors for high resolution PET," *IEEE Transactions on Nuclear Science*, vol. 55, pp. 842–852, 2008.

centre of the detector with an infinitely narrow test beam.

## 5.1 Introduction

Positron emission tomography (PET) has gained a lot of interest in recent years as a molecular imaging tool for research on small animals such as rats and mice. The small dimensions of the organs of these animals impose stringent requirements on the spatial resolution and sensitivity of dedicated PET systems. Many current detector designs rely on small scintillation crystals to obtain the best possible spatial resolution [48, 53, 61, 74–81]. However, the scanner sensitivity is reduced in such designs due to the dead space between the individual crystals. Additionally, the spatial resolution may be deteriorated by inter-crystal scatter and parallax errors due to depth of interaction (DOI) effects.

To avoid these problems, monolithic scintillator detectors were proposed [18, 19]. These detectors consist of several  $\text{cm}^3$  of scintillating material coupled to one or more avalanche photodiode (APD) arrays (see Fig. 5.1). The entry point of an incoming annihilation photon on the front surface of the detector can be derived from the distribution of the scintillation light on the APD arrays. Because there are no individual crystal segments, sensitivity loss due to reflective material between the crystals is avoided.

Preliminary research on these detectors yielded promising results. A detector spatial resolution of  $\sim 2.0$  mm FWHM, not corrected for the  $\sim 1$  mm FWHM measurement beam was achieved with a 20-mm thick detector, with only a slight deterioration for angles of incidence up to  $30^\circ$ , see Chapter 4. This indicates that a thick layer of scintillating material can be used to maximise sensitivity, without deterioration of the image spatial resolution by parallax errors.

The aim of the present work is to gain a better understanding of the influence of signal variances on the detector energy, timing and spatial resolutions, and of the factors that contribute to these signal variances. As the energy resolution represents a direct measure of a detector's signal-to-noise ratio (SNR), a model of this quantity for scintillator-APD detectors is presented first. This model is initially verified experimentally using a single channel large-area APD (LAAPD), in order to avoid effects such as differences in gain or excess noise factor between the individual channels of the APD arrays. It is subsequently applied to the APD array detectors. Furthermore, analyses of the electronic noise and the timing resolution of the APD array detectors are presented, and the influence of the signal variance on the spatial resolution is investigated.

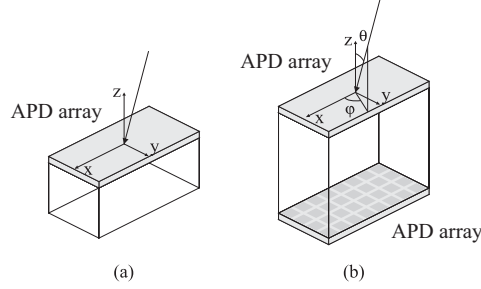


Figure 5.1: Schematic representation of the detectors investigated. On the 10-mm thick crystals (a), the APD array was coupled to the side facing the beam. On the 20-mm thick crystals (b), the arrays were coupled to opposing sides.

## 5.2 Models

### 5.2.1 Energy resolution

For a scintillator coupled to an APD, the mean number of electrons  $\bar{N}_e$  produced at the APD output due to incident radiation producing an average of  $\bar{N}_{ph}$  scintillation photons per event can be written as

$$\bar{N}_e = \eta \cdot \bar{M} \cdot \bar{N}_{ph}, \quad (5.1)$$

where  $M$  is the APD multiplication gain, and  $\eta$  represents the number of primary e-h pairs generated in the APD per scintillation photon, averaged over all photons per scintillation event and over all events. In this formula,  $\bar{N}_{ph}$  and  $\bar{N}_e$  represent averages over many events, while  $\bar{M}$  is averaged over all primary electron-hole (e-h) pairs created in the APD conversion layer.

The energy resolution of this system, defined as the full width at half maximum (FWHM) of the full-energy peak divided by its centroid location, can be described by four terms. The first of these represents the variance in the number of photons generated per scintillation event, the second represents the added variance due to the conversion of scintillation photons to primary e-h pairs in the APD, the third represents the APD multiplication variance, and the fourth represents the contribution of electronic noise [82]:

$$\frac{\Delta E}{E} = 2.35 \left( \frac{\text{var}\{N_{ph}\}}{\bar{N}_{ph}^2} + \frac{1 - \eta}{\eta \bar{N}_{ph}} + \frac{1}{\eta \bar{N}_{ph}} \frac{\text{var}\{M\}}{\bar{M}^2} + \frac{ENC^2}{(\eta \bar{M} \bar{N}_{ph})^2} \right)^{1/2}, \quad (5.2)$$

where  $\Delta E/E$  is the FWHM energy resolution, and  $ENC$  is the equivalent noise charge of the detector-amplifier system referred to the preamplifier input.

Due to e.g. non-proportionality of the scintillator electron response, the variance of  $N_{ph}$  is often greater than what would be expected based on Poisson statistics. In this work, this broadening is represented by an excess variance factor  $\alpha^2$  describing the observed photon variance relative to the Poisson variance:

$$\alpha^2 = \frac{\text{var}\{N_{ph}\}}{\overline{N}_{ph}}. \quad (5.3)$$

Assuming that this term is independent of the energy of the incident radiation in the range of energies considered in this work (511–662 keV), the same value of  $\alpha$  can be used for model calculations at different energies. This assumption may be invalid at lower energies. This approach is also followed in the Monte Carlo code Geant4 [83] used in our simulations of monolithic scintillator detectors [70], and is included in this experimental model for ease of comparison.

The variance associated with the multiplication process in the APD is commonly expressed in terms of the excess noise factor  $J$ , which is defined as:

$$J \equiv \frac{\text{var}\{M\}}{\overline{M}^2} + 1. \quad (5.4)$$

Using Eq. (5.2)–Eq. (5.4), the energy resolution may now be written as:

$$\frac{\Delta E}{E} = 2.35 \left( \frac{\alpha^2 - 1}{\overline{N}_{ph}} + \frac{J}{\overline{N}_e/\overline{M}} + \frac{ENC^2}{\overline{N}_e^2} \right)^{1/2}. \quad (5.5)$$

The first term in this equation represents the deviation from Poisson statistics of the number of scintillation photons produced per event. The Poisson statistics are contained in the second term, where the factor  $\overline{N}_e/\overline{M} = \eta \overline{N}_{ph}$  represents the number of primary e-h pairs.

### 5.2.2 Equivalent noise charge

Assuming equal shaping time constants for differentiation and integration, the squared equivalent noise charge of a radiation detector-amplifier system can be written as [84]:

$$ENC^2 = \frac{1}{q^2} \left( \frac{aC_{tot}^2 A_1}{\tau} + \left[ 2\pi a_f C_{tot}^2 + \frac{b_f}{2\pi} \right] A_2 + bA_3 \tau \right), \quad (5.6)$$

where  $a$  is the spectral density of the series white noise,  $b$  is the spectral density of the parallel white noise,  $a_f$  is the coefficient of the series  $1/f$  noise, and  $b_f$  is the coefficient of parallel  $1/f$  noise.  $C_{\text{tot}}$  is the total input capacitance of the detector-preamplifier system,  $q$  is the elementary electron charge,  $\tau$  is the amplifier shaping time, and  $A_1$ – $A_3$  are dimensionless constants depending on the type of shaping network. A mathematical frequency range is assumed in this model:  $-\infty < f < +\infty$ .

The series white noise contribution is mainly due to thermal noise of the preamplifier input FET channel and may be written as [85]:

$$a = \Gamma \frac{2k_b T}{g_m}, \quad (5.7)$$

where  $g_m$  is the FET transconductance,  $k_b$  is Boltzmann's constant,  $T$  is the temperature and  $\Gamma$  is the FET channel form factor, having values ranging between 0.5 and 0.7.

The parallel white noise contribution  $b$  consists mainly of shot noise related to leakage currents through the detector and the preamplifier FET gate, and of thermal noise of the preamplifier feedback resistor. For a detector with internal amplification such as an APD, a distinction can be made between unamplified (surface) leakage current  $I_{\text{ls}}$  and amplified (bulk) leakage current  $I_{\text{lb}}$ , resulting in a total detector leakage current of [86]:

$$I_l = I_{\text{ls}} + M I_{\text{lb}} \quad (5.8)$$

Taking into account that the amplified portion of the leakage current also experiences the APD excess noise factor, the total white parallel noise contribution may be written as:

$$b = q \left( I_{\text{lg}} + I_{\text{ls}} + J \overline{M}^2 I_{\text{lb}} \right) + \frac{2k_b T}{R_f}. \quad (5.9)$$

where  $I_{\text{lg}}$  is the FET gate leakage current and  $R_f$  is the preamplifier feedback resistance.

### 5.2.3 Timing resolution

The timing resolution of a pair of detectors can be determined by measuring the distribution of time differences between prompt coincident events. In this work, the timing resolution of the LYSO-APD array detectors is measured against a fast PMT detector, so that the variance of this distribution can be written as:

$$\sigma_t^2 = \sigma_A^2 + \sigma_P^2, \quad (5.10)$$

where  $\sigma_A^2$  and  $\sigma_P^2$  are the variances introduced by the APD array detector and the PMT detector, respectively. The variance in the time pickoff of each of these detectors consists of contributions related with time variations in the interaction of the radiation with the detectors, variations in the amplitude and shape of the scintillation pulse, time variations induced by its detection and the associated electronics, and the time pickoff method [87]. The first of these contributions is neglected in this analysis in view of the small dimensions of the detectors.

When a constant fraction discriminator (CFD) is used for time-pickoff, the uncertainty of the zero-crossing time of its output bipolar pulse can be related to the signal fluctuations and the signal slope at the zero-crossing point, according to [88]:

$$\sigma_{t_0} = \left( \frac{\sigma_v}{dv/dt} \right)_{t=t_0} \quad (5.11)$$

where  $\sigma_v$  denotes the rms signal fluctuation,  $dv/dt$  denotes the signal slope and  $t_0$  represents the zero-crossing time.

In the LYSO-APD array detector, the signal fluctuations described by  $\sigma_v$  may be caused by statistical fluctuations in the pulse amplitude and shape, and by electronic noise. It is assumed that pulse amplitude variations are cancelled by the CFD. Additionally, the large number of primary e-h pairs that are multiplied in the APD and integrated on the preamplifier feedback capacitance in each scintillation pulse, combined with the short scintillation decay time of LYSO ( $\sim 40$  ns) and the limited bandwidth of the preamplifier-fast amplifier system, result in a negligible contribution of pulse shape walk. Hence, it is assumed that only electronic noise contributes to  $\sigma_v$ .

The signal slope at the zero-crossing point is assumed to be proportional to the ratio of the pulse amplitude and rise time. The pulse amplitude is given by the pulse height in response to a single input electron,  $V'_{pk}$ , times  $N_e$ . In the ratio  $\sigma_v/V'_{pk}$ , the definition of equivalent noise charge is recognised. Hence, it follows that

$$\sigma_A \sim \frac{ENC_f}{N_e/t_r}, \quad (5.12)$$

where  $t_r$  denotes the pulse rise time and the 'f' subscript is used to indicate the fast amplifier branch. Hence, to optimise the timing resolution, the product of  $ENC_f$  and  $t_r$  should be minimised.

### 5.2.4 Spatial resolution

In addition to scattering of the incident radiation inside the crystals, the SNR of the detector signals forms one of the main contributions to the detector spatial

resolution [89]. To investigate the probability distribution of the positioning error due to statistics and electronic noise for a given, arbitrary event, it is assumed that (1) the covariance between the detector channels may be neglected, and (2) the probability distribution of the positioning error depends on the SNR of the signals measured for that given event only. A detailed statistical analysis of the spatial resolution obtainable with these detectors, which also takes the covariance between the channels into account, is presented elsewhere [90]. It is shown there that assumption (1) is indeed valid for the detectors investigated here. Assumption (2) can be justified by considering that the set of training data used by the positioning algorithm employed is large (see Section 5.3.3), rendering the effects of statistics and noise in this latter set negligible [89,91].

Summarising, the probability distribution of the positioning error due to statistics and electronic noise of an event with (a) given energy deposition(s) at given location(s) in the crystal is assumed to depend only on the SNR per channel of that same event. For this given event, the photon detection efficiency  $\eta_i$  of a channel  $i$  is defined as the expectation value of the number of e-h pairs generated in APD pixel  $i$  divided by the expectation value of the number of emitted scintillation photons that corresponds to the energy deposited in the event. If this energy corresponds to an expectation value of the number of emitted scintillation photons equal to  $\bar{N}_{\text{ph}}$ , the relative signal variance in channel  $i$  can be derived using Eq. (5.2), substituting  $\eta_i$  for  $\eta$ :

$$\begin{aligned} \left(\frac{\sigma_i}{\mu_i}\right)^2 &= \frac{\text{var}\{N_{\text{ph}}\}}{\bar{N}_{\text{ph}}^2} + \frac{1 - \eta_i}{\eta_i \bar{N}_{\text{ph}}} \\ &+ \frac{1}{\eta_i \bar{N}_{\text{ph}}} \frac{\text{var}\{M\}}{\bar{M}^2} + \frac{ENC_i^2}{(\eta_i \bar{M} \bar{N}_{\text{ph}})^2}, \end{aligned} \quad (5.13)$$

where  $\mu_i$ ,  $\sigma_i$  and  $ENC_i$  represent the signal expectation value and standard deviation and the equivalent noise charge of channel  $i$ , respectively.

To assess the relative importance of each of the terms in Eq. (5.13), a hypothetical event is considered with the same total energy deposited, for which  $\eta_i = \eta/n$ , where  $n$  is the number of detector channels. Thus, the light distribution of this event is expected to be uniform over the detector pixels. The independence of the electronic noise in the detector channels results in  $ENC_i = ENC/\sqrt{n}$ . This leads to the following expression:

$$\left(\frac{\sigma_i}{\mu_i}\right)^2 = \frac{\alpha^2 - 1}{\bar{N}_{\text{ph}}} + n \frac{J}{\bar{N}_e \bar{M}} + n \frac{ENC^2}{\bar{N}_e^2}. \quad (5.14)$$

Table 5.1: List of crystals used in the experiments.

Sample	Material	Dimensions (mm <sup>3</sup> )	Vendor
LYSO10-P1	LYSO(Ce)	20×10×10	Photonic Materials
LYSO10-P2	LYSO(Ce)	20×10×10	CrystalPhotonics
LYSO20-P1	LYSO(Ce)	20×10×20	Photonic Materials
LYSO20-P2	LYSO(Ce)	20×10×20	CrystalPhotonics

Thus, for this hypothetical situation, the relative importance of the terms representing excess noise and electronic noise is increased by a factor  $n$  compared to Eq. (5.5), while the term corresponding to the excess scintillation photon variance remains unaltered. It is assumed that the relative influence of the various terms on the spatial resolution indicated by Eq. (5.14) is representative for other, arbitrary, events.

## 5.3 Materials

### 5.3.1 Crystals

The crystals investigated in this work are listed in Table 5.1. The sample names consist of the crystal material followed by the thickness in mm, a letter representing the surface finish and a sample number. The crystals used in this work were all polished, represented by the letter P. The photon statistics contribution  $(\alpha^2 - 1)/\overline{N}_{\text{ph}}$  of these crystals was measured on a PMT (Hamamatsu R1791), using an Ortec 672 shaping amplifier set to a shaping time of 1  $\mu\text{s}$  and an Ortec AD114 ADC.

### 5.3.2 LAAPD

LAAPD measurements were performed using an Advanced Photonix LAAPD model 630-70-73-510, serial no. 128-10-11 [92], see Table 5.2. It was contained in a temperature controlled box, and was read out using a Goyot preamplifier [93], an Ortec 672 shaping amplifier set to a shaping time of 1  $\mu\text{s}$  and an Ortec AD114 ADC. Energy resolution measurements were performed with crystal LYSO10-P2, packed in Teflon powder, with a  $10 \times 10 \text{ mm}^2$  face optically coupled to the  $\varnothing 16 \text{ mm}$  LAAPD.



### 5.3.3 APD arrays

The APD arrays used in this work are Hamamatsu model S8550-SPL, serial numbers 036 and 037, see Table 5.2. These arrays consist of 2 banks of  $2 \times 8$  pixels measuring  $1.6 \times 1.6$  mm<sup>2</sup>, at a pitch of 2.3 mm [94].

Each bank has a specific bias voltage  $V_{50}$  at which the mean channel gain  $\langle M \rangle = 50$  according to manufacturer specifications. Between banks in the same array, and between different arrays, differences in  $V_{50}$  of 10–20 V are common. In this work, the bias voltage of the arrays is therefore expressed in terms of  $\Delta V \equiv V - V_{50}$ , where  $V$  is the applied bias voltage. The average gains  $\langle M \rangle$  of the individual banks of the APD arrays used in this work, measured as a function of  $\Delta V$  using 5.89 keV X-rays from an <sup>55</sup>Fe-source, were found to coincide within 4% between  $\Delta V = -40$  V and  $\Delta V = +10$  V (see Appendix A). Breakdown effects started to occur at approximately  $\Delta V = 18$  V.

The experimental setup used to investigate the LYSO-APD array detectors is depicted in Fig. 5.2. The detectors are contained in a light-tight Al box, which is held at a constant temperature using Peltier coolers. To define a narrow beam of 511 keV photons, a  $\varnothing 0.5$  mm <sup>22</sup>Na-source is used, and a second detector, consisting of a  $\varnothing 19 \times 35$  mm<sup>3</sup> BGO crystal coupled to a PMT (XP2020) equipped with a Pb collimator, is used in coincidence with the APD detector. The width of the photon beam can be controlled by varying the distance between the PMT and the source. The 32 or 64 APD signals are each individually preamplified by Cremat CR-110 charge-sensitive preamplifiers (CSPs). Further amplification and shaping is provided by several CAEN N568BB 16-channel shaping amplifiers, which have a fast and a slow output branch. The slow output branch has a CR-(RC)<sup>2</sup> shaping network with an adjustable gain and shaping times of 0.1, 0.2, 1 and 3  $\mu$ s; the fast output branch is a fixed-gain single differentiation stage with a time constant of 100 ns. A schematic representation of the front-end electronics is shown in Fig. 5.3.

Measurements of the equivalent noise charge and the energy resolution were performed on the analog sum signal of the slow amplifier outputs. Pulse height spectra were obtained using an Ortec AD413A ADC.

Timing resolution measurements were performed against a  $\varnothing 25.4 \times 25.4$  mm<sup>3</sup> BaF<sub>2</sub> crystal coupled to an XP2020Q PMT. The PMT signal was directly fed into a constant fraction discriminator (CFD, Ortec 934) for time pickoff. Time pickoff on the APD detectors was performed by feeding the analog sum of the fast outputs of the linear amplifiers to a CFD, via a timing filter amplifier (TFA, Ortec 454) with a variable integration time constant. The time spectra were measured using a time-to-amplitude converter (TAC, Ortec 476), and an Ortec AD413A ADC. The

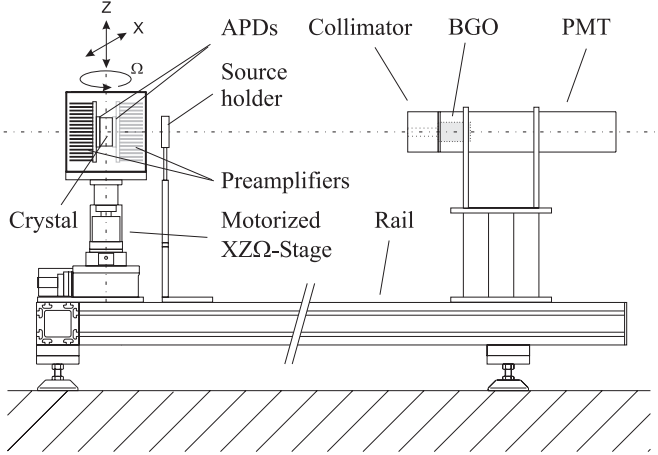


Figure 5.2: Schematic representation of the experimental setup used to analyse the APD array detectors.

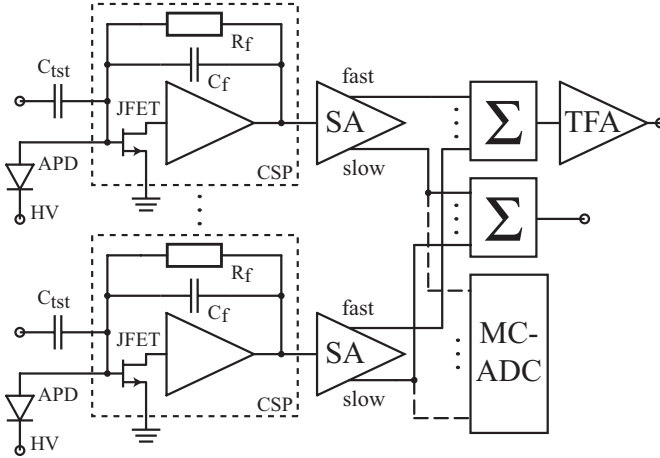


Figure 5.3: Schematic representation of the front-end electronics. CSP: charge-sensitive preamplifier; SA: shaping amplifier; TFA: timing filter amplifier; MC-ADC: multichannel ADC.

Table 5.2: Characteristics of the LAAPD and the APD arrays.

Device	LAAPD	APD arrays
Manufacturer	Advanced Photonics	Hamamatsu
Type	630-70-73-510	S8550 SPL
Sensitive area	Ø16 mm circular	$32 \times 1.6 \text{ mm} \times 1.6 \text{ mm}$
Gain <sup>a</sup>	200 at 1850 V	50 at 400 V
Dark current <sup>a</sup>	280 nA at Gain 200	10 nA / ch at Gain 50
Capacitance <sup>a</sup>	130 pF	10 pF per channel

<sup>a</sup> Typical values

time axis was calibrated with an Ortec 462 time calibrator.

Positional information can be extracted from the distribution of scintillation light on the APD arrays in each event. To record these, multichannel ADCs (CAEN V785) were used to read out each slow-output channel separately.

## 5.4 Methods

### 5.4.1 Scintillation photon variance

The scintillation photon statistics term  $(\alpha^2 - 1)/\overline{N}_{\text{ph}}$  was calculated for the crystals investigated by subtracting the PMT multiplication variance, calculated from the single electron spectrum, from the measured energy resolution [95]. The electronic noise contribution was assumed to be negligible.

### 5.4.2 LAAPD energy resolution

The energy resolutions measured with crystal LYSO10-P2 coupled to the LAAPD were compared to calculated values. These were obtained by inserting separately measured values of the individual contributions into Eq. (5.5).

To measure the LAAPD gain, the peak positions of spectra recorded with a pulsed laser (Hamamatsu C5143,  $\lambda = 667 \text{ nm}$ ) were compared to the peak position at  $V = 400 \text{ V}$ , where unity gain was assumed.

The excess noise factor was determined by measuring the energy resolution of the laser pulser at fixed LAAPD gain as a function of the number of output electrons, by inserting optical filters between the light source and the LAAPD, thus effectively varying  $\eta$ . The energy resolution observed with the laser pulser

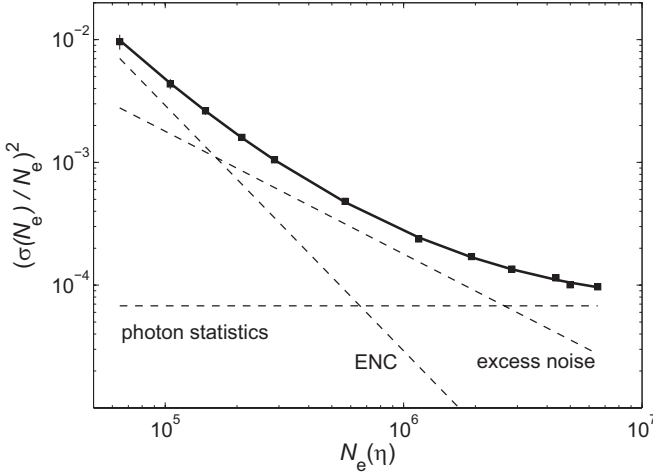


Figure 5.4: Energy resolution of the laser pulser as a function of the number of output electrons, at a constant LAAPD gain of  $\sim 95$ . The solid line represents a least squares fit to the data using Eq. (5.15); the dashed lines indicate the individual components.

can be written as (see Eq. (5.2) and Eq. (5.5)):

$$\left( \frac{\sigma(N_e)}{N_e} \right)^2 = h_1 + \frac{h_2}{N_e} + \frac{h_3}{N_e^2}, \quad (5.15)$$

where  $h_1 = \text{var}\{N_{\text{ph}}\} / \bar{N}_{\text{ph}}^2 - 1 / \bar{N}_{\text{ph}}$  is the deviation from Poisson statistics of the distribution of the number of photons produced per laser pulse. This term remains constant during the experiment. The term  $h_2 = J\bar{M}$  describes the excess noise contribution, and  $h_3 = \text{ENC}^2$  represents the electronic noise. The excess noise factor can thus be obtained by least-squares fitting this model to the data. An example of this type of experiment, performed at  $M \sim 95$ , is presented in Fig. 5.4. It is noted that with this method, no model terms need to be neglected, and no assumptions about the underlying statistics of photons or electron-hole pairs are made.

### 5.4.3 APD arrays

#### Equivalent noise charge

The electronic noise of the APD arrays was investigated by measuring the equivalent noise charge at various APD bias and amplifier shaping time settings. Measurements were performed by injecting charge into calibrated  $\sim 1.8$  pF capacitors at each of the CSP test inputs using a square wave test pulser and obtaining pulse height spectra of the analog sum of the slow amplifier output signals.

#### Timing resolution

The influence of electronic noise and amplifier shaping on timing was investigated by measuring the timing resolution at various TFA integration time settings. The influence of the APD bias voltage on the timing resolution was also investigated.

#### Energy resolution

Measurements of the energy resolution were performed at 511 keV with the crystals listed in Table 5.1. Calculations according to Eq. (5.5) were also done, again using separately measured values of the individual contributions.

Measurement of the gain of the APD arrays is not straightforward. Gain measurements using an optical source such as an LED or a pulsed laser are complicated by the fact that at low bias voltage, where unity gain is assumed, the pixels of the array are not fully depleted [86]. The possible change in the effective sensitive volume of the pixels with increasing bias voltage and the optical crosstalk caused by the 0.5 mm epoxy window in front of the pixels cause an uncertainty in the measured gain. These effects are illustrated by the significant differences reported between gain measurements with and without  $\varnothing 1.3$  mm masks in front of the arrays [96].

To avoid these issues, the APD gain was measured with 5.89 keV X-rays from a  $^{55}\text{Fe}$ -source in this work. X-ray measurements can however result in a significantly lower gain than measurements with optical photons. This effect depends on the X-ray energy, the APD gain and the device structure [97, 98], and has indeed been observed for the S8550 arrays at 5.89 keV [37].

The uncertainties in the gain measurements with an optical source preclude determination of the excess noise factor using the method described above. Determination of the ENF from X-ray data is complicated by effects of non-uniformity of the gain over the detection area of each APD pixel. This effect can add significantly to the peak width observed with X-rays, but is averaged out when detecting

optical photons which are spread over the whole detection area in each event [99]. An excess noise factor of  $\sim 1.75$  has been reported elsewhere for these arrays, nearly independent of the APD gain [37]. This value was adopted in this work.

The model term  $\bar{N}_e/\bar{M}$  describes the mean number of primary e-h pairs per scintillation event and is thus independent of  $M$ . The term was determined by comparing the peak position of the pulse height spectrum with that of a square-wave test pulser. This was done at a low gain ( $M \sim 18$ ), where the difference between optical and X-ray gain is assumed to be small.

## Spatial resolution

Spatial resolution measurements were performed by scanning the detectors through the beam in steps of 0.25 mm along the  $x$  or the  $y$  axis of the crystals at normal incidence (see Fig. 5.1). At each beam position, 1500 light distributions were recorded, consisting of 32 or 64 channel values from the multichannel ADCs. The coordinate of each event was estimated with a statistical learning algorithm based on the nearest neighbor method [68], using the rest of the same data set as training data (leave-one-out approach). With both the estimated and the real beam coordinates known, a histogram of the positioning errors can be created. The FWHM and FWTM of the overall error histogram containing all events in a data set served as a measure of the spatial resolution for the purposes of this work. These numbers were obtained by linear interpolation of the histograms. This position estimation algorithm and its performance optimisation are described in more detail elsewhere [71]. In the present work, the position estimation algorithm was operated using 500 nearest neighbors.

## 5.5 Results and discussion

### 5.5.1 Scintillation photon variance

The photon statistics contribution  $(\alpha^2 - 1)/\bar{N}_{\text{ph}}$  was measured both at 662 keV and at 511 keV. For constant  $\alpha$ , the ratio of both photon statistics terms should equal the ratio of the photon yields, i.e.  $662/511 = 1.295$ . Experimentally, a ratio of 1.285 was observed, indicating that  $\alpha$  may indeed be regarded constant in the energy range considered.

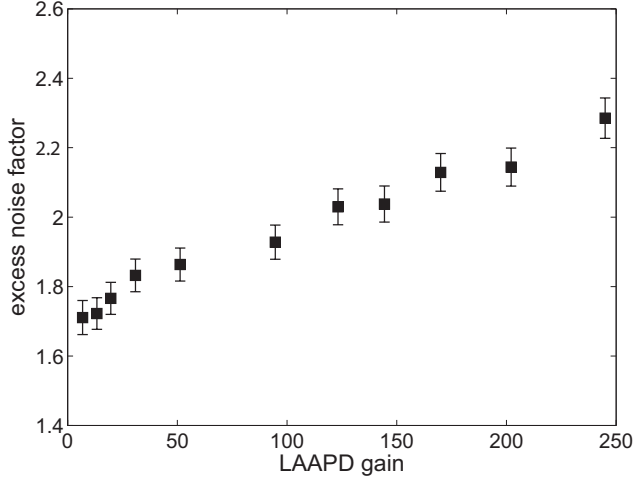


Figure 5.5: Excess noise factor of the LAAPD as a function of the gain. The error bars indicate a  $1\sigma$  uncertainty.

### 5.5.2 LAAPD energy resolution

The excess noise factor of the LAAPD is plotted as a function of the gain in Fig. 5.5. A comparison of the calculated and measured energy resolutions of crystal LYSO10-P2 at 662 keV and 511 keV as a function of the LAAPD gain is presented in Fig. 5.6. Good agreement between calculation and experiment is observed at both energies.

### 5.5.3 APD arrays

#### Equivalent noise charge

Fig. 5.7 shows measurements of the equivalent noise charge of a single detector channel as a function of the nominal amplifier shaping time, at several APD bias voltages. At  $\Delta V = 0$  V, the best  $ENC$  is found at  $\tau = 0.1 \mu\text{s}$  with a value of  $\sim 550 \text{ e}^-$  rms. The same measurement performed on the analog sum signal of 64 channels yielded an average of  $\sim 600 \text{ e}^-$  per channel.

It is customary to fit the data of Fig. 5.7 to the model in Eq. (5.6) in order to estimate the individual noise contributions. However, it was found that the pulse shapes produced by the spectroscopy amplifiers are not the same for every shaping

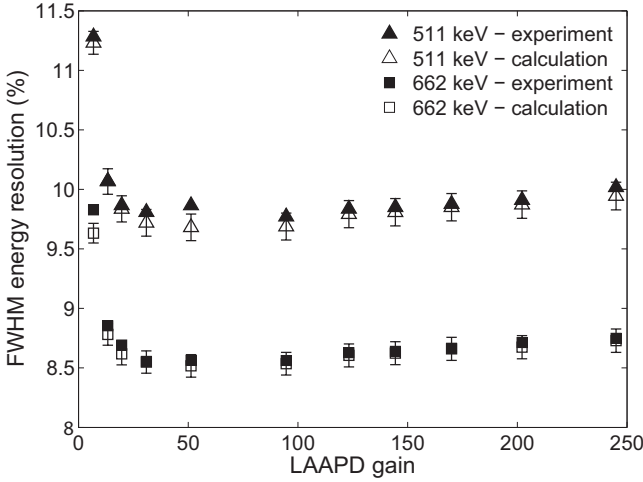


Figure 5.6: Measured and calculated energy resolution of crystal LYSO10-P2 coupled to the LAAPD as a function of the gain, at 662 keV and 511 keV. The error bars indicate a  $1\sigma$  uncertainty. The error bars of the experimental data fall within the markers.

time setting. This implies that the factors  $A_1$ – $A_3$  in Eq. (5.6) are not the same for every shaping time, making fitting meaningless.

The noise component proportional to  $\tau$  rises with increasing  $\Delta V$ , as can be seen in Fig. 5.7. This is due to increasing amplification of the bulk leakage current through the APD, and possibly an increasing excess noise factor (see Eq. (5.6) and Eq. (5.9)). The APD capacitance hardly changes in the voltage range considered [86], implying that the  $1/\tau$ -proportional series white noise and the  $\tau$ -independent  $1/f$  series noise components remain nearly constant. Because of these effects, the optimum shaping shifts to shorter time constants with increasing  $\Delta V$ , as can be observed in Fig. 5.7.

The thermal noise of the CSP feedback resistor is given by the last term in Eq. (5.9). With  $R_f = 100 \text{ M}\Omega$  and  $T = 300 \text{ K}$ , we find  $2k_b T/R_f = 8.3 \cdot 10^{-29} \text{ A}^2/\text{Hz}$ . The surface and bulk leakage currents  $I_{ls}$  and  $I_{lb}$  of the same type of APD were measured elsewhere [86], yielding values of  $0.4 \text{ nA}$  and  $0.02 \text{ nA}$ , respectively. According to the CSP manufacturer,  $I_{lg}$  is much smaller than the APD leakage currents, and may be neglected. At  $M = 50$ , and assuming that  $J = 1.75$  [37], Eq. (5.9) then yields a parallel white noise contribution due only to detector leakage currents of  $1.4 \cdot 10^{-26} \text{ A}^2/\text{Hz}$ . The feedback resistor thermal noise may thus



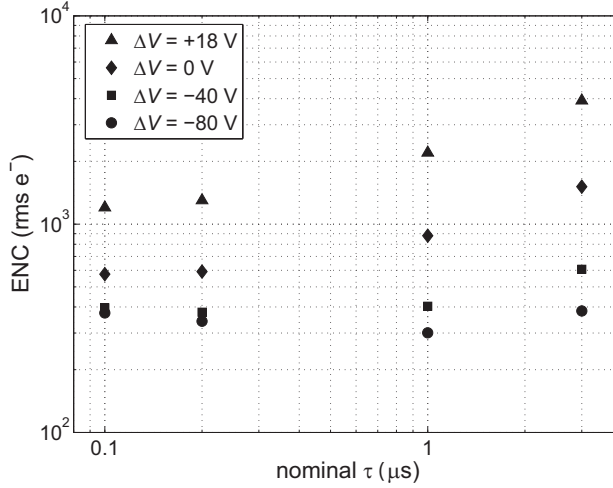


Figure 5.7: ENC of a single detector channel as a function of the nominal amplifier shaping time  $\tau$  at various APD bias voltages.

be neglected.

### Timing resolution

In our experiments, the time constants for differentiation and integration are in general unequal in the fast branch, because the differentiation time constant is fixed. Consequently, a more complex expression for  $ENC_f$  than Eq. (5.6) applies, see Appendix C. However, increasing  $M$  increases the parallel noise in this branch also, causing the integration time constant  $\tau_i$  that minimises  $ENC_f$ , and also the  $\tau_i$  that optimises timing, to shift towards shorter time constants. In Table 5.3, the timing resolution as a function of  $\tau_i$  is presented at two bias voltage settings, as well as the 10%–90% rise time of the signals. The uncertainty on these timing measurements was approximately 0.1 ns. Although small, the expected effect is indeed observed: at  $\Delta V = -20$  V, the best timing is achieved at  $\tau_i = 20$  ns, while at  $\Delta V = +16$  V, this is at  $\tau_i = 2$ –5 ns.

Timing resolution measurements as a function of the APD bias, up to close to the breakdown voltage ( $\Delta V_b \sim 18$  V) are shown Fig. 5.8 for crystals LYSO10-P2 (10 mm, 32 channels) and LYSO20-P2 (20 mm, 64 channels). These measurements were performed with  $\tau_i = 2$  ns and an energy threshold of 250 keV. Due to its increased number of noise sources, the timing resolution of the 64-channel

Table 5.3: Timing resolution of LYSO20-P2 as a function of  $\tau_i$  at different bias voltages.

$\tau_i$ (ns)	$t_r$ (10%–90%) (ns)	Timing resolution (ns)	
		$\Delta V = -20$ V	$\Delta V = +16$ V
2	40	7.8	2.3
5	40	7.6	2.3
10	41	7.6	2.4
20	44	7.5	2.4
50	64	7.8	2.6

detector is poorer than that of the 32-channel detector. The strong dependence on  $\Delta V$  observed in both cases may be understood by rewriting Eq. (5.12), splitting  $ENC_f$  in an unamplified and an amplified part, and using the fact that  $\bar{N}_e$  is directly proportional to  $\bar{M}$ :

$$\sigma_A \propto \frac{\sqrt{\beta_1 + \beta_2 J \bar{M}^2}}{\bar{M}/t_r}. \quad (5.16)$$

Here,  $\beta_2$  accounts for the component of the parallel white noise that is amplified in the APD, while  $\beta_1$  contains all other, unamplified, noise components (see also Eq. (5.6) and Eq. (5.9)). Both  $\beta_1$  and  $\beta_2$  are independent of  $M$ , but do depend on the shaping network. Taking the derivative of Eq. (5.16) with respect to  $\bar{M}$ , treating  $J$  as a constant, results in:

$$\frac{d\sigma_A}{\sigma_A} = -\frac{\beta_1}{(\beta_1 + \beta_2 J \bar{M}^2)} \frac{d\bar{M}}{\bar{M}}. \quad (5.17)$$

A numerical estimation presented in Appendix C indicates that  $\beta_2 \ll \beta_1$ , and so for small  $M$ ,  $\beta_2 J \bar{M}^2 \ll \beta_1$ . In the latter regime, Eq. (5.17) thus reduces to  $d\sigma_A/\sigma_A = -d\bar{M}/\bar{M}$ , and a fractional increase  $d\bar{M}/\bar{M}$  results in a fractional decrease  $d\sigma_A/\sigma_A$  of the same magnitude. This explains the strong bias dependence of  $\sigma_A$  at lower  $\Delta V$ . At higher  $\Delta V$ , the term  $\beta_2 J \bar{M}^2$  becomes more dominant, decreasing the dependence of  $\sigma_A$  on  $M$ . At high  $\Delta V$ , an increase of  $J$  could in principle cause a degradation of the timing resolution, but this effect is not observed in the experiments.

The best timing resolution, measured with the 32-channel detector at  $\Delta V = +16$  V against the BaF<sub>2</sub>-PMT-detector, was 1.6 ns FWHM. The corresponding time spectrum is presented in Fig. 5.9. The best timing resolution obtained with the 64-channel detector was 2.0 ns. Neglecting the contribution of  $\sigma_P$ , the coincidence timing resolution of a pair of APD-detectors can be approximated as

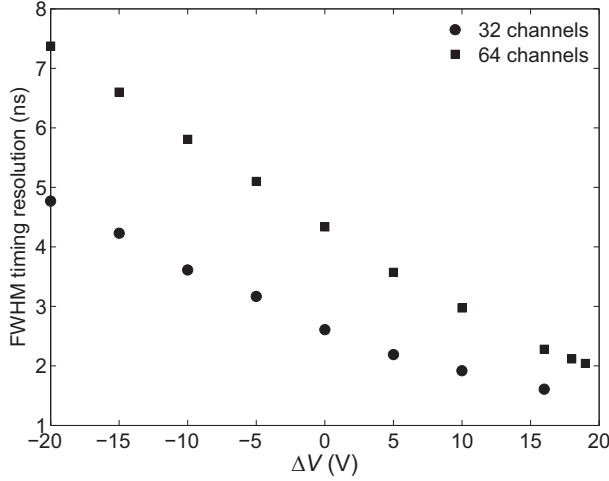


Figure 5.8: Timing resolution as a function of APD bias voltage, measured with crystals LYSO10-P2 (32 channels) and LYSO20-P2 (64 channels), using an TFA integration time constant of 2 ns. The error bars fall within the markers.

$\sigma'_A = \sqrt{2}\sigma_A$ . This yields  $\sim 2.3$  ns for a pair of coincident 32-channel detectors and  $\sim 2.8$  ns for a pair of 64-channel detectors.

### Energy resolution

A pulse height spectrum of crystal LYSO10-P2 at 511 keV and  $\Delta V = 0$  V ( $M \sim 50$ ) is presented in Fig. 5.10. The corresponding FWHM energy resolution is 10.8%. This value is close to the 9.7% measured with the LAAPD (see Fig. 5.6). Despite the considerable dead space between the pixels of the APD array of  $\sim 60\%$ , the total active APD area coupled to the crystal is  $81.92 \text{ mm}^2$ , while for the LAAPD this is  $100 \text{ mm}^2$ . This corresponds to a difference in active area of only 18%.

An overview of the energy resolutions and the different model contributions at the same bias voltage is listed in Table 5.4 for several crystals. The term describing the excess scintillation photon variance dominates the other terms.

A comparison between the calculated and measured energy resolutions as a function of the APD bias is presented in Fig. 5.11 for crystal LYSO10-P2. In contrast with the LAAPD results, it is observed that the calculated values underestimate the measurements, and that the model does not describe the experimentally observed deterioration of the energy resolution at high bias. Similar results

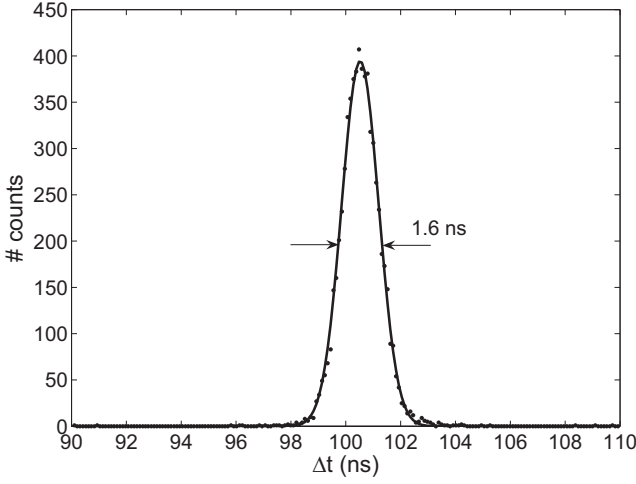


Figure 5.9: Timing spectrum of LYSO10-P2 at  $\Delta V = +16$  V and a TFA integration time constant of 2 ns. The solid line represents a Gaussian fit through the data.

Table 5.4: Overview of energy resolution contributions at  $\Delta V = 0$ .

Crystal	$\Delta E/E$ (%)	$\overline{N}_e$ ( $e^-$ )	$\frac{\alpha^2 - 1}{\overline{N}_{ph}}$	$\frac{J}{\overline{N}_e \overline{M}}$	$\frac{ENC^2}{\overline{N}_e^2}$
LYSO10-P1	11.0	370000	$1.82 \cdot 10^{-3}$	$2.55 \cdot 10^{-4}$	$0.99 \cdot 10^{-4}$
LYSO10-P2	10.8	411000	$1.50 \cdot 10^{-3}$	$2.30 \cdot 10^{-4}$	$0.80 \cdot 10^{-4}$
LYSO20-P1	11.9	304000	$1.57 \cdot 10^{-3}$	$3.11 \cdot 10^{-4}$	$2.92 \cdot 10^{-4}$
LYSO20-P2	11.0	374000	$1.25 \cdot 10^{-3}$	$2.53 \cdot 10^{-4}$	$1.93 \cdot 10^{-4}$

were obtained with crystal LYSO20-P2 coupled to two APD arrays. The observed differences may be caused by an increasing excess noise factor at increasing APD gain, an effect that was neglected in the model. However, a value of  $J$  of  $\sim 4$  would be needed to account for the difference at the highest bias if no other effects would play a role. This is a high value compared to measurements with these devices reported elsewhere [37].

Additional peak broadening may be caused by gain differences between the individual APD channels, which cause a dependence of the detector response on the position of interaction in the crystal. Using 5.89 keV X-rays from an  $^{55}\text{Fe}$ -source, these inter-channel gain differences were found to be bias dependent, increasing from a relative standard deviation of 3.4% at  $\Delta V = -40$  V to 4.9% at  $\Delta V = +10$  V. The influence of these gain differences was investigated with Monte Carlo simulations in Geant4 [100], by irradiating a  $20 \times 10 \times 10$  mm<sup>3</sup> Teflon-wrapped LYSO crystal coupled to one APD array with a beam of 511 keV photons. Approximately 100 events were recorded, optically tracking the scintillation photons and scoring the number incident on each APD pixel in each event. Taking into account an excess noise factor of 1.75 and an equivalent noise charge of 750 e<sup>-</sup> for each pixel, the energy resolution was determined in two situations. In the first, all APD pixels had the same gain, while in the second, the pixels were given the same relative gains as found with the  $^{55}\text{Fe}$ -measurements at  $\Delta V = +10$  V. All other parameters were kept the same for this comparison. The energy resolutions found were  $10.1 \pm 0.1\%$  with equal channel gains and  $10.2\% \pm 0.1\%$  with unequal channel gains. Thus, no significant peak broadening due to gain differences between the APD pixels was observed.

### Spatial resolution

Fig. 5.12 represents a histogram of positioning errors obtained with crystal LYSO10-P2 along the  $x$ -direction, containing data from all beam positions. The corresponding spatial resolution, obtained by linear interpolation of the histogram, was 1.64 mm FWHM and 4.42 mm FWTM, not corrected for the  $\sim 0.9$  mm FWHM measurement beam.

An analysis of the influence of the e-h pair yield on the spatial resolution is presented in Table 5.5. Slight improvements of the spatial resolution with increasing e-h pair yield are observed both between the two 10 mm crystals and between the two 20 mm crystals. However, it is noted that these improvements are comparable to the estimated measurement uncertainties of 0.05 mm for the FWHM and 0.2 mm for the FWTM, see Appendix B.

The influence of the equivalent noise charge on the spatial resolution was in-

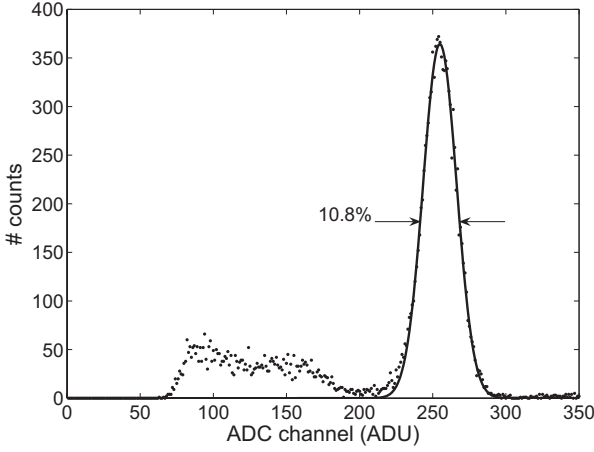


Figure 5.10: Pulse height spectrum at 511 keV,  $\Delta V = 0$  V and a shaping time of  $0.2 \mu\text{s}$  of crystal LYSO10-P2. The solid line represents a Gaussian fit through the data.

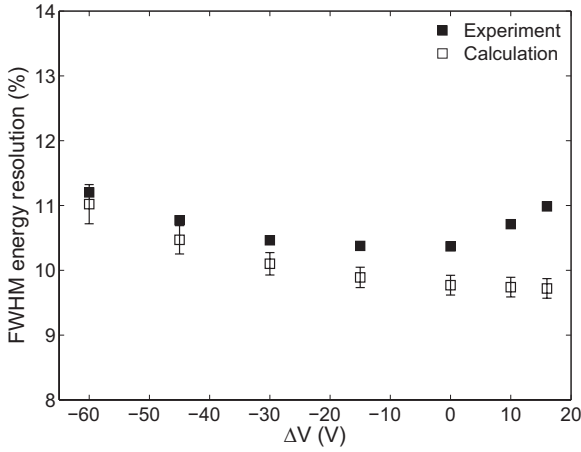


Figure 5.11: Measured and calculated energy resolution of LYSO10-P2 as a function of APD bias voltage at an amplifier shaping time of  $0.2 \mu\text{s}$ . The error bars indicate a  $1\sigma$  uncertainty. The error bars of the experimental data fall within the markers.

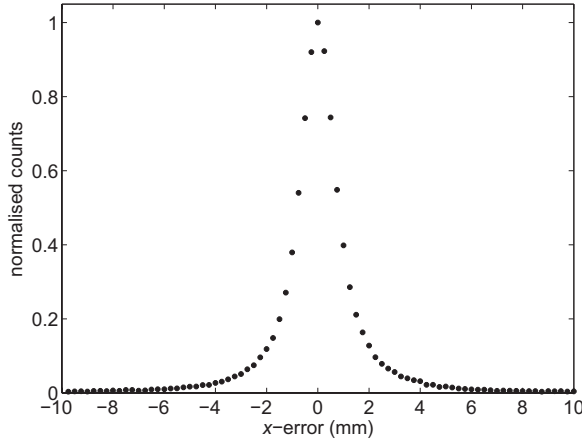


Figure 5.12: Positioning error histogram obtained with crystal LYSO10-P2 along the  $x$ -direction, containing data from all beam positions. The corresponding spatial resolution was 1.64 mm FWHM and 4.42 mm FWTM.

vestigated by adding random gaussian noise to the measured data sets by software. The amplitude of the added noise was equal for all channels. At each ENC value, a new reconstruction of the data was performed to estimate the spatial resolution. The results of this analysis are presented in Fig. 5.13. The 64-channel detectors (solid markers) are clearly more affected by the noise than the 32-channel detectors (open markers), in accordance with Eq. (5.14). Compared to a 32-channel detector, each pixel in a 64-channel detector receives approximately half the number of scintillation photons. Adding equal amounts of noise per channel therefore results in a poorer SNR per channel in the 64-channel case. Between the two 32-channel detectors, the crystal with the highest photon yield is least affected by the added noise (see Table 5.5); the same is observed between the two 64-channel detectors. Furthermore, it is noted that the spatial resolution clearly deteriorates even when only little noise is added. This is an indication that electronic noise forms a non-negligible contribution to the spatial resolution, in contrast to the energy resolution. Again, this is in accordance with Eq. (5.14). For example, for crystal LYSO20-P2 for which  $n = 64$ , the terms  $nJ/(\bar{N}_e/\bar{M})$  and  $n(ENC/\bar{N}_e)^2$  amount to  $1.62 \cdot 10^{-2}$  and  $1.24 \cdot 10^{-2}$ , respectively, while the scintillation photon term remains  $1.25 \cdot 10^{-3}$  (see also Table 5.4).

The spatial resolution as a function of the bias voltage measured with sample

Table 5.5: Global 1D spatial resolution and photo electron yield of the crystals investigated. The results are not corrected for the width of the measurement beam.

Sample	$\bar{N}_e/\bar{M}$ ( $e^-/511$ )	x-resolution (mm)		y-resolution (mm)	
		FWHM	FWTM	FWHM	FWTM
LYSO10-P1	6858	1.69	4.57	1.80	4.79
LYSO10-P2	7606	1.64	4.42	1.70	4.33
LYSO20-P1	5631	1.84	5.09	1.94	5.56
LYSO20-P2	6928	1.74	4.76	1.88	5.03

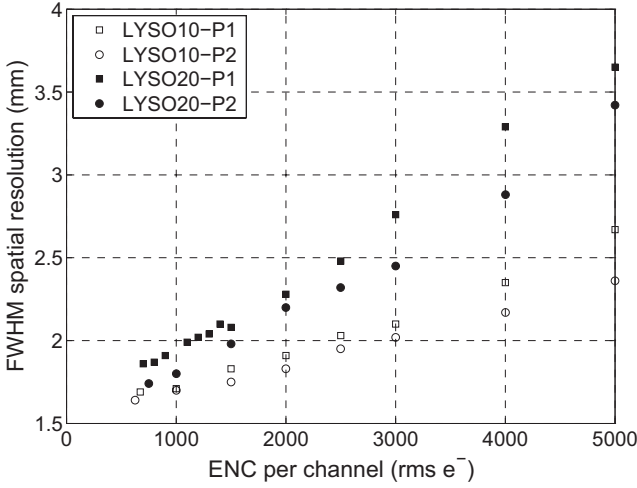


Figure 5.13: Global 1D x-spatial resolution of several crystals as a function of the equivalent noise charge per channel, at fixed  $\Delta V = 0$  V. The results include the influence of the  $\sim 0.9$  mm FWHM beam. The 10 mm (32 channel) detectors are represented by open markers, the 20 mm (64 channel) detectors by solid markers.



Table 5.6: Spatial resolution of LYSO20-P2 as a function of the APD bias voltage, not corrected for the width of the measurement beam.

$\Delta V$ (V)	$ENC/N_e$	x-resolution (mm)		y-resolution (mm)	
		FWHM	FWTM	FWHM	FWTM
-30	$3.2 \cdot 10^{-2}$	1.84	5.15	1.98	5.78
-15	$2.3 \cdot 10^{-2}$	1.78	4.85	1.86	4.99
0	$1.8 \cdot 10^{-2}$	1.74	4.76	1.88	5.03
+10	$1.4 \cdot 10^{-2}$	1.78	5.00	1.90	5.12
+16	$1.4 \cdot 10^{-2}$	1.80	5.17	1.91	5.19

LYSO20-P2 is shown in Table 5.6. In the second column, the total electronic noise term  $ENC/N_e$  is also indicated. Although this term is lowest at the highest bias, the optimum spatial resolution is not observed there, but around  $\Delta V = 0$  V. The observed deterioration at high bias may again be due to an increase of  $J$ , just as for the energy resolution (see Fig. 5.11).

All results presented here include the influence of the width of the experimental photon beam. In a PET system, this influence is not present. The beam had an estimated width of  $\sim 0.9$  mm FWHM, constituting a significant contribution to the results. However, correcting the results by deconvolution of the beam is not trivial, as it is divergent and has a non-Gaussian shape. A Monte-Carlo based procedure to do so will be discussed elsewhere [89]. It is estimated that with an infinitely narrow beam, the intrinsic detector spatial resolution of LYSO10-P2 at  $\Delta V = 0$  V is approximately 1.26 mm FWHM.

## 5.6 Conclusions

An analysis of the energy, timing and spatial resolutions of monolithic scintillator detectors was presented. Good agreement between a model of the energy resolution and experiments with a crystal coupled to a single pixel LAAPD was obtained. The energy resolutions observed with scintillators coupled to APD arrays were in the order of 10-11% FWHM, but discrepancies between model calculations and experiments of up to  $\sim 1.2\%$  FWHM were found at the highest APD gains. It was shown that the energy resolution is dominated by the variance in the number of scintillation photons produced per event, while the APD excess noise factor and electronic noise contributions are of less importance. For good timing and spatial resolutions, however, minimisation of the electronic noise is necessary, and should thus be taken into account for example in the design of a front-end ap-

plication specific integrated circuit (ASIC). Our model predicts that the excess noise factor also forms an important contribution to the spatial resolution, setting an important criterion for APDs in this application.

Spatial resolutions down to 1.64 mm were obtained. The results were not corrected for the influence of the  $\sim 0.9$  mm FWHM beam; it is estimated that an intrinsic detector spatial resolution of  $\sim 1.26$  mm FWHM may be achieved with an infinitely narrow beam.

Coincidence timing resolutions of less than 3 ns were shown to be feasible. The best timing performance was observed operating the APD at the highest possible bias voltage. Although the best energy and spatial resolutions were achieved at lower bias, the deterioration of these two quantities at higher bias was found to be small. It is therefore likely that the best performance of a scanner based on these detectors in terms of image spatial resolution and count rate performance will be found when operating the APD arrays close to the breakdown voltage.

## Chapter 6

# Model analysis of the detector point spread function<sup>1</sup>

### Abstract

It was demonstrated in Chapter 4 that monolithic scintillator PET detectors offer the advantages of high spatial resolution, excellent depth-of-interaction (DOI) correction, high detection efficiency, good energy resolution, and simplicity of design. This chapter presents an analysis of the point spread function (PSF) measured with a detector consisting of a  $20 \times 10 \times 20$  mm<sup>3</sup> LYSO:Ce<sup>3+</sup> crystal coupled to 2 Hamamatsu S8550SPL APD arrays. A simple model of the PSF is derived, which accounts for the spatial distribution of the energy deposited by the annihilation photons within the scintillator, as well as for the influences of statistical signal fluctuations and electronic noise. A detailed validation of the model is performed through comparison with measured detector PSFs. The model is shown to describe the measured PSFs well at the noise levels found in our experiments. It is furthermore demonstrated how the model can be used to quantify the influence of a finite-diameter test beam of annihilation photons on measured detector PSFs, and how a correction for this influence can be made.

---

<sup>1</sup>This chapter is to be published as M. C. Maas, D. R. Schaart, D. J. van der Laan, P. Bruyndonckx, C. Lemaître and C. W. E. van Eijk, “Model Analysis of the Point Spread Function of Monolithic Scintillator PET Detectors”, *to be submitted*.

## 6.1 Introduction

It was shown in Chapter 4 that monolithic scintillator detectors have favourable characteristics for application in positron emission tomography (PET). They offer the advantages of high spatial resolution, excellent depth-of-interaction (DOI) correction, high detection efficiency, good energy resolution, and simplicity of design.

The present chapter focuses on an analysis of the point spread function (PSF) of our monolithic scintillator detectors. To gain an understanding of the factors which determine the PSF, a simple model is derived that accounts for the spatial distribution of the energy depositions following the interaction of an annihilation photon within the scintillator, as well as for the influence of signal fluctuations arising from photon and charge carrier statistics and from electronic noise.

The use of the model is demonstrated by fitting it to the measured PSF of a prototype monolithic scintillator detector consisting of a  $\text{LYSO}:\text{Ce}^{3+}$  crystal and two APD arrays. The model is then used to quantify the effect of the finite diameter of the test beam of annihilation photons on the measured PSF, and it is shown how a correction for this influence can be made. Using the fitting and correction methods thus demonstrated, a detailed validation of the different components of the model is then performed.

## 6.2 Point spread function models

Upon estimating the entry points of a series of test events with the procedure described in Section 3.3.1, a normalised, two-dimensional (2D) histogram of the errors  $\Delta \mathbf{x}_j = (\hat{\mathbf{x}}_j - \mathbf{x}_t)$  can be created, where  $\hat{\mathbf{x}}_j$  is the estimated entry point of the  $j$ -th test event recorded at  $\mathbf{x}_t = (x_t, y_t)$ . This histogram approaches the point spread function  $PSF(x, y)$  at  $\mathbf{x}_t$  if the number of test events is sufficiently large, see Chapter 3.

### 6.2.1 Detector PSF

A model of  $PSF(x, y)$  is derived for perpendicularly incident annihilation photons, i.e. parallel to the  $z$ -axis (see Fig. 6.1). Four factors are assumed to contribute to the PSF: (1) the spatial distribution of energy depositions within the crystal, (2) photon and electron-hole (e-h) pair statistics and electronic noise in the measured data, (3) the position estimation algorithm and (4) a small background contribution due to e.g. scattering of the annihilation photons in materials in between the

source and the crystal. Each of these contributions is accounted for as described in the following.

An annihilation photon entering the crystal at some entry point coordinate  $\mathbf{x}_e \equiv (x_e, y_e)$  on the front surface of the crystal ( $z = 0$ ) may give rise to multiple energy depositions, e.g. due to X-rays and Auger electrons following photoelectric absorption, or secondary photons and electrons following Compton scattering. For each detected annihilation photon, we define the corresponding energy deposition centroid as the weighted average of these energy depositions. For the present purpose, only the  $x$ - and  $y$ -coordinates  $\mathbf{x}_c \equiv (x_c, y_c)$  of this energy deposition centroid are of interest. These are given by:

$$\mathbf{x}_c = \frac{\sum_n E_n \mathbf{x}_n}{\sum_n E_n}, \quad (6.1)$$

where  $E_n$  and  $x_n$  are the energy deposited in, and the  $x$ - and  $y$ -coordinates of, the  $n^{\text{th}}$  energy deposition, respectively.

We now define the function  $\gamma_0$  as the probability distribution of  $\mathbf{x}_c$  for a given entry point  $\mathbf{x}_e$ :

$$P(\mathbf{x}_c | \mathbf{x}_e) = \gamma_0(\mathbf{x}_c - \mathbf{x}_e). \quad (6.2)$$

This distribution is obtained by Monte Carlo simulation in this work (see Section 6.3.3).

The following two assumptions are now made. First, it is assumed that the distribution of scintillation light on the photosensor due to an event consisting of multiple energy depositions can be approximated by the light distribution due to a single deposition of the same total energy at the corresponding energy deposition centroid. Second, it is assumed that each centroid position corresponds with a unique expected normalised scintillation light distribution, and, in reverse, that each light distribution corresponds with a unique expected position of the energy deposition centroid.

The light distribution actually measured for a given event may differ from the expected distribution due to statistical signal fluctuations and electronic noise. We will denote the expectation values of the coordinates of the energy centroid corresponding with a measured light distribution as  $\mathbf{x}'_c \equiv (x'_c, y'_c)$ . We now describe the probability distribution of  $\mathbf{x}'_c$  corresponding to a given  $\mathbf{x}_c$  by a bivariate normal distribution  $N_{\Sigma}$  with zero mean and covariance matrix  $\Sigma$ :

$$P(\mathbf{x}'_c | \mathbf{x}_c) = N_{\Sigma}(\mathbf{x}_c - \mathbf{x}'_c) \equiv \frac{1}{2\pi|\Sigma|^{1/2}} \exp \left\{ -\frac{1}{2} (\mathbf{x}_c - \mathbf{x}'_c) \Sigma^{-1} (\mathbf{x}_c - \mathbf{x}'_c)^T \right\}, \quad (6.3)$$

where the off-diagonal elements of  $\Sigma$  are assumed to be equal to zero. This distribution is to be seen as a first-order approximation to an unknown underlying distribution, the theoretical determination of which is considered beyond the scope of this work.

The probability that the light distribution actually measured for a given photon entering at  $\mathbf{x}_e$  corresponds to  $\mathbf{x}'_c$  can now be written as:

$$\begin{aligned} P(\mathbf{x}'_c|\mathbf{x}_e) &= \sum_{x_c} \sum_{y_c} P(\mathbf{x}'_c|\mathbf{x}_c) P(\mathbf{x}_c|\mathbf{x}_e) = \sum_{x_c} \sum_{y_c} N_{\Sigma}(\mathbf{x}_c - \mathbf{x}'_c) \gamma_0(\mathbf{x}_c - \mathbf{x}_e) \\ &= \{\gamma_0 * N_{\Sigma}\}(\mathbf{x}'_c - \mathbf{x}_e), \end{aligned} \quad (6.4)$$

where the notation  $\{f * g\}(\mathbf{x})$  denotes the convolution of two functions  $f(\mathbf{x})$  and  $g(\mathbf{x})$ .

Based on the measured light distribution with corresponding  $\mathbf{x}'_c$ , the position estimation algorithm assigns an estimated entry point  $\hat{\mathbf{x}}_e$  from the discrete set of reference entry points  $\{\mathbf{x}_r\}$ , see Section 3.3.1. In the following derivation, it is assumed that an equal number of reference events  $n_{\text{ref}}$  is recorded at each entry point, so that the total number of events in the reference set equals:

$$N_{\text{ref}} = k \cdot n_{\text{ref}}, \quad (6.5)$$

where  $k$  is the total number of reference entry points.

Following the same arguments as above, a reference event recorded at  $\mathbf{x}_r$  has a probability of generating a light distribution corresponding to  $\mathbf{x}'_c$  of:

$$P(\mathbf{x}'_c|\mathbf{x}_r) = \{N_{\Sigma} * \gamma_0\}(\mathbf{x}'_c - \mathbf{x}_r). \quad (6.6)$$

If  $N_{\text{ref}} \rightarrow \infty$ , two situations can be distinguished for the selection of  $\hat{\mathbf{x}}_e$ : using 1 nearest neighbour ( $L = 1$ ), and using many nearest neighbours ( $L \rightarrow \infty$ ). For  $L = 1$  and  $N_{\text{ref}} \rightarrow \infty$ , the nearest neighbour algorithm behaves as a proportional estimator [68]. In this case, the probability  $P(\hat{\mathbf{x}}_e|\mathbf{x}'_c)$  of selecting entry point  $\hat{\mathbf{x}}_e$  is proportional to the local values of the various  $P(\mathbf{x}'_c|\mathbf{x}_r)$  evaluated at  $\mathbf{x}'_c$ . This probability can be approximated by:

$$P(\hat{\mathbf{x}}_e|\mathbf{x}'_c) = \{\gamma_0 * N_{\Sigma}\}(\hat{\mathbf{x}}_e - \mathbf{x}'_c) \quad \text{for } L = 1 \wedge N_{\text{ref}} \rightarrow \infty. \quad (6.7)$$

The probability distribution of estimated entry points  $\hat{\mathbf{x}}_e$  given a true entry point  $\mathbf{x}_e$  can be expressed for this case as:

$$\begin{aligned} P(\hat{\mathbf{x}}_e|\mathbf{x}_e) &= \sum_{x'_c} \sum_{y'_c} P(\hat{\mathbf{x}}_e|\mathbf{x}'_c) P(\mathbf{x}'_c|\mathbf{x}_e) \\ &= \{\gamma_0 * N_{\Sigma} * N_{\Sigma} * \gamma_0\}(\hat{\mathbf{x}}_e - \mathbf{x}_e) \quad \text{for } L = 1 \wedge N_{\text{ref}} \rightarrow \infty. \end{aligned} \quad (6.8)$$

For  $L \rightarrow \infty$  and  $N_{\text{ref}} \rightarrow \infty$  with  $L/N_{\text{ref}} \rightarrow 0$ , the nearest neighbour algorithm selects the reference entry point for which the probability density function  $P(\mathbf{x}'_c|\mathbf{x}_r)$  evaluated at  $\mathbf{x}'_c$  is greatest. Assuming that these functions are symmetrical and that the reference entry points lie on a regular, rectangular grid,  $P(\hat{\mathbf{x}}_e|\mathbf{x}'_c)$  follows a 2D uniform distribution covering a rectangular area centred around  $\mathbf{x}'_c$ :

$$\begin{aligned}
 P(\hat{\mathbf{x}}_e|\mathbf{x}'_c) &= \Upsilon(\hat{\mathbf{x}}_e|\mathbf{x}'_c) \\
 &\equiv U(x'_c - \frac{\Delta x_r}{2}, x'_c + \frac{\Delta x_r}{2}) \cdot U(y'_c - \frac{\Delta y_r}{2}, y'_c + \frac{\Delta y_r}{2}) \\
 &= \begin{cases} \frac{1}{\Delta x_r \Delta y_r} & \text{for } -\frac{\Delta x_r}{2} \leq \hat{x}_e - x'_c \leq \frac{\Delta x_r}{2} \text{ and } -\frac{\Delta y_r}{2} \leq \hat{y}_e - y'_c \leq \frac{\Delta y_r}{2} \\ 0 & \text{elsewhere} \end{cases} \\
 &\quad \text{for } L \rightarrow \infty \wedge N_{\text{ref}} \rightarrow \infty \wedge L/N_{\text{ref}} \rightarrow 0,
 \end{aligned} \tag{6.9}$$

where  $\Delta x_r$  and  $\Delta y_r$  represent the distances between adjacent reference entry points in the  $x$ - and  $y$ -directions, respectively. For this case the probability distribution of  $\hat{\mathbf{x}}_e$  given  $\mathbf{x}_e$  can be written:

$$\begin{aligned}
 P(\hat{\mathbf{x}}_e|\mathbf{x}_e) &= \sum_{x'_c} \sum_{y'_c} P(\hat{\mathbf{x}}_e|\mathbf{x}'_c) P(\mathbf{x}'_c|\mathbf{x}_e) \\
 &= \{\gamma_0 * N_{\Sigma} * \Upsilon\}(\hat{\mathbf{x}}_e - \mathbf{x}_e) \\
 &\quad \text{for } L \rightarrow \infty \wedge N_{\text{ref}} \rightarrow \infty \wedge L/N_{\text{ref}} \rightarrow 0.
 \end{aligned} \tag{6.10}$$

### 6.2.2 Influence of test beam diameter

The model presented thus far describes the distribution of estimated entry points  $\hat{\mathbf{x}}_e$  given a known entry point  $\mathbf{x}_e$ . However, as the beam of annihilation photons used to record the test and the reference data sets has a finite diameter, the true entry points are known in neither set. A measured PSF thus actually represents  $P(\hat{\mathbf{x}}_b|\mathbf{x}_b)$ , where  $\mathbf{x}_b \equiv (x_b, y_b)$  represents the true beam position and  $\hat{\mathbf{x}}_b$  the estimated one, defining the beam position as the location where the beam axis intersects the crystal front surface. The probability distribution of the  $x$ - and  $y$ -coordinates of the energy centroids due to a realistic experimental beam, having a finite diameter and possibly exhibiting divergence, can again be determined by Monte Carlo simulation and will be written as:

$$P(\mathbf{x}_c|\mathbf{x}_b) = \gamma_b(\mathbf{x}_c - \mathbf{x}_b), \tag{6.11}$$

where the subscript 'b' is used to indicate the use of a realistic beam. The probability distribution of  $\hat{\mathbf{x}}_b$ , given  $\mathbf{x}_b$ , is then found by substituting  $\gamma_b$  for  $\gamma_0$  in the

derivation given in the previous section, yielding:

$$P(\hat{\mathbf{x}}_b | \mathbf{x}_b) = \{\gamma_b * N_\Sigma * N_\Sigma * \gamma_b\}(\hat{\mathbf{x}}_b - \mathbf{x}_b) \quad \text{for } L = 1 \wedge N_{\text{ref}} \rightarrow \infty, \quad (6.12)$$

and

$$P(\hat{\mathbf{x}}_b | \mathbf{x}_b) = \{\gamma_b * N_\Sigma * \Upsilon\}(\hat{\mathbf{x}}_b - \mathbf{x}_b) \quad \text{for } L \rightarrow \infty \wedge N_{\text{ref}} \rightarrow \infty \wedge L/N_{\text{ref}} \rightarrow 0. \quad (6.13)$$

### 6.2.3 Background

To account for effects such as scattering of the annihilation photons on materials in between the source and the crystal (e.g. APD array on the crystal front surface or the entrance window of the detector box), a background contribution is included in the model. For each true beam position  $\mathbf{x}_b$ , the background is assumed to be uniformly distributed over all available reference coordinates:

$$b(\hat{\mathbf{x}}_b - \mathbf{x}_b) = c \cdot U(x_r^{\min} - x_b, x_r^{\max} - x_b) \cdot U(y_r^{\min} - y_b, y_r^{\max} - y_b), \quad (6.14)$$

where  $b$  is the background contribution at a single beam position,  $c$  is a constant, and  $x_r^{\min}$ ,  $x_r^{\max}$ ,  $y_r^{\min}$  and  $y_r^{\max}$  are the minimum and maximum  $x$ - and  $y$ -coordinates in the reference data, respectively.

Experimentally, the PSF is usually determined by summing the PSFs measured at multiple beam positions in order to improve statistics on the histogram. The model background contribution for this case is found by summing the individual contributions  $b(\hat{\mathbf{x}}_b - \mathbf{x}_b)$  over all  $\mathbf{x}_b$  in the test data:

$$B(\hat{\mathbf{x}}_b - \mathbf{x}_b) = c \cdot \sum_{x_b} \sum_{y_b} U(x_r^{\min} - x_b, x_r^{\max} - x_b) \cdot U(y_r^{\min} - y_b, y_r^{\max} - y_b), \quad (6.15)$$

where it is assumed that  $c$  is equal for all beam positions and that equal numbers of test events are used at each beam position. This expression is equivalent to a scaled convolution of two uniform distributions: one spanning the area containing the test coordinates, and one spanning the area containing the reference coordinates. Therefore,  $B(\hat{\mathbf{x}}_b - \mathbf{x}_b)$  generally has a trapezoidal shape.

### 6.2.4 PSF model summary

A summary of the model expressions for the different cases considered in the preceding sections is presented in Table 6.1. Each case is represented by a symbol  $\text{PSF}_{rt}$ , where the subscripts ‘ $r$ ’ and ‘ $t$ ’ represent the diameter of the beam used



Table 6.1: Summary of the different PSF models, for different numbers of nearest neighbours, with or without a finite beam diameter in reference and/or test data. In all models, it is assumed that  $N_{\text{ref}} \rightarrow \infty$ .

PSF	Beam		Number of nearest neighbours	
	Reference	Test	$L = 1$	$L \rightarrow \infty \wedge L/N_{\text{ref}} \rightarrow 0$
PSF <sub>00</sub>	No	No	$\{\gamma_{0,r} * N_{\Sigma,r} * N_{\Sigma,t} * \gamma_{0,t}\} + B$	$\{N_{\Sigma,t} * \gamma_{0,t}\} + B$
PSF <sub>b0</sub>	Yes	No	$\{\gamma_{b,r} * N_{\Sigma,r} * N_{\Sigma,t} * \gamma_{0,t}\} + B$	$\{N_{\Sigma,t} * \gamma_{0,t}\} + B$
PSF <sub>0b</sub>	No	Yes	$\{\gamma_{0,r} * N_{\Sigma,r} * N_{\Sigma,t} * \gamma_{b,t}\} + B$	$\{N_{\Sigma,t} * \gamma_{b,t}\} + B$
PSF <sub>bb</sub>	Yes	Yes	$\{\gamma_{b,r} * N_{\Sigma,r} * N_{\Sigma,t} * \gamma_{b,t}\} + B$	$\{N_{\Sigma,t} * \gamma_{b,t}\} + B$

in the reference data and the test data, respectively. Specifically,  $r$  and  $t$  each take a value of either ‘0’ or ‘b’, corresponding either to a zero-diameter beam or to a beam with finite diameter and divergence, respectively. Analogously, the distributions  $\gamma_0$ ,  $\gamma_b$  and  $N_{\Sigma}$  have an extra subscript ‘r’ or ‘t’, specifying whether they pertain to the reference data or the test data, respectively. This distinction will be used in the validation of the model presented in Section 6.4.3. The extra subscript is omitted whenever this distinction is not necessary, i.e. in experiments performed using beams of equal diameter for measuring the reference and test data and with equal signal-to-noise ratios in both data sets. Most of our experiments are carried out in this latter way.

The uniform distribution  $\Upsilon$  describing the influence of the finite distances between adjacent reference entry points is approximated by a delta function in view of its narrow width compared to the width of the measured PSFs, and is omitted from the convolution.

## 6.3 Materials and methods

### 6.3.1 Detector

The detector module investigated here consists of a monolithic polished rectangular  $20 \times 10 \times 20 \text{ mm}^3$  LYSO:Ce<sup>3</sup> scintillation crystal coupled to two Hamamatsu S8550SPL APD arrays, see Fig. 6.1. The properties of the crystal are summarised in Table 6.2. The crystal is wrapped in Teflon tape on all sides not coupled to an APD array.

Table 6.2: Properties of the crystal investigated.

Sample	LYSO20-P2
Material	LYSO:Ce <sup>3+</sup>
Surface	polished
Dimensions	20×10×20 mm <sup>3</sup>
Light yield <sup>1</sup>	20.2·10 <sup>3</sup> ph/MeV
$\Delta E/E$ <sup>1</sup>	10.5% FWHM at 511 keV

<sup>1</sup> Data from Chapter 4

### 6.3.2 PSF measurements

The PSF was evaluated for one half of the symmetric crystal only in order to reduce measurement times. Reference data were recorded using the test setup described in Chapter 3, at a rectangular grid of beam positions covering the area  $(-10 \leq x \leq 10, -2 \leq y \leq 5)$  mm, in steps of 0.25 mm (see Fig. 6.1). Test data were drawn from the same data set (leave-one-out approach, see Section 3.3.1), covering the area  $(-3 \leq x \leq 3, 0 \leq y \leq 1.5)$  mm. The margin between the two sets at  $-2 \leq y \leq 0$  mm was used to avoid truncating the PSFs at  $y = 0$ . At each beam position,  $n_{\text{ref}} = 500$  reference events were recorded.

The entry point of each event in the test data set was estimated using the nearest neighbour procedure described in Section 3.3. Calculation of the PSF was optimised by finding the value of  $L$ . Each PSF was calculated using the value of  $L$  that minimised  $\langle \sigma_{\text{PSF}}^* \rangle \equiv 1/2 (\sigma_{\text{PSF},x}^* + \sigma_{\text{PSF},y}^*)$ , the average of the sample standard deviations of the histogram in the  $x$ - and  $y$ - directions. The asterisk is used to indicate that PSF values below 1% of the peak amplitude are disregarded in order to reduce the effect of outliers.

The influence of various parameters (such as the beam diameter) was studied by varying the parameter of interest in a series of measurements performed in 1 dimension (1D) only, in order to reduce measurement times. In these studies,  $n_{\text{ref}} = 1500$  reference events were recorded per beam position in the range  $-10 \leq x \leq 10$  mm along the  $x$ -axis ( $y = 0$ ), in steps of 0.25 mm. Test data were recorded in the range  $-3 \leq x \leq 3$  mm ( $y = 0$ ). For optimisation of  $L$  in 1D, the standard deviation  $\sigma_{\text{PSF}}^*$  of the measured 1D-PSF was minimised, again excluding bins lower than 1% of the peak amplitude.

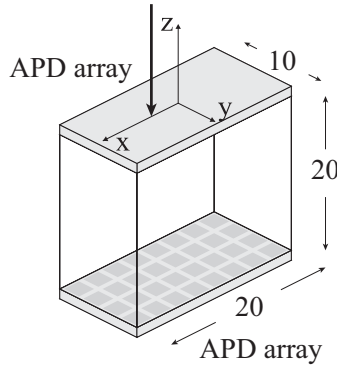


Figure 6.1: Schematic representation of the detector geometry investigated: a 20 mm thick LYSO:Ce<sup>3+</sup> crystal read out by 2 position-sensitive, Hamamatsu S8550SPL APD arrays. Dimensions are in indicated in mm.

### 6.3.3 Simulation of photon beam and intra-crystal scattering

To determine the energy centroid distributions due to a pencil beam,  $\gamma_0$ , and due to a realistic beam,  $\gamma_b$ , the experimental setup was modelled in a Monte Carlo simulation, see Fig. 6.2.

The  $^{22}\text{Na}$ -source was simulated using GATE, a Monte Carlo simulation toolkit [101]. The activity was assumed to be uniformly distributed within the ion exchange bead, which was modelled as a  $\varnothing 0.5 \times 1 \text{ mm}^3$  cylinder with a density of  $1 \text{ g/cm}^3$  and was contained in a  $\varnothing 25.4 \times 6.4 \text{ mm}^3$  polymethyl methacrylate (PMMA) cylinder. Approximately  $9 \cdot 10^5$  positrons were generated and tracked until annihilation, and the coordinates of the annihilation positions were stored.

A simulation of  $2 \cdot 10^5$  pairs of 511 keV photons was then performed in Geant4 [100]. For each photon pair, a point on the BGO crystal falling within the collimator opening was randomly picked from a uniform distribution. The vector connecting this point to a randomly picked annihilation position from the set determined previously was then calculated. It was thus implicitly assumed that no 511 keV photons could reach the BGO-PMT detector through the lead of the collimator. Photon acollinearity was accounted for by adding a randomly picked angle to this vector at the annihilation position, according to a distribution determined experimentally for PMMA [11]. A 511 keV photon was propagated along the resulting vector towards the APD detector, and upon interaction with the crystal, the coordinates of the energy deposition centroid were stored, taking a threshold of 100 keV

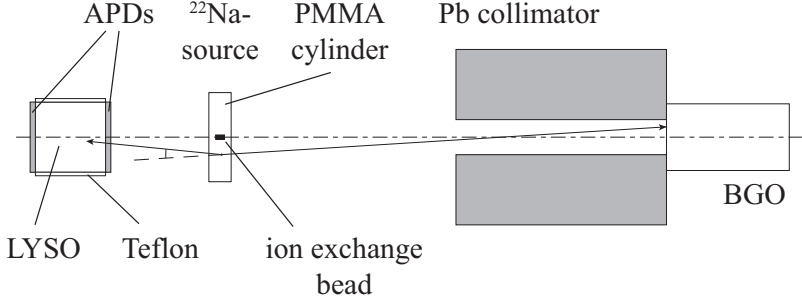


Figure 6.2: Geometry used in the 511 keV photon beam simulations (not to scale).

for the total energy deposition into account. The Teflon layer around the crystal was modeled as a 1 mm thick plastic layer (density  $0.9 \text{ g/cm}^3$ ).

The distributions  $\gamma_0$  and  $\gamma_b$  were obtained by creating histograms of the  $x$ - and  $y$ -coordinates of the energy deposition centroids within the crystal. The coordinates at which the 511 keV photons crossed the front surface of the crystal were also histogrammed, providing an estimate of the beam diameter  $d_b$ .

### 6.3.4 Fitting procedure

Fitting the model to measured PSFs was done by minimising the sum-of-squares (SSQ) difference between the appropriate model from Table 6.1 and the experimental result. The simulated distributions  $\gamma_0$  and/or  $\gamma_b$  were used as fixed inputs, while the amplitude and covariance matrix of  $N_\Sigma$  and the amplitude of  $B$  were used as fit parameters.

## 6.4 Results

In the following, we first fit the model derived in Section 6.2 to the measured detector PSF. the model is then used to quantify the influence of the test beam diameter on the measured detector PSF in Section 6.4.2, and it is shown how a correction for this influence can be made. Using the fitting and correction methods thus demonstrated, a detailed validation of the different model components is performed in Section 6.4.3.

Table 6.3: FWHM and FWTM of cross-sections through measured and corrected PSFs of the detector, obtained with  $L = 500$ .

	$PSF(x)$		$PSF(y)$	
	FWHM	FWTM	FWHM	FWTM
Measured	1.54	3.33	1.61	3.80
Corrected	1.05	2.09	1.25	2.42

### 6.4.1 Detector PSF

All measured detector PSFs have been determined using reference and test data sets recorded with a test beam of finite diameter  $\gamma_b$ . Hence, they are of type ‘ $PSF_{bb}$ ’ as defined in Table 6.1.

The cross-section  $PSF_{bb}(x)$  of the measured point spread function ( $L = 500$ ) in the  $x$ -direction at zero  $y$ -error is shown in Fig. 6.3a. The model of  $PSF_{bb}(x, y)$  for the case  $L \rightarrow \infty \wedge L/N_{\text{ref}} \rightarrow 0$  was then fitted to the measured data. The result is indicated by the solid curve. Excellent correspondence between the model and the experiment is observed. Similarly good correspondence was observed in the  $y$ -direction, i.e. for  $PSF_{bb}(y)$ .

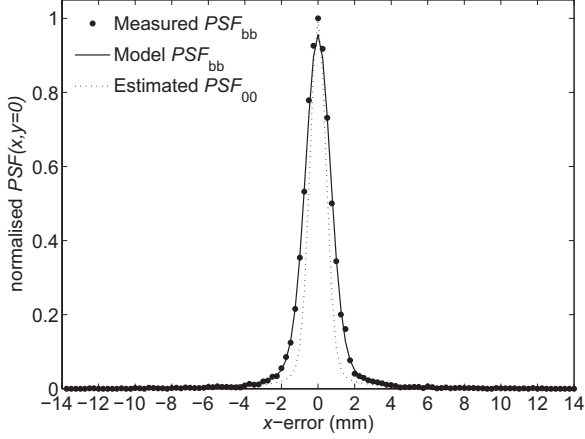
### 6.4.2 Influence of test beam diameter

Assuming that the model accurately describes the various contributions to the measured  $PSF_{bb}$ , it can be used to quantify the influence of the test beam diameter and, therefore, to make a correction for this influence. Here we show how this is done for the case  $L \rightarrow \infty \wedge L/N_{\text{ref}} \rightarrow 0$ .

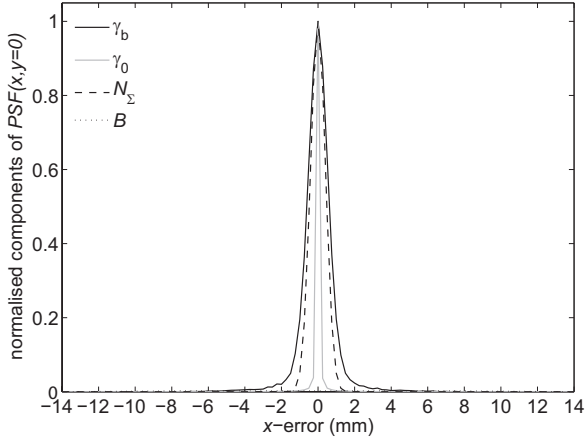
First, the distributions  $N_\Sigma$  and  $B$  are determined by fitting the appropriate model expression from Table 6.1 to the measured  $PSF_{bb}$ , using a Monte Carlo simulation of the test beam for determining  $\gamma_b$  (see Section 6.3.3). Subsequently,  $PSF_{00}$  is estimated by convolving the resulting  $N_\Sigma$  with  $\gamma_0$ , and adding  $B$ . Here,  $\gamma_0$  is determined from a Monte Carlo simulation of a beam with zero diameter. The result of this procedure is denoted by  $\widehat{PSF}_{00}$ .

The dotted curve in Fig. 6.3a shows  $\widehat{PSF}_{00}(x)$  for the case  $L = 500$ . Fig. 6.3b shows the corresponding cross-sections through  $\gamma_b$  (solid black curve),  $\gamma_0$  (solid grey curve),  $N_\Sigma$  (dashed curve), and  $B$  (dotted curve), where the amplitude of  $B$  has been scaled according to the amplitude of  $\{\gamma_b * N_\Sigma\}$ .

The FWHM and FWTM of the measured and intrinsic PSFs of this detector are listed in Table 6.3. A very good detector spatial resolution of 1.05 mm FWHM is found in the  $x$ -direction.



(a)



(b)

Figure 6.3: (a): Cross-sections at  $y = 0$  through the measured (circles), fitted (solid curve) and corrected (dotted curve)  $PSF(x,y)$  obtained with  $L = 500$ . (b): corresponding distributions  $\gamma_b$  (solid black curve),  $\gamma_0$  (solid grey curve),  $N_\Sigma$  (dashed curve) and  $B$  (dotted curve).

### 6.4.3 Model validation

In Section 6.4.1 it was demonstrated that the PSF model derived in Section 6.2 can accurately be fitted to measured detector PSFs. In Section 6.4.2 it was shown how the model can be used to quantify the influence of the test beam diameter and to correct the measured PSF for this influence. Using the methods demonstrated in those sections, we will further investigate the validity of the model in the following.

Two assumptions were made in the derivation of the model in Section 6.2.1 that are not trivial. First, it was assumed that the influence on the measured  $PSF_{bb}$  of the spatial distribution of the energy deposited within the crystal by the test beam can be accounted for by the distribution  $\gamma_b$  of the energy deposition centroids of each of the recorded events. Second, it was assumed that the influence of statistical fluctuations and electronic noise in the measured light distributions can be accounted for by a Gaussian distribution  $N_{\Sigma}$ .

The validity of the first assumption is investigated by separately studying the influence of the beam diameters  $d_{b,r}$  and  $d_{b,t}$  in the reference data (Section 6.4.3) and in the test data (Section 6.4.3), respectively. The second assumption is tested by varying the signal-to-noise ratio of the detector signals (Section 6.4.4).

For efficiency, all of these experiments were done by means of 1D resolution measurements. This implies that each of the distributions  $\gamma_b$ ,  $\gamma_0$  and  $B$  in Table 6.1 reduce to 1D functions; only the  $x$ -coordinate is taken into account. Instead of  $N_{\Sigma}$  we therefore use a 1D Gaussian distribution  $N_{\sigma}$  with standard deviation  $\sigma$ . The resulting point spread functions are denoted by ‘1D- $PSF_{bb}$ ’, etc.

#### Influence of $d_b$ in the reference data

The model predicts that while  $PSF_{bb}$  depends on the beam diameter  $d_{b,r}$  in the reference data for  $L = 1$ , this is no longer the case for  $L = 500$ , provided that  $L/N_{ref} \rightarrow 0$ , see Table 6.1. This was verified by recording a number of reference data sets at different values of  $d_{b,r}$  ranging from 0.84 mm FWHM to 1.46 mm FWHM. Specifically, the distance between the  $^{22}\text{Na}$ -source and the detector was varied, keeping the distance between the source and the PMT constant to maintain a constant beam profile. 1D- $PSF_{bb}$  was then calculated for each of these reference sets, using the same test set recorded at  $d_{b,t} = 0.84$  mm FWHM in all cases.

Fig. 6.4 shows the FWHM of 1D- $PSF_{bb}$  as a function of  $d_{b,r}$  for several values of  $L$ . In agreement with the model, the variation of 1D- $PSF_{bb}$  between  $d_{b,r} = 0.84$  mm FWHM and  $d_{b,r} = 1.46$  mm FWHM decreases from  $\sim 20\%$  at  $L = 1$  to  $\sim 6\%$  at  $L = 500$ .

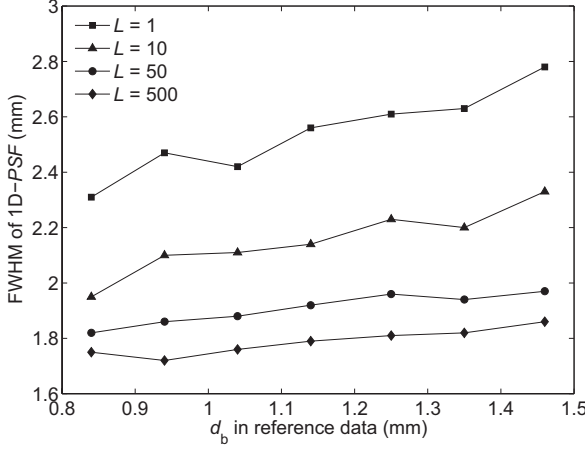


Figure 6.4: FWHM of measured 1D- $PSF$ s as a function of the beam diameter in the reference data  $d_{b,r}$ , for various values of  $L$ . Each 1D- $PSF$  was created using the same test data set, recorded at  $d_{b,t} = 0.84$  mm.

The slight dependence on  $d_{b,r}$  that remains at  $L = 500$  is attributed to the finite number of reference events per beam position  $n_{\text{ref}}$  ( $\sim 1500$  in these experiments). If the number of reference events recorded at the reference position  $\mathbf{x}_r$  closest to the  $\mathbf{x}'_c$  corresponding to the measured light distribution is not large compared to  $L$ , some of the nearest neighbours may be selected from other reference positions. In that case the probability  $P(\hat{\mathbf{x}}_e | \mathbf{x}'_c)$  that the positioning algorithm assigns a coordinate  $\hat{\mathbf{x}}_e$ , given the measured  $\mathbf{x}'_c$ , may no longer be given by Eq. (6.9), resulting in an increasing width of  $PSF_{bb}$ . We thus conclude that, while the condition  $L/N_{\text{ref}} \rightarrow 0$  may not be met entirely at  $L = 500$ , the data in Fig. 6.4 support the validity of our model. In addition, these results show that although  $\widehat{PSF}_{00}$  is a good approximation of the true  $PSF_{00}$ , the influence of  $\gamma_{b,r}$  is not entirely removed by the correction procedure, and a further improvement of the detector spatial resolution may be expected with increasing  $n_{\text{ref}}$  and/or decreasing  $d_{b,r}$ .

### Influence of $d_b$ in the test data

If the influence of the spatial distribution of the energy depositions on  $PSF_{bb}$  is accounted for correctly by  $\gamma_b$ ,  $\widehat{PSF}_{00}$  should be independent of the diameter of the test beam. This was tested by measuring 1D- $PSF_{bb}$  for various beam diameters  $d_{b,t}$  in the test data ( $0.84 \text{ mm} \leq d_{b,t} \leq 1.46 \text{ mm}$  FWHM) and correcting the re-



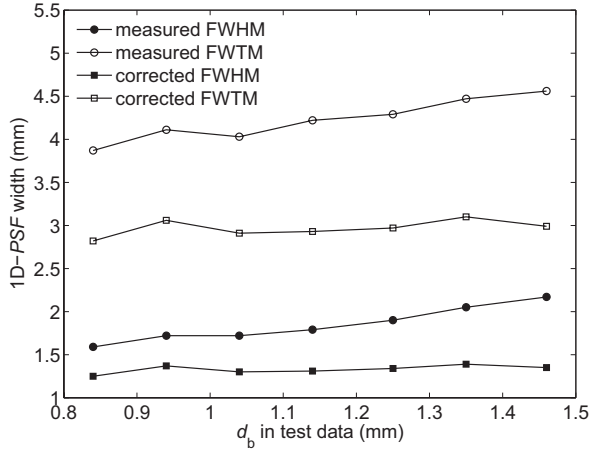


Figure 6.5: FWHM and FWTM of the measured  $1D-PSF_{bb}$  and corrected  $1D-\widehat{PSF}_{00}$  as a function of the beam diameter  $d_{b,t}$  in the test data. All PSFs were obtained using the same reference data set recorded at  $d_{b,r} = 0.84$  mm FWHM, using  $n_{ref} = 1500$  and the value of  $L$  that minimised  $\sigma_{PSF}^*$ .

sults using the simulated distribution  $\gamma_{b,t}$  appropriate for each beam diameter. The same reference data set recorded at  $d_{b,r} = 0.84$  mm FWHM was used for each measurement, keeping the influence of the beam diameter in the reference data the same in each experiment. Each  $1D-PSF_{bb}$  was calculated using the value of  $L$  that minimised  $\sigma_{PSF}^*$ , in order to match the condition  $L \rightarrow \infty \wedge L/N_{ref} \rightarrow 0$  as closely as possible.

Fig. 6.5 shows the FWHMs (solid symbols) and FWTMs (open symbols) of the measured  $1D-PSF_{bb}$  (circles) and the corrected  $1D-\widehat{PSF}_{00}$  (squares) as a function of  $d_{b,t}$ . Whereas the FWHM and the FWTM of the measured  $1D-PSF_{bb}$  increase with increasing  $d_{b,t}$ , the corrected  $1D-\widehat{PSF}_{00}$  appears to be essentially independent of the beam diameter in the test data. This suggests that the proposed procedure to correct for the influence of the spatial distribution of the energy deposited by the annihilation photons is indeed valid.

#### 6.4.4 Signal to noise ratio

In the model, it is assumed that the influence on the PSF of statistical fluctuations and electronic noise in the measured light distributions can be accounted for by a Gaussian distribution  $N_{\Sigma}$  (see Section 6.2.1). To investigate the validity of this

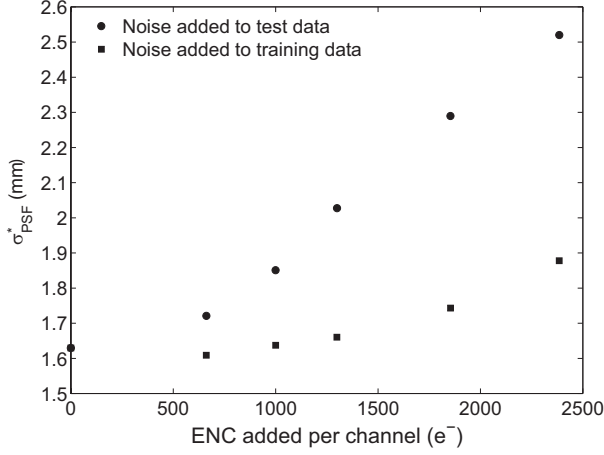
assumption, the influence on  $1D\text{-}PSF_{bb}$  of increasing noise levels in the reference data and the test data was studied. This was done by adding Gaussian noise to the measured light distributions by software, on top of the  $\sim 750\text{ e}^-$  equivalent noise charge (ENC) already present per channel at the APD array outputs [102], see Chapter 5. Two types of experiment were performed: noise was added to the test data only, leaving the reference data unaltered, and vice versa. For the case  $L \rightarrow \infty$ , adding noise to test data is expected to increase the width of  $1D\text{-}PSF_{bb}$ , while adding noise to the reference data should have negligible influence, provided that  $L/N_{\text{ref}} \rightarrow 0$ .

Fig. 6.6a shows the standard deviation  $\sigma_{\text{PSF}}^*$  of  $1D\text{-}PSF_{bb}$  for the case  $L \rightarrow \infty$  as a function of the ENC added to the test data (circles) and to the reference data (squares). As in the previous sections, each  $1D\text{-}PSF_{bb}$  was calculated using the value of  $L$  that minimised  $\sigma_{\text{PSF}}^*$ . As expected,  $\sigma_{\text{PSF}}^*$  increases rapidly when noise is added to the test data. If up to about  $\sim 1250\text{ e}^-$  ENC per channel is added to the reference data,  $\sigma_{\text{PSF}}^*$  can be seen to remain essentially constant. However, if more noise is added,  $\sigma_{\text{PSF}}^*$  starts to increase significantly. Similarly to in Section 6.4.3, this is probably due to the finite number of available reference events  $N_{\text{ref}}$ : as the value of  $L$  that minimises  $\sigma_{\text{PSF}}^*$  increases to compensate for the added noise, it increasingly deviates from the requirement  $L/N_{\text{ref}} \rightarrow 0$ .

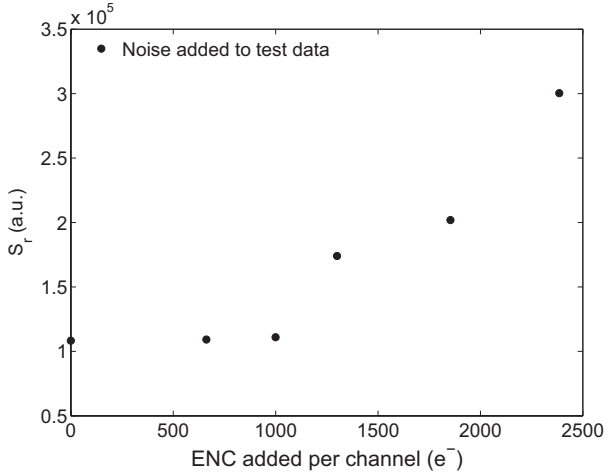
To investigate whether the influence of statistical fluctuations and noise is accurately accounted for by the Gaussian distribution  $N_{\Sigma}$  in the model, the residual sum of squares  $S_r \equiv \sum_i (PSF_{bb,\text{fit}}(x_i) - PSF_{bb,\text{exp}}(x_i))^2$  was calculated as a function of the amount of noise added to the test data. Here,  $PSF_{bb,\text{exp}}$  and  $PSF_{bb,\text{fit}}$  represent the measured and fitted PSF, respectively. The results of this analysis are shown in Fig. 6.6b. Below  $\sim 500\text{ e}^-$  ENC added per channel,  $S_r$  does not yet increase strongly with increasing noise. At higher noise levels, however,  $S_r$  starts to increase more rapidly. This suggests that  $N_{\Sigma}$  can indeed be approximated by a Gaussian distribution at the relatively low noise levels found in our measurements, but that this simple approximation loses its applicability if the noise level is increased too much.

### 6.4.5 Discussion

Although the Gaussian distribution  $N_{\Sigma}$  modelling the influence of statistical variances and electronic noise in the measured light distributions only represents a first-order approximation to an unknown underlying distribution, it was shown that this approximation yields good correspondence between measured and modelled PSFs at sufficiently high signal-to-noise ratios. This distribution can therefore be used to study the PSF as a function of instrumental parameters such as the



(a)



(b)

Figure 6.6: (a): Standard deviation  $\sigma_{\text{PSF}}^*$  of measured  $1D\text{-}PSF_{\text{bb}}$  as a function of the added equivalent noise charge in the test data (circles) and the reference data (squares). (b): Residual sum of squares  $S_r$  corresponding to these fits as a function of the added equivalent noise charge in the test data (circles). At each data point, the value of  $L$  that minimised  $\sigma_{\text{PSF}}^*$  for that particular noise level was used.

scintillator light yield, the geometry of the detectors and its light sensors, and the noise properties of the light sensors and front-end electronics.

This can be accomplished using a model describing the signal variances in the scintillator – light sensor – amplifier chain, as has been previously reported for our detectors [102], see Chapter 5. A statistical model of the signals resulting from scintillation events within the crystal can then be created using Monte Carlo simulations of the transport of optical photons in the detectors, taking all of the relevant instrumental parameters into account. This statistical model can then be used to derive the Cramér-Rao (C.R.) lower bound on the positioning variance as a function of the parameters of interest. Such an analysis is presented elsewhere for our detectors [90]. It is shown there that our measured PSFs indeed approach the C.R. lower bound for large sets of reference data, thus providing a useful tool for the optimisation of our detector design.

## 6.5 Conclusions

In this chapter, a simple model of the point spread function of monolithic scintillator detectors was derived, which accounts for the spatial distribution of the energy depositions following the interaction of annihilation photons within the scintillator, as well as for the influence of signal fluctuations arising from photon and charge carrier statistics and from electronic noise. The model was used to analyse the measured PSF of a prototype monolithic scintillator detector consisting of a  $\text{LYSO}:\text{Ce}^{3+}$  crystal and two APD arrays. The effect of the finite diameter of the test beam of annihilation photons used in our experiments on the measured detector PSF was quantified, and it was demonstrated how a correction for this influence can be made.

The results show that the proposed model describes the measured detector PSF well, within certain boundary conditions. Specifically, the model is based on the assumption that  $N_{\text{ref}} \rightarrow \infty$ . The model then predicts that the best possible spatial resolution is achieved if  $L \rightarrow \infty$  with  $L/N_{\text{ref}} \rightarrow 0$ . The extent to which these conditions are approximated by the finite values of  $L$  and  $N_{\text{ref}}$  used in practice depends not only on the values of  $L$  and  $N_{\text{ref}}$  themselves, but also on the beam diameter  $d_b$  and on the signal-to-noise ratio of the measured light distributions. Furthermore, the extent to which the influence of the signal-to noise ratio on the measured point spread function is accurately represented by a simple Gaussian distribution  $N_{\Sigma}$  was found to depend on the signal-to-noise ratio as well. It was shown that this approximation is valid at the signal-to-noise ratios found in our experiments.

We thus conclude that the proposed model is an accurate and useful tool for analysing the detector PSF of monolithic scintillator detectors and for correcting measured PSFs of such detectors for the influence of the finite diameter of the test beam of annihilation photons used in spatial resolution measurements.



## Chapter 7

# Simulated performance of small-animal PET scanners based on monolithic scintillator detectors

### Abstract

This chapter presents a pilot study of the performance of small-animal PET systems based on monolithic scintillator detectors. The study is based on Monte Carlo simulations which use measurements of the PSFs and other detector properties as input. Simulations are performed of scanners consisting of 1 or 4 rings with an inner diameter of 123.8 mm and an axial extent of 19.5 mm, each containing 32 detectors of 20 mm thick LSO.

The system resolution of the 1-ring scanner is estimated in 2D, both for ideal mathematical point sources without positron range or photon acollinearity, and for realistic  $\varnothing 0.5$  mm  $^{18}\text{F}$  sources. Very little degradation of the system resolution towards the edge of the field of view of the scanner is observed in either case. A 2D image of a simulated  $^{18}\text{F}$ -filled micro-Derenzo hot rod phantom reconstructed with an OSEM algorithm shows that rods with a diameter of 2.4 mm are well resolved.

The sensitivity for coincident detection at low count rates is estimated at 21% at the centre of the FOV of a 4-ring scanner with trapezoidally shaped detectors. This is substantially higher than the 3–4% reported for current state of the art systems. The NECR calculated for this system reaches 2000 kcps in a  $\varnothing 36 \times 67$  mm<sup>3</sup> water

phantom uniformly filled with  $^{18}\text{F}$  at an activity of 70 MBq.

Further improvement of the image quality is expected with an optimisation of the reconstruction algorithm and the detector geometry.

## 7.1 Introduction

The performance of monolithic scintillator detectors has been summarised in Chapter 4. The results were promising: a corrected detector spatial resolution of  $\sim 1.05$  mm FWHM was found, comparable to current state-of-the-art small animal PET systems, and the correction for the depth-of-interaction of incident 511 keV photons was found to be excellent. The energy and timing resolutions measured with these detectors are suitable for application in PET. In addition, the detectors have a high detection efficiency and compact design, suggesting that a PET scanner based on these detectors could have excellent performance characteristics.

This chapter presents a pilot study into the performance potential of small-animal PET scanners based on monolithic scintillator detectors, in terms of the image spatial resolution, the scanner sensitivity and the count rate performance. This is done by Monte Carlo simulations using experimental point spread functions (PSFs) and other performance parameters measured on a prototype detector module as input.

The image spatial resolution obtainable with these scanners is investigated in 2D acquisition mode. This is done by simulating a PET system consisting of 1 ring with an inner diameter of 123.8 mm containing 32 trapezoidally shaped detectors. The intrinsic system resolution of this system is analysed by simulating mathematical point sources emitting back-to-back annihilation photons at a range of radial distances from the scanner axis, neglecting positron range and photon acollinearity. The system resolution in response to realistic point sources is also investigated, by simulating eight  $\varnothing 0.5 \times 1 \text{ mm}^3$   $^{18}\text{F}$ -sources at various radial distances from the scanner axis, taking positron range and photon acollinearity into account. Finally, the image resolution obtained with a Micro-Derenzo hot rod phantom filled with  $^{18}\text{F}$  is analysed.

The scanner sensitivity and noise equivalent count rate (NECR) are analysed for scanners consisting of four rings of detectors. A comparison is made between trapezoidal monolithic detector modules, rectangular monolithic detector modules, and detector modules consisting of  $8 \times 4$  matrices of  $2 \times 2 \times 20 \text{ mm}^3$  crystals. The scanner sensitivity is investigated as a function of the axial and the radial the distance from the scanner centre using a 1 MBq mathematical point source emitting back-to-back 511 keV photons. The NECR is determined using



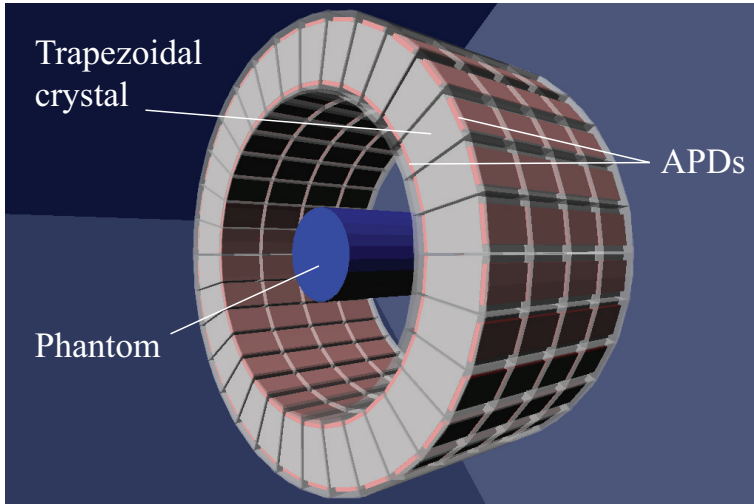


Figure 7.1: Four-ring scanner with trapezoidal detectors.

simulations of a mouse phantom and a rat phantom, modelled respectively as a  $\varnothing 36 \times 67 \text{ mm}^3$  and a  $\varnothing 60 \times 150 \text{ mm}^3$  water cylinder filled with uniform  $^{18}\text{F}$  activity.

## 7.2 Methods

### 7.2.1 Monte Carlo simulations

Simulations were performed using the Monte Carlo simulation toolkit GATE [101]. The simulated scanners consisted of one or four rings of 32 detector modules each. Each ring had an inner diameter of 123.8 mm and an axial length of 19.5 mm. In the 4-ring scanners, the rings were positioned at an axial pitch of 21 mm. Three different detector geometries were investigated: trapezoidal monolithic crystal detectors, rectangular monolithic crystal detectors, and detectors with  $8 \times 4$  crystal matrices. An illustration of the 4-ring scanner with trapezoidal detectors is presented in Fig. 7.2.1. The detector types are depicted in Fig. 7.2, which also shows the coordinate system used to specify positions and angles of incidence on the detector front surface. The trapezoidal crystals had a front surface of  $11.5 \times 19.5 \text{ mm}^2$ , a back surface of  $15.4 \times 19.5 \text{ mm}^2$  and a depth of 20 mm. The rectangular crystals

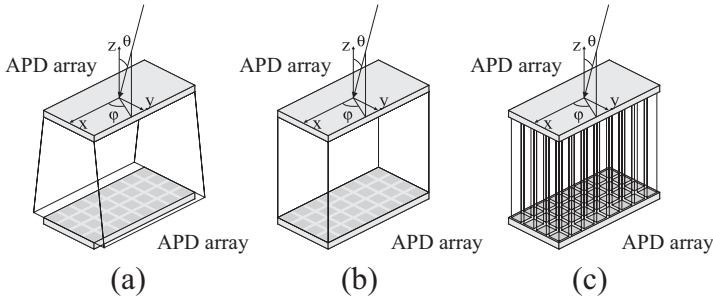


Figure 7.2: Detector types investigated: (a) trapezoidal, (b) rectangular, (c) pixel matrix.

had dimensions of  $19.5 \times 11.5 \times 20 \text{ mm}^3$ , and the matrix detectors had  $8 \times 4$  crystals of  $2 \times 2 \times 20 \text{ mm}^3$  at a pitch of 2.2 mm. The crystal material in each detector was LSO:Ce, and each module was coupled to 2 Hamamatsu S8550-SPL APD arrays, modelled as  $11.2 \times 19.5 \times 1.5 \text{ mm}^3$  slabs of silicon.

In each simulation, the locations and energy depositions of the interactions within the crystal of each 511 keV photon entering a detector were stored. The total energy deposited was blurred with a Gaussian distribution with a FWHM of 10% of the energy value as an approximation of the energy resolution measured with these detectors, see Chapter 4. Events with blurred total energy depositions outside an energy window of 250–750 keV were rejected. For each single event within the energy window, a detector dead time of 0.5  $\mu$ s was applied. All single events were stored in list mode for offline coincidence sorting.

The time stamp of each detected single was blurred with a Gaussian distribution with a FWHM of 2 ns, based on measurements of the timing resolution of a prototype detector module (see Chapter 4). A coincidence time window of 5 ns was used, approximately twice the coincidence timing resolution of 2.8 ns obtained experimentally [102]. Coincident events in which more than two detector modules were involved were rejected.

After sorting the coincidences, the entry point and incidence angle of each 511 keV photon was determined. Each entry point was then projected onto the detector y-axis (see Fig. 7.2), since the image resolution was determined in 2D only in this study. The projected entry points were then blurred by adding a positioning error randomly selected from the corrected 1D-PSF of the detector corresponding to the nearest test beam position and incidence angle (see Section 7.2.2). The lines-of-response (LORs) corresponding to these blurred entry points were then calculated and sorted into 2D sinograms.

### 7.2.2 Intrinsic detector PSF

The 1D-PSF of the trapezoidal detectors was measured according to the procedure outlined in Section 3.3.1. A prototype detector (LYSO20T-P) was stepped through a beam of 511 keV photons of  $d_b = 0.96$  mm FWHM along the detector y-axis in steps of 0.25 mm, i.e. in the plane of the detector ring. At each beam position,  $n_{\text{ref}} = 1500$  reference light distributions were recorded. This was done for incidence angles between  $\theta = 0^\circ$  and  $\theta = 40^\circ$ , in steps of  $5^\circ$ , at  $\varphi = 90^\circ$  (see Fig. 7.2), yielding a total of 9 data sets. The oblique sides of the crystals were included in the data sets at all angles of incidence. The entry point coordinate of each event in each of the data sets was estimated with the  $L$ -nearest neighbour method, using the leave-one-out approach (see Section 3.3.1).

The positioning error of each test event was calculated by subtracting the estimated coordinate from the true, known coordinate. This way, histograms of positioning errors were created for each beam position and each angle of incidence. Each of these histograms corresponds to the detector 1D-PSF at a certain position and angle of incidence on the front surface of the detector. In the present analysis, the 1D-PSFs were averaged over 1 mm data segments.

The intrinsic 1D-PSF exhibited by the detectors in a PET system corresponds to their response to an infinitely narrow beam. The measured 1D-PSFs were therefore corrected for the finite width of the test beam. The beam profile was determined using Monte Carlo simulations of an accurate model of the measurement setup in Geant4 [100], see Chapter 6. The procedure to correct the PSFs for the finite diameter of the test beam presented in Chapter 6 could not be used in this study, because the model on which it is based was only derived for normally incident 511 keV photons at the centre of the detector front surface. The intrinsic detector 1D-PSFs were therefore estimated by deconvolution of the measured 1D-PSFs with the simulated beam profile.

### 7.2.3 Scanner performance

#### Image spatial resolution

The system resolution obtainable with the proposed scanner type was investigated in 2D, by simulating a 1-ring system of trapezoidal detectors. To investigate the intrinsic resolution of this scanner, a 0.5 kBq mathematical point source emitting back-to-back annihilation photons was simulated, neglecting positron range and acollinearity. The source was placed at radial positions  $r$  in the field of view (FOV) ranging from  $r = 0$  mm (center FOV) to  $r = 29$  mm, in steps of 1 mm. A simulation of  $10^6$  events was performed at each source position, and no attenuation cor-

rection, normalisation or subtraction of random coincidences was performed. The LORs were binned into 2D sinograms with a bin size of  $r \times \phi = 0.5 \text{ mm} \times 0.9^\circ$ . Reconstruction of the sinograms was performed by filtered backprojection with a ramp filter with a cutoff at the Nyquist frequency, resulting in an image with pixels with a size of  $0.5 \times 0.5 \text{ mm}$ .

The system resolution obtainable with realistic point sources was investigated by simulating eight  $0.5 \text{ kBq } \varnothing 0.5 \times 1 \text{ mm}^3$   $^{18}\text{F}$ -sources each embedded in a  $\varnothing 4.6 \times 5 \text{ mm}^3$  PMMA cylinder, at radial positions ranging from  $r = 0 \text{ mm}$  to  $r = 35 \text{ mm}$  in steps of  $5 \text{ mm}$ . A total number of  $37 \cdot 10^6$  positron emission events were simulated, taking positron range and photon acollinearity into account. The LORs were binned into 2D sinograms with a bin size of  $r \times \phi = 0.5 \text{ mm} \times 0.9^\circ$ . Reconstruction of the sinograms was performed by filtered backprojection with a ramp filter with a cutoff at the Nyquist frequency, resulting in an image with pixels with a size of  $0.5 \times 0.5 \text{ mm}$ .

Finally, simulations were performed of a micro-Derenzo phantom, consisting of a  $\varnothing 77 \times 35 \text{ mm}^3$  PMMA cylinder with 6 segments of radioactive rods with diameters of 1.2, 1.6, 2.4, 3.2, 4.0 and 4.8 mm containing  $2 \text{ MBq}$  of  $^{18}\text{F}$ . The distance between the rods in each segment was twice the diameter, and the activity was contained in the central  $1 \text{ cm}$  of the axial field of view. A total number of  $3.3 \cdot 10^8$  events were simulated. No correction for scattered events, attenuation or random coincidences was performed, and the sinograms were not normalised. The sinograms were reconstructed using a 2D-OSEM algorithm with 10 subsets and 30 iterations, resulting in an image with pixels with a size of  $0.5 \times 0.5 \text{ mm}$ .

### Scanner sensitivity

To assess the scanner sensitivity, simulations of three 4-ring systems with trapezoidal monolithic detectors, rectangular monolithic detectors and crystal matrix detectors were performed, see Section 7.2.1. The sensitivity of each of these systems was investigated by stepping a  $1 \text{ MBq}$  point source of back-to-back  $511 \text{ keV}$  photons from the centre to the edge of the FOV, both axially and radially, in steps of  $1 \text{ mm}$ . At each source position,  $\sim 10^6$  events were simulated. An energy window of  $250\text{--}750 \text{ keV}$  was used for each detector. The sensitivity was calculated by dividing the true coincidence count rate by the activity of the point source.

### Count rate performance

The count rate performance of a scanner represents its ability to reject random and scattered coincidences at a given source activity. It can be quantified using

the noise equivalent count rate (NECR), which can be calculated using the relationship [15]:

$$\text{NECR} = \frac{T^2}{T + S + 2kR}, \quad (7.1)$$

where  $T$  is the rate of true coincidences,  $S$  is the rate of scattered coincidences,  $R$  is the rate of random coincidences and  $k$  is the ratio of the phantom diameter and the scanner diameter. The factor 2 in the denominator accounts for the method of randoms correction, which is assumed to be a delayed coincidence technique for the present study.

The NECR of the 4-ring system with trapezoidal detectors was determined using simulations of a mouse phantom and a rat phantom. The phantoms were modelled respectively as a  $\varnothing 36 \times 67 \text{ mm}^3$  and a  $\varnothing 60 \times 150 \text{ mm}^3$  water cylinder filled with uniform  $^{18}\text{F}$  activity.

## 7.3 Results

### 7.3.1 Spatial resolution

Fig. 7.3 shows the radial (squares) and tangential (triangles) FWHM intrinsic system resolution in response to mathematical point sources emitting back-to-back 511 keV photons at a range of radial distances from the CFOV. These numbers were obtained by linear interpolation of the intensity profile through the pixel with maximum intensity for each source position. The spatial resolution is essentially uniform and isotropic over a range up to 3 cm off-centre, in agreement with the excellent correction for the DOI previously reported for these detectors (see Chapter 4).

Fig. 7.4 shows an FBP reconstructed image of the eight  $\varnothing 0.5 \text{ mm}$   $^{18}\text{F}$  point sources. Linear interpolation of the profiles through the pixel with maximum intensity yields a system resolution at the CFOV of  $\sim 1.4 \text{ mm}$  FWHM and  $\sim 3.3 \text{ mm}$  FWTM. At 35 mm from the CFOV, this degrades to 2.1 mm FWHM and 4.1 mm FWTM radially, and 2.3 mm FWHM and 5.7 mm FWTM tangentially.

Fig. 7.5 shows 2D-OSEM reconstructed images of the micro-Derenzo phantom. In Fig. 7.5a, the source emitted back-to-back 511 keV photons, neglecting positron range and photon acollinearity. Attenuation and scatter within the phantom were set to zero. In Fig. 7.5b, a realistic positron source with an energy distribution corresponding to  $^{18}\text{F}$  was simulated, and photon acollinearity, attenuation and scatter within the phantom were taken into account. No attenuation correction, scatter correction or normalisation was applied to the data to create either

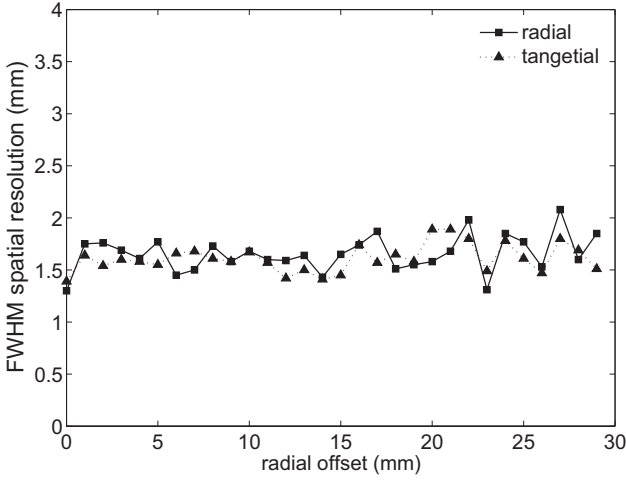


Figure 7.3: Radial (squares) and tangential (triangles) FWHM spatial resolution of a mathematical point source as a function of the radial position. Positron range and photon acollinearity were set to zero in these simulations.

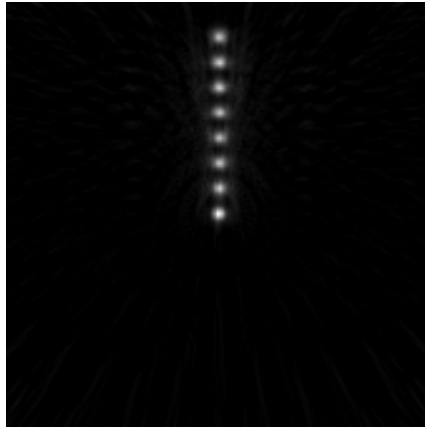


Figure 7.4: Reconstructed image of eight  $\text{Ø}0.5 \text{ } ^{18}\text{F}$  point sources at radial distances of 0, 5,  $\dots$ , 35 mm from the scanner CFOV.

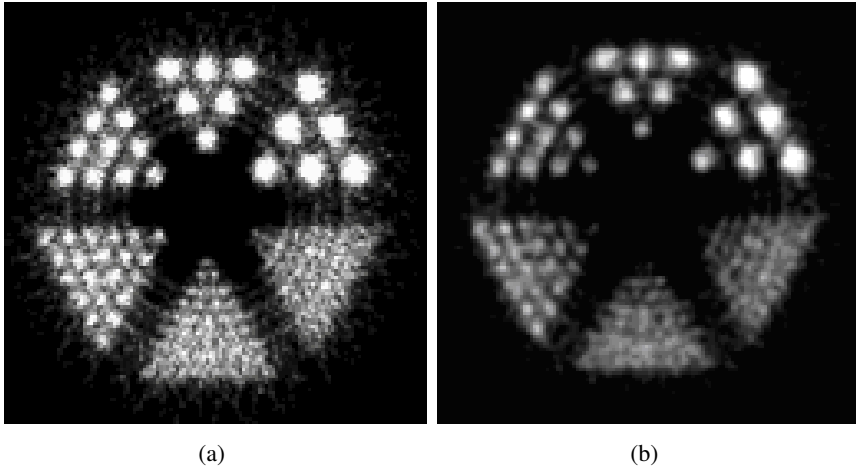


Figure 7.5: Reconstructed images of a micro-Derenzo hot rod phantom with rods with diameters of 1.2, 1.6, 2.4, 3.2, 4.0, and 4.8 mm, uniformly filled with activity. In (a), the source emits back-to-back photons, and positron range and photon acollinearity are neglected. Attenuation and scatter within the phantom are set to zero. In (b), a positron emitting source with an energy distribution corresponding to  $^{18}\text{F}$  is used, and photon acollinearity is taken into account, as well as attenuation and scatter within the phantom. Correction for attenuation and scattered events and normalisation were not applied to obtain these images.

image. No randoms correction was applied in view of the low activity (0.5 kBq) of the simulated sources.

In Fig. 7.5a, the 2.4 mm rods are clearly separated while the 1.6 mm rods are not, in agreement with the results presented for the mathematical point sources (Fig. 7.3). In Fig. 7.5b, the 2.4 mm rods can still be identified, but the separation is less distinct due to the blurring effect of positron range and photon acollinearity. Radial distortion of the rods on the outside of the FOV is observed in neither image, owing to the good DOI correction of the detectors.

Ring-shaped artefacts can be observed around each row of rods in Fig. 7.5a. Although less clearly discernible, these artefacts are also observed in Fig. 7.5b.

### 7.3.2 Sensitivity

The point source sensitivity is plotted in Fig. 7.6 as a function of the radial and axial distance from the CFOV for the three 4-ring systems with trapezoidal mono-

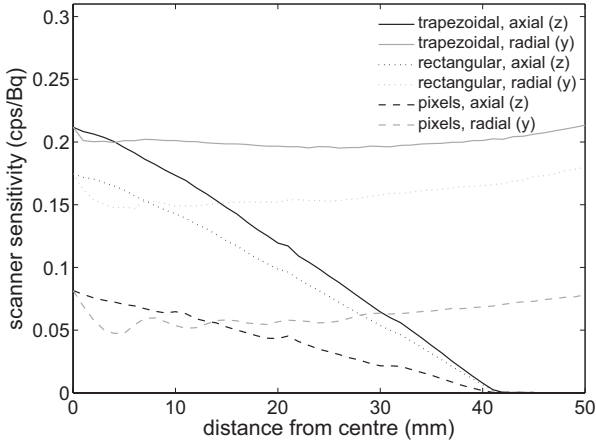


Figure 7.6: Axial and radial point-source sensitivity curves of the three 4-ring systems with trapezoidal monolithic detectors (solid lines), rectangular monolithic detectors (dotted lines), and crystal matrix detectors (dashed lines).

lithic detectors (solid lines), rectangular monolithic detectors (dotted lines), and crystal matrix detectors (dashed lines). The sensitivities at the CFOV are 21% for the trapezoidal detectors, 17.5% for the rectangular detectors and 8% for the crystal matrix detectors. The rectangular monolithic detectors have a sensitive volume that is  $\sim 56\%$  larger than that of the crystal matrix detectors, resulting in an increase of the scanner sensitivity of approximately a factor 2. The more favourable geometry of the trapezoidal detectors compared to the rectangular ones results in a further increase of the scanner sensitivity of 20%. In addition, the radial sensitivity profile is smoother for the trapezoidal detectors than for the other geometries, due to the reduced dead space between the detector modules.

### 7.3.3 Count rate performance

The noise equivalent count rate of the 4-ring scanner with trapezoidal detectors is plotted in Fig. 7.7 as a function of the total activity for the  $\varnothing 36 \times 67 \text{ mm}^3$  mouse phantom (solid line) and the  $\varnothing 60 \times 150 \text{ mm}^3$  rat phantom (dotted line). The NECR reaches a maximum of 2000 kcps with the mouse phantom at an activity of 70 MBq. The NECR obtained with the rat phantom is considerably lower, reaching a maximum of 550 kcps at an activity of 70 MBq. This is due to the larger dimensions of the rat phantom, of which approximately 48% of the volume



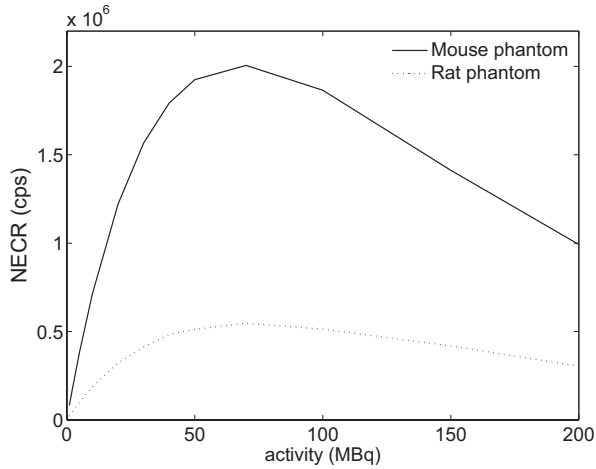


Figure 7.7: Noise equivalent count rate as a function of total activity of the 4-ring scanner with trapezoidal detectors for the mouse phantom (solid line) and the rat phantom (dotted line).

lies outside the scanner FOV. This activity outside the FOV leads to an increased number of random coincidences, but does not contribute to the number of true coincidences. In addition, the number of scattered events coming from within the FOV is larger in the rat phantom due to its larger diameter. For both NECR curves, only a minor deviation from linearity is observed at activities commonly used in small-animal PET ( $< 40$  MBq).

## 7.4 Discussion

The unconventional shape of the detector point spread function complicates estimating the system resolution that should be achievable intuitively. In order to obtain such an estimate, an image of a mathematical point source at the CFOV was re-created using idealised detector PSFs. This was done by creating a model 1D-PSF, convolving an energy centroid distribution in response to a zero-width pencil beam with a Gaussian distribution. The standard deviation of the Gaussian was set at  $\sigma = 0.46$  mm, which is a common value for our detectors (see Chapter 6, Fig. 6.6a). This resulted in a 1D-PSF with a FWHM of 1.24 mm. This model PSF was applied to all entry points in the data, regardless of position or incidence angle, eliminating any statistical variances or deteriorations at the edges of the

detectors observed in the measured PSFs. These new entry points were used to calculate a sinogram, which was subsequently reconstructed in the same way as the original study. The image spatial resolution resulting from this idealised situation was 1.10 mm FWHM at the CFOV, an improvement of  $\sim 0.25$  mm compared to the result in Fig. 7.3.

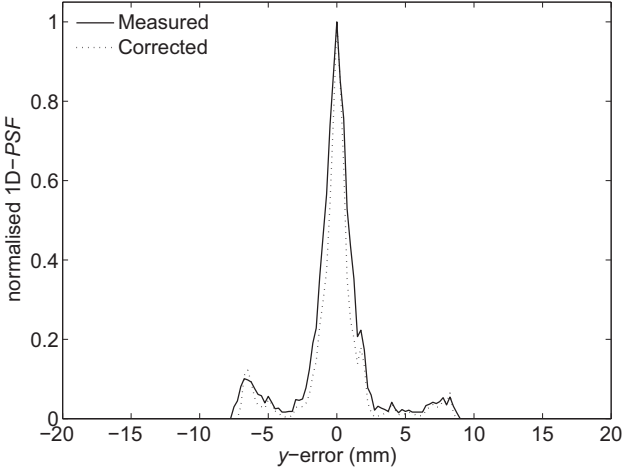
A number of possible causes for this difference can be identified. Firstly, the degradation of the detector spatial resolution at the crystal edges is likely to have an adverse effect on the image resolution. This would suggest that reducing the number of events taking place close to a detector edge, i.e. using detectors with a larger surface area and more light sensors per crystal surface, may result in a relative reduction of these effects. However, this approach would also result in a lower average number of detected scintillation photons per light sensor, reducing the signal-to-noise ratio per pixel, which could result in an overall deterioration of the detector PSF.

A second cause could be the limited statistics in the measured PSFs used in this study. Increasing the number of test events per local PSF may make the deconvolution of the test beam more accurate, possibly leading to an improved image resolution. The present number of events per local PSF was a compromise between statistics and measurement and computation times.

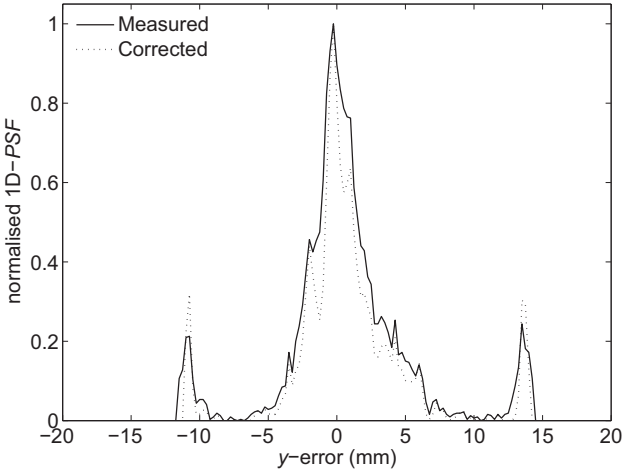
A further improvement of the image quality could be achieved by reducing the ring-shaped artefacts observed in Fig. 7.5. It was found that a significant fraction of the measured 1D-PSFs, mainly at oblique incidence angles, had artifacts at the edges of the histograms, which may give rise to the observed effects. Examples of such artefacts are shown in Fig. 7.8, which shows measured (solid lines) and deconvolved (dotted lines) 1D-PSFs obtained at  $y = 0.5$  mm and  $\theta = 0^\circ$  (a), and at  $y = 5.5$  mm and  $\theta = 30^\circ$  (b). The artefacts in the 1D-PSF in (b) at the edges of the histogram are clearly visible.

A cause for these artefacts has thus far not been established. They were also observed in 1D-PSFs obtained by Monte Carlo simulations in GEANT4 [100], making it unlikely that they are the result of a flaw in the experimental procedure. Furthermore, energy thresholding was not found to lead to a reduction of the artefacts. It may be that internal reflections in the crystal cause similarities in the scintillation light distributions at different entry points. In that case, a reduction of the artefacts could be achieved by using crystals with a rough or an absorbing surface. Finally, it may also be that using an alternative event positioning scheme, for example one using neural networks, would result in a reduction of the artefacts.

Further improvements of the image quality obtained with the Micro-Derenzo phantom could be obtained by further optimising the image reconstruction algo-



(a)



(b)

Figure 7.8: Measured (solid lines) and corrected (dotted lines) 1D-PSFs obtained at  $y = 0.5$  mm and  $\theta = 0^\circ$  (a), and at  $y = 5.5$  mm and  $\theta = 30^\circ$  (b).

rithm. For instance, scatter correction, attenuation correction and normalisation of the sinograms have not been performed in this pilot study. Furthermore, using more sophisticated reconstruction techniques such as resolution recovery could lead to an improved image resolution.

## 7.5 Conclusions

A pilot study assessing the performance of small-animal PET scanners based on monolithic scintillator detectors was presented in this chapter. The study was based on Monte Carlo simulations using measured detector line spread functions and other detector characteristics as input. The image resolution of a 1-ring system with trapezoidal monolithic detectors was investigated in 2D. A system resolution of  $\sim 1.4$  mm FWHM was found at the centre of the FOV using a  $\varnothing 0.5$  mm point source of  $^{18}\text{F}$ . Very little degradation of the system resolution with increasing radial distance from the CFOV was found, and no anisotropy in the system resolution was observed. This is in agreement with the excellent correction for depth-of-interaction reported previously for these detectors.

Further improvements to the image resolution are likely to be achievable by an adjustment of the detector geometry. This could reduce the relative number of events entering the detectors close to a crystal edge, which exhibit a larger position uncertainty than events entering at the centre of the crystals. An additional improvement of the image resolution is expected with the reduction of artefacts on the measured PSFs, which may be achieved using alternative event positioning algorithms or crystals with a different surface finish.

The favourable geometry of the trapezoidal detectors results in a very high peak sensitivity of 21% at low activity in a 4-ring system, a great improvement compared to the peak sensitivity of 3–4% currently reported for small-animal PET systems. Furthermore, a high peak noise equivalent count rate of 2000 kcps was calculated for a mouse phantom in this system, using an energy window of 250–750 keV, a coincidence time window of 5 ns and a detector dead time of 1000 ns. These very high values can lead to a significant improvement of the signal-to-noise ratio of reconstructed images compared to the current standards, improving image quality, and permitting more accurate quantification of tracer concentrations in dynamic small-animal PET studies.

## Chapter 8

# General discussion

This thesis focused on the characterisation and analysis of the performance of monolithic scintillator detectors, aimed at an application in high-resolution PET. The detectors were demonstrated to have properties that could result in a PET system with very good performance characteristics. The estimated intrinsic detector spatial resolution was comparable to that of current state-of-the-art high-resolution PET systems. The detector spatial resolution was furthermore shown to be essentially independent of the angle of incidence of the annihilation photons. As a result, the image spatial resolution of a scanner based on these detectors is not degraded by the varying depth of interaction of the incident photons. This permits the use of a thick layer of scintillation material to achieve maximum scanner sensitivity, without degrading the image resolution at the periphery of the field of view (FOV). Indeed, simulations of a 1-ring PET scanner with 20 mm thick monolithic trapezoidal LSO crystals yielded a 2D system resolution in response to a  $\varnothing 0.5$  mm  $^{18}\text{F}$  point source of 1.4 mm FWHM at the centre of the FOV (CFOV), with little degradation at off-centre positions (see Chapter 7). The point source sensitivity of a 4-ring version of this scanner reaches 21% at the CFOV, a great improvement compared to the peak sensitivities of 3–4% currently reported in state-of-the-art small-animal PET systems.

An additional advantage of the proposed detector design is that the APD arrays used to detect the scintillation light retain their functionality in the strong magnetic fields prevalent in MRI systems [103]. This facilitates combining a PET system based on these detectors with an MRI device. The combination of PET with MRI enables accurate coregistration of the functional PET data with the anatomical information provided by the multitude of contrast possibilities of MRI. In addition, it opens up the possibility of the simultaneous acquisition of dual-

modality functional information, e.g. by combining PET with blood-oxygen level dependent (BOLD) MRI or MR spectroscopic imaging (MRSI).

Implementation of monolithic scintillator detectors in a PET system requires addressing a number of technical challenges. One of these is the design of an application specific integrated circuit (ASIC) for the frontend electronics, necessary to accommodate the large number of readout channels in the small area available. Such an ASIC should provide individual preamplifying and shaping for multiple (e.g. 16) channels, and should have a low power consumption. It should have sufficient dynamic range to handle the strongly varying light intensities incident on the APD pixels, and should provide a low noise level to allow accurate positioning of events. In addition, it should provide a low-noise timing signal with a slew rate shorter than the decay time of the scintillator used, and a digital constant fraction discriminator would be necessary to provide sufficiently accurate time pickoff. These are challenging requirements; however, several integrated circuit frontend chips have recently been designed for similar purposes, suggesting that it should indeed be feasible to design an ASIC suitable for monolithic scintillator detectors [104, 105].

A PET scanner based on monolithic scintillator detectors would also require a new data acquisition (DAQ) system. To accurately determine the entry points of the incident annihilation photons on the front surfaces of the detectors, information is needed on the angle of incidence, which can be deduced from the positions of the detector pair triggering in coincidence [72]. This approach requires that coincidence sorting be done prior to the estimation of the entry points. Storing all channel data of each single event for offline coincidence sorting and entry point estimation would require a data stream and storage space approximately 64 times as large as in the recently developed DAQ system of the MadPET-II system, which also uses Hamamatsu S8550 APD arrays and has 64 channels per detector module [106]. An alternative could be to cache the channel data and time stamps of all singles events in each detector module in fast buffer memories for a specified period of time. These buffers could then be periodically read out and sorted for coincidences, after which the channel data corresponding to coincident events could be transferred to disk for offline estimation of the entry points.

The nearest neighbour method used throughout this thesis for estimating the entry points gives excellent results, but is too computationally intensive to be a realistic option in a practical setting. A different position estimation algorithm should therefore be used in a PET system. Alternative options such as neural networks and support vector machines have been reported on elsewhere [107]. Neural networks have the advantages of being much faster than statistical methods

and of yielding continuous instead of discrete coordinates as output. However, they have also been shown to exhibit a bias in the position estimation at the detector edges, resulting in a ‘pincushion’ distortion such as commonly observed in block detectors. Whether this would have a significant deleterious effect on the system resolution could be investigated with Monte Carlo simulations similar to those presented in Chapter 7.

Irrespective of the specific positioning procedure used, the proposed method to eliminate DOI effects requires the use of sets of previously recorded reference data. A method to efficiently collect such data in a practical setting is therefore needed. Important steps in the development of such a method have already been taken [108].

A renewed interest in time-of-flight (TOF) PET has arisen in the past years, stimulated by the development of new scintillating materials such as LSO [29] and  $\text{LaBr}_3$  [109] and by recent improvements in photodetector technology and electronics. In TOF-PET, the time difference between the detection of two photons forming a coincident pair is used to define a region on the line of response within which the annihilation must have taken place. This information can be used in image reconstruction, leading to a strong reduction of statistical variance in the image [110, 111]. A coincidence timing resolution of 500 ps FWHM confines the annihilation event to a line segment on the LOR of  $\sim 7.5$  cm long [111], sufficient to provide a significant improvement of the image quality in clinical PET. Timing resolutions of such order are nowadays readily achievable with PMTs, and a commercial LYSO-based TOF-PET system has recently been released by Philips.

However, achieving timing resolutions adequate for time-of-flight is difficult with APDs because of the low signal-to-noise ratios these currently produce. A possible solution to achieving TOF with monolithic scintillator detectors would be to use arrays of silicon PMTs (SiPMs) instead of APD arrays. A SiPM typically consists of hundreds of small APD-like structures operated in Geiger (on-off) mode, causing the output signal to be proportional to the number of incident photons at sufficiently low light intensities. The output signals of SiPMs are much higher than those of APDs, allowing the use of current amplifiers instead of charge-sensitive preamplifiers. This way, the signal rise time is no longer limited by the scintillator decay time, but rather by its rise time and by the slew rate of the frontend electronics. Much higher timing resolutions are therefore potentially achievable with these devices: a coincidence timing resolution of 0.78 ns has been reported with two opposing LSO-SiPM detectors at an energy of 511 keV [112]. SiPM arrays suitable for high-resolution position-sensitive radiation are being developed, but still require a number of improvements. The first

arrays of SiPMs have recently been introduced to the market (SensL, Cork, Ireland). Current development efforts are aimed at improving the photon detection efficiency by matching the devices' spectral response to the wavelength of commonly used scintillators, and at improving the signal-to-noise ratio by reducing the devices' relatively high dark currents.

Overcoming these challenges could mean a great step forward in PET technology. It could lead to a paradigm shift from detectors based on scintillation crystal matrices read out by PMTs, to detectors using monolithic scintillators read out by solid-state light sensors [113].



## Appendix A

# Characterisation of setup components

This appendix gives an overview of characterisation measurements of several key components of the experimental setup.

### A.1 APD arrays

The Hamamatsu S8550 APD arrays consist of 2 banks of  $2 \times 8$  pixels each. Each bank has a specific bias voltage  $V_{50}$ , at which the gain  $M = 50$  according to the manufacturer specifications. Between banks in the same array, and between different arrays, differences in  $V_{50}$  of 10–20 V are common.

The gain of several arrays was measured as a function of the bias voltage using 5.89 keV X-rays from a  $^{55}\text{Fe}$ -source directly incident on the APDs. The number of electron-hole (e-h) pairs created per X-ray photon is obtained by dividing its energy by the mean ionisation energy, which is 3.6 eV in Si. Pulse height spectra were recorded on each channel, and the full-energy peaks of these spectra were fitted with a Gaussian function. Pulse height spectra in response to a square wave pulser connected to the test inputs of the preamplifiers were also recorded. As the input capacitance of these test inputs is accurately known, the charge delivered by the test pulser to the preamplifiers is known also. Comparison of the peak position of an X-ray spectrum to that of the corresponding test pulse spectrum thus yields the APD gain. In these experiments, each shaping amplifier was adjusted to give a zero baseline-offset averaged over its 16 channels (see Section A.3), and all spectra were corrected for the DC-offsets observed in the MC-ADCs (see Section A.4).

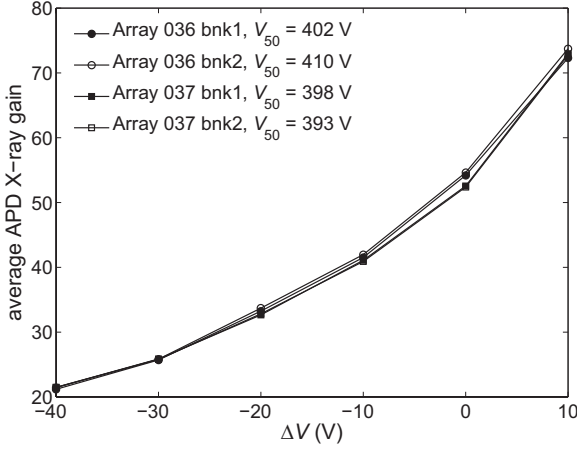


Figure A.1: APD gain averaged over 16 channels per bank, measured with 5.89 keV X-rays, as a function of  $\Delta V \equiv V - V_{50}$ .

Fig. A.1 shows the gain of two APD arrays (serial numbers 036 and 037) averaged over the 16 channels of each bank. The bias voltage is expressed in terms of  $\Delta V \equiv V - V_{50}$ , where  $V$  is the applied bias voltage. These results show that although  $V_{50}$  varies significantly between the different banks, the average gains as a function of  $\Delta V$  are equal within 4%.

Fig. A.2a shows the gain of each individual channel of APD array 036 measured at  $\Delta V = 0$  V. Differences in the gain are observed between the channels. The gain dispersion, expressed as the gain standard deviation relative to the average gain over 32 channels, is plotted as a function of  $\Delta V$  for arrays 036 and 037 in Fig. A.2b. For both arrays, the gain dispersion increases by a factor  $\sim 1.5$  in the bias voltage range between  $\Delta V = -40$  V and  $\Delta V = +10$  V. The average gain increases by a factor  $\sim 3.5$  in the same voltage range (see Fig. A.1).

## A.2 Preamplifiers

Preamplification of the APD signals is performed using low-noise charge-sensitive preamplifiers (CSPs), type Cremat CR-110. Table A.1 lists a number of properties of these preamplifiers, as provided by the manufacturer.

The rise time of the preamplifiers was measured using a square wave test pulser with a rise time of  $\sim 4$  ns coupled to the preamplifier input via 1.8 pF coupling

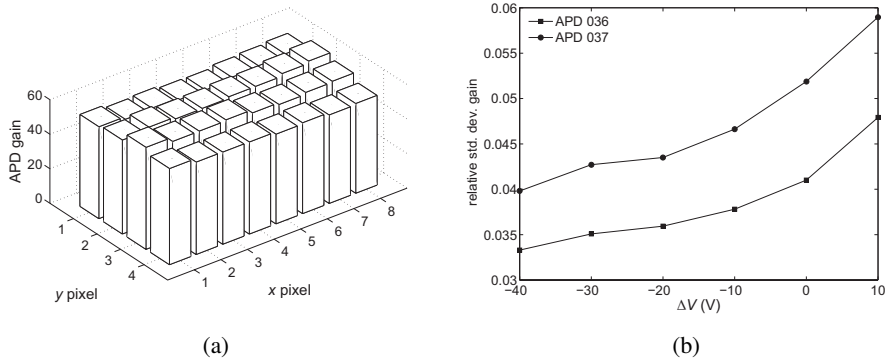


Figure A.2: Gain differences between APD pixels: (a) Gain per pixel of array 036 at  $\Delta V = 0$  V and (b) relative standard deviation of the gain of arrays 036 and 037 as a function of  $\Delta V$ .

Table A.1: Properties of the Cremat CR-110 charge sensitive preamplifiers, as provided by the manufacturer.

Parameter	Value	Unit
Input JFET:		
Eff. input capacitance	13	pF
Transconductance	50	mS
Gate-source leakage current (max)	1	nA
Gate-source leakage current (typ)	< 10	pA
Feedback capacitance ( $C_f$ )	1.4	pF
Feedback resistor ( $R_f$ )	100	M $\Omega$

capacitors, with the APD array biased at  $\Delta V = 0$  V connected to the preamplifier inputs. The observed 10%–90% rise time was approximately 20 ns. In the readout of a scintillation detector using an integrating charge-sensitive preamplifier with a sufficiently high slew rate, the signal rise time is determined by the decay time of the scintillator. Since the materials LSO:Ce and LYSO:Ce have a decay time of  $\tau_d \sim 40$  ns, preamplifier signal rise times of this same order can be expected in scintillation readout.

To assess the noise performance of the preamplifiers, electronic noise measurements were carried out as a function of the amplifier shaping time. A preamplifier was placed in a metal measurement box to minimise interference, and a 1.8 pF capacitor was connected to its input. The preamplifier output signal was amplified with an Ortec 572 shaping amplifier, and the root-mean-square (rms) noise was determined with an HP 3400A rms-meter. The measurements were performed at room temperature.

The results of these measurements are shown in Fig. A.3. The electronic noise is expressed as the equivalent noise charge (ENC), which describes the rms noise amplitude at the shaping amplifier output in terms of the charge needed at the preamplifier input to create an output pulse with the same amplitude, expressed in electrons. Assuming equal time constants for differentiation and integration, the squared equivalent noise charge of a detector-amplifier system can be written as:

$$ENC^2 = \frac{1}{q^2} \left( \frac{aC_{tot}^2 A_1}{\tau} + \left[ 2\pi a_f C_{tot}^2 + \frac{b_f}{2\pi} \right] A_2 + bA_3 \tau \right), \quad (A.1)$$

where  $a$  is the spectral density of the series white noise,  $b$  is the spectral density of the parallel white noise,  $a_f$  is the coefficient of the series  $1/f$  noise, and  $b_f$  is the coefficient of parallel  $1/f$  noise.  $C_{tot}$  is the total input capacitance of the detector-preamplifier system,  $\tau$  is the amplifier shaping time, and  $A_1$ – $A_3$  are dimensionless constants which are characteristic of the shaping network used. A least-squares fit of this model to the data is also presented in Fig. A.3, indicating the relative contributions of white series and parallel noise and  $1/f$  noise.

Because the input capacitance and leakage currents are different in the present measurements than when an APD is connected to the preamplifier input, the low noise level of  $< 300$   $e^-$  rms presented in Fig. A.3 will not be reached in the latter situation. However, the leakage current of the Hamamatsu S8550 APDs was such that the optimum shaping time, representing a balance between serial and parallel white noise, was shorter than those available on commonly used shaping amplifiers such as the Ortec 572, the parallel component dominating the ENC at each shaping time. Although a short enough shaping time could be reached with the CAEN N568BB shaping amplifiers, it was found that the shaping constants

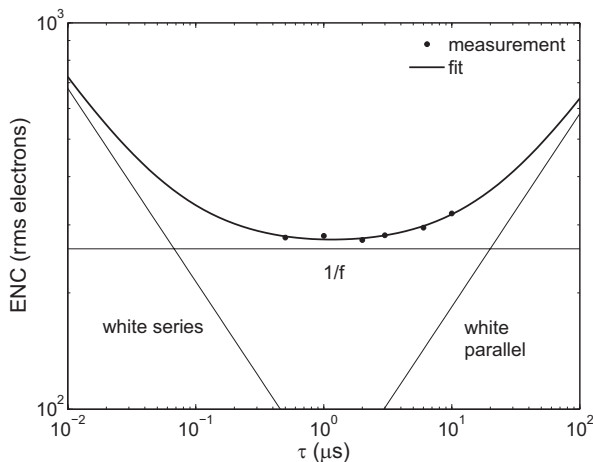


Figure A.3: Equivalent noise charge of a Cremat CR-110 preamplifier at room temperature with a 1.8 pF capacitor at the input as a function of the shaping time of an Ortec 572 shaping amplifier.

$A_1$ – $A_3$  of these amplifiers were not equal for all shaping times (see Section A.3), making a fit with the model Eq. (A.1) meaningless. The measurements presented here do however give a good indication of the low noise levels that can be reached with these preamplifiers.

## A.3 Shaping amplifiers

### A.3.1 Linearity

The linearity of the shaping amplifiers was tested by applying pulses with different amplitudes to the input using an Ortec 419 precision pulser producing tail pulses with a rise time of  $\sim 10$  ns. Its circuitry was internally modified to provide a pulse decay time of  $\sim 100 \mu\text{s}$  in order to comply with the range of decay times accepted by the shaping amplifiers. The pulser output was terminated with a  $50 \Omega$  resistor at the amplifier input to avoid pulse distortion. The amplitude of the pulses was measured using a Tektronix TDS3032 digital oscilloscope (Tektronix, Beaverton, OR, USA).

Fig. A.4 shows the results of such a measurement on channel 00 of amplifier 1, at a shaping time setting of  $\tau = 0.2 \mu\text{s}$  and a gain of approximately 30. The line

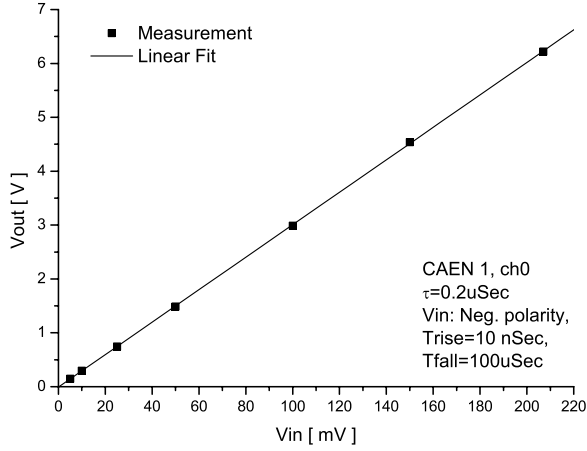


Figure A.4: Output versus input pulse amplitude of channel 00 of amplifier 1, at a shaping time setting of  $\tau = 0.2 \mu\text{s}$  and a gain of approximately 30.

represents a linear fit through the data. The data points have a maximum deviation from the fit of approximately 1%. Similar results were obtained at other shaping time settings.

### A.3.2 Gain dispersion

The gain dispersion between different amplifier channels was investigated both for the fast and the slow output branch, by applying pulses of 12.5 mV in parallel to all amplifier inputs. The gain of the slow branch was set to approximately 86.4, and the shaping time was set to  $\tau = 0.2 \mu\text{s}$ . The relative deviation from the average gain of each channel is indicated in Fig. A.5. The gain deviations lie between  $\pm 2\%$  in the fast branch and between  $+2\%$  and  $-4.5\%$  in the slow branch. Similar numbers were found for the other shaping time settings of the slow branch.

### A.3.3 Offset

The DC-offset of the slow branch of the shaping amplifiers can be adjusted, but only for all 16 channels simultaneously. The individual channels do not have equal DC-offsets, however. This is illustrated in Fig. A.6, where the DC-output

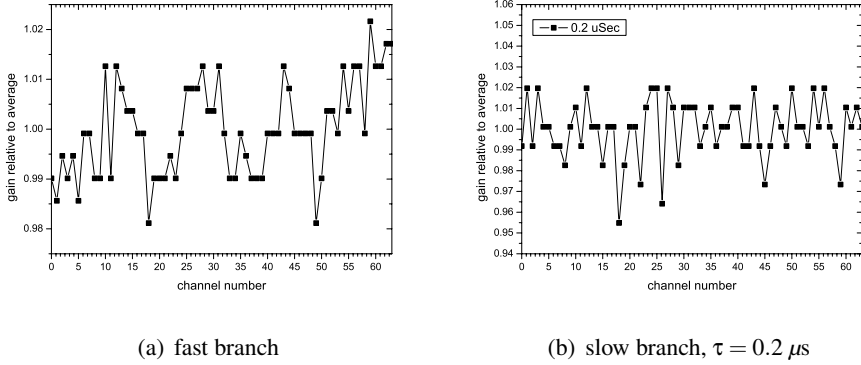


Figure A.5: Channel gains relative to the average of all 64 channels of the shaping amplifiers. The average gain in the slow branch was approximately 86.4 and the shaping time setting was  $\tau = 0.2 \mu\text{s}$ .

of each channel is measured at the two extrema of the settable offset range. A maximum difference of  $\sim 17 \text{ mV}$  is observed between channels. In comparison, the amplifiers have an output voltage range of 4 V. The differences remain constant over the range of offsets, the difference between the maximum and minimum offset being  $279 \pm 1 \text{ mV}$  for each channel in this case.

### A.3.4 Shaping constants

Inspection of the pulse peaking time at each shaping time setting showed a longer peaking time at  $\tau = 0.1 \mu\text{s}$  than would be expected based on the nominal value, see Table A.2. To investigate this, the frequency response of each shaping circuit was calculated analytically based on component values taken from the electronic circuit diagram provided by the manufacturer. As a check, the response of each shaping circuit was also simulated in PSPICE, using the same component values. The third column in Table A.2 shows the pulse peaking times resulting from these simulations. As these values match very well with the measured ones, it was assumed that the correct component values were used in the calculations for the different stages. It is noted that the analytical calculations did not take the bandwidth limitations of the opamp into account, whereas the simulations did.

The slow branch of the amplifiers consists of a course gain stage which is different for each shaping time followed by a common fine gain stage. Based on the analytic filter frequency responses, the shaping constants  $A_1$ – $A_3$  were calcu-

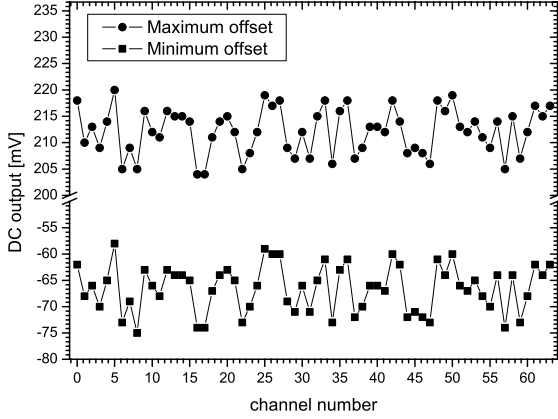


Figure A.6: DC output of each amplifier channel for the maximum (circles) and the minimum (squares) offset setting.

lated for each of the four available shaping times, with and without taking the fine gain stage into account. In columns 4–6 in Table A.2, the results of the calculations without the fine gain stage are presented. In this case, the constants  $A_1$ – $A_3$  are roughly constant for the three longest shaping times, but are different for  $\tau = 0.1 \mu\text{s}$ . This indicates that the frequency response of the course gain stage at this shaping time is different from the frequency response at other shaping times. When the fine gain is stage included in the calculations, the constants  $A_1$ – $A_3$  are found to differ even more between different shaping times, as shown in the last three columns in Table A.2. It was found that this is due to a parasitic RC-integration stage with a time constant of  $\sim 0.22 \mu\text{s}$  within the fine gain circuit, independent of the shaping time setting. This further distorts the shape of the pulses for the  $\tau = 0.1 \mu\text{s}$  and  $\tau = 0.2 \mu\text{s}$  shaping times.

These effects do not preclude the use of these devices as shaping amplifiers in these experiments. However, they do have the consequence that the peaking times of the shortest shaping constants are not as short as would be expected, and that fitting the ENC as a function of the shaping time using the model in Eq. (A.1) is meaningless with these amplifiers.



Table A.2: Calculated shaping constants at different shaping times of the slow branch of the CAEN N568BB spectroscopy amplifiers.

nominal $\tau$ ( $\mu\text{s}$ )	pk. time ( $\mu\text{s}$ )		Not including fine gain			Including fine gain		
	meas.	sim.	$A_1$	$A_2$	$A_3$	$A_1$	$A_2$	$A_3$
0.1	0.38	0.36	0.146	1.057	13.296	0.087	1.025	21.607
0.2	0.54	0.54	0.344	1.074	5.625	0.248	1.048	7.368
1	1.8	1.8	0.347	1.077	5.576	0.328	1.067	5.711
3	5	5	0.395	1.071	4.865	0.392	1.069	4.875

## A.4 Multichannel ADCs

The MC-ADCs were calibrated by measuring the digital output of each channel as a function of the input voltage. A precision pulser (BNC DB-2), generating pulses with a semi-Gaussian shape with a time constant of approximately  $1 \mu\text{s}$ , was used. The input voltages were measured using a Tektronix TDS3054 digital oscilloscope. Fig. A.7 shows the result of such a measurement for one ADC channel. A linear fit to these data shows a significant positive offset in the ADC output at zero input voltage. The results of such fits for all 64 channels of the two MC-ADCs are summarised in Fig. A.8. A slight dispersion in the slope of the curves is observed between the channels (Fig. A.8a). The offsets, shown in (Fig. A.8b), have an average value over 64 channels of 95 ADU. This corresponds to 7 least significant bits (LSBs), which is significant compared to the 12-bit resolution of the ADCs. Therefore, the ADC output should be corrected for these effects if absolute data are needed.

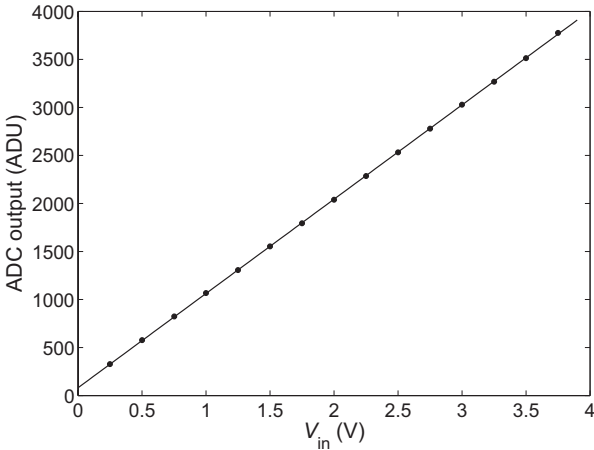


Figure A.7: Calibration of ADC channel 00.

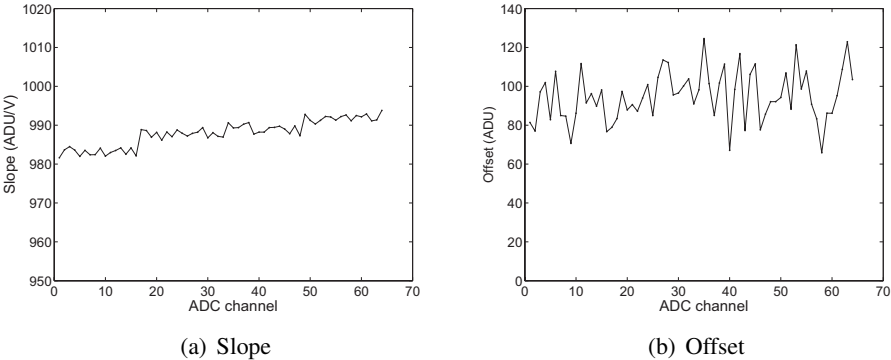


Figure A.8: Results ADC calibration per channel: slopes (a) and offsets (b).

# Appendix B

## Positioning algorithm

### B.1 Algorithm optimisation

#### B.1.1 Number of nearest neighbours

The performance of the position estimation algorithm depends on the number of nearest neighbours  $L$  and on the number of reference events per beam position  $n_{\text{ref}}$ . These dependencies were examined in a 1D experiment with sample LYSO20-P2, a  $20 \times 10 \times 20 \text{ mm}^3$  polished LYSO:Ce crystal, coupled to two APD arrays. In this experiment, a data set was collected by stepping the beam over the crystal in steps of 0.25 mm between  $-10 \leq x \leq 10 \text{ mm}$ . The measured data set was randomly split into  $n_{\text{ref}}$  reference events and  $n_{\text{tst}}$  test events per beam position. A 1D-PSF was then created for various values  $L$  (see Section 3.3.1), using test data containing events between  $-3 \leq x \leq 3 \text{ mm}$ , with  $n_{\text{tst}} = 1000$ . This experiment was performed for values of  $n_{\text{ref}}$  of 200, 750 and 2500.

Fig. B.1a shows the width of the 1D-PSF, expressed in  $\sigma_{\text{PSF}}^*$  (see Section 3.3.1), as a function of  $L$  for the different values of  $n_{\text{ref}}$ . The PSF width decreases with increasing  $L$  at low values of  $L$ , reaches a minimum, and increases again at higher values of  $L$ . This can be explained by considering that for  $L = 1$  and  $N_{\text{ref}} \rightarrow \infty$ , the nearest neighbour algorithm behaves as a proportional estimator, having a maximum probability of misclassification of two times the Bayes error probability. On the other hand, for  $L \rightarrow \infty$  and  $N_{\text{ref}} \rightarrow \infty$  with  $L/N_{\text{ref}} \rightarrow 0$ , the probability of misclassification approaches the Bayes error probability, i.e., the probability of misclassification reduces to approximately half that for  $L = 1$  (see Section 6.2) [114, 115].

Because of the finite size of the reference, the optimum value of  $L$  may be expected to depend on  $n_{\text{ref}}$ . However, since  $\sigma_{\text{PSF}}^*$  remains relatively constant over

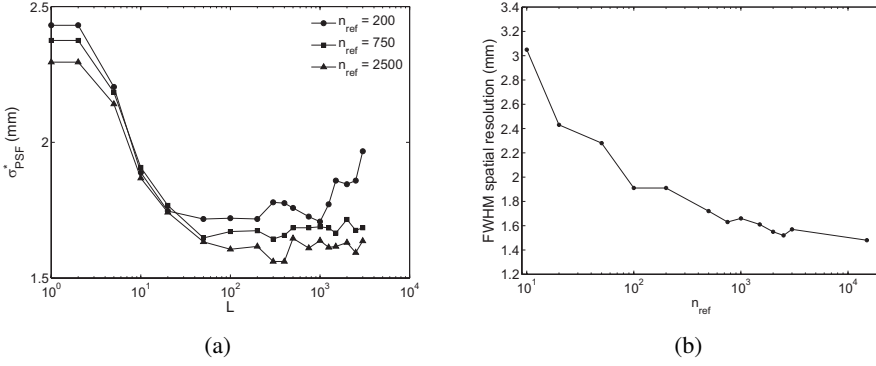


Figure B.1: (a): Width  $\sigma_{\text{PSF}}^*$  of the measured 1D-PSF of a  $20 \times 10 \times 20$  mm<sup>3</sup> polished LYSO:Ce crystal (LYSO20-P2) coupled to two APD arrays, as a function of  $L$  for different values of  $n_{\text{ref}}$ , and (b): FWHM of the 1D-PSF of the same detector as a function of the number of reference events per beam position, using the value of  $L$  that minimised  $\sigma_{\text{PSF}}^*$  at each value of  $n_{\text{ref}}$ . The 1D-PSFs were averaged over  $-3 \leq x \leq 3$  mm.

a wide range of values of  $L$  at each value of  $n_{\text{ref}}$ , such a dependence cannot be clearly observed in these experiments.

### B.1.2 Number of reference events

In Fig. B.1b, the FWHM 1D spatial resolution of the same detector is shown as a function of  $n_{\text{ref}}$ . At each point on the curve, the 1D-PSF was calculated using the value of  $L$  that minimised  $\sigma_{\text{PSF}}^*$ . Although these results suggest that further improvement of the spatial resolution may be achieved with  $n_{\text{ref}} > 15000$ , an improvement of only  $\sim 0.05$  mm FWHM is observed with a doubling of the number of reference events above approximately  $n_{\text{ref}} = 1500$ . As a compromise between measurement and CPU times and spatial resolution, all 1D experiments have therefore been performed using  $n_{\text{ref}} = 1500$ , unless stated otherwise. All 2D experiments have been performed using  $n_{\text{ref}} = 500$ .

## B.2 Resolution uncertainty

The uncertainty in the FWHM and FWTM spatial resolutions produced by the position estimation algorithm was estimated by performing multiple independent 1D measurements on the same crystal, leaving all experimental conditions the same

for each measurement. Ten datasets were collected on the same grid as described above (Section B.1.1), each containing  $n_{\text{ref}} = 1500$  reference events per beam position. A 1D-PSF was created with each data set using the leave-one-out approach (see Section 3.3.1), using the value of  $L$  that minimised  $\sigma_{\text{PSF}}^*$  for each. The FWHM and FWTM of each 1D-PSF was then calculated by linear interpolation of the histogram. This resulted in  $2\sigma$  uncertainties of approximately 0.05 mm for the FWHM and 0.15 mm for the FWTM. Because of the considerable time involved in performing this type of experiment, this procedure was only performed for this crystal and only in 1D, and the results were assumed representative of the uncertainties obtained in other experiments.



## Appendix C

# Equivalent noise charge of the fast amplifier branch<sup>1</sup>

In the fast branch of the CAEN N568BB amplifiers, the CSP tail pulses are differentiated with a fixed time constant  $\tau_d$ . The pulses are subsequently integrated in the TFA, with an adjustable time constant  $\tau_i$  (see Section 3.2). This system can be modeled as a CR-RC circuit, of which the equivalent noise charge in the general case of unequal time constants can be written as [84]:

$$ENC_f^2 = \frac{A}{q^2} (aC_{\text{tot}}^2 + \tau_d \tau_i b), \quad (\text{C.1})$$

where

$$A = \frac{(\tau_d - \tau_i)^2}{2\tau_d \tau_i (\tau_d + \tau_i)^2 \left[ \left( \frac{\tau_d}{\tau_i} \right)^{\frac{\tau_i}{\tau_d + \tau_i}} - \left( \frac{\tau_d}{\tau_i} \right)^{\frac{\tau_d}{\tau_d + \tau_i}} \right]^2}. \quad (\text{C.2})$$

The  $1/f$  noise components are omitted in this analysis for the sake of clarity.

Expressions for the terms  $\beta_1$  and  $\beta_2$  introduced in the timing resolution model can now be given (see Eq. (5.16)), considering that  $\beta_2$  contains only the parallel white noise contribution which is due to the amplified portion of the leakage current, and  $\beta_1$  contains all other noise sources. Using Eq. (5.9), it follows that

$$\beta_1 = \frac{A}{q^2} (aC_{\text{tot}}^2 + \tau_d \tau_i q I_{\text{ls}}) \quad (\text{C.3})$$

---

<sup>1</sup>This appendix has been published as part of M. C. Maas, D. R. Schaart, D. J. van der Laan, H. T. van Dam, J. Huizenga, J. C. Brouwer, P. Bruyndonckx, C. Lemaître and C. W. E. van Eijk, “Signal to noise ratio of APD-based monolithic scintillator detectors for high resolution PET,” *IEEE Transactions on Nuclear Science*, vol. 55, pp. 842–852, 2008.

Table C.1: Estimated noise parameters in the fast amplifier branch for a single channel.

$a$ (V <sup>2</sup> /Hz)	$C_{\text{tot}}$ (pF)	$I_{\text{ls}}$ (nA)	$I_{\text{lb}}$ (nA)	$\beta_1$	$\beta_2$
$1.1 \cdot 10^{-19}$	26	0.4	0.02	$2.3 \cdot 10^{-32}$	$1.8 \cdot 10^{-37}$

and

$$\beta_2 = \frac{A\tau_d\tau_i I_{\text{lb}}}{q}. \quad (\text{C.4})$$

For  $\tau_d = 100$  ns and  $\tau_i = 2$  ns, Eq. (C.2) results in  $A = 2.9 \cdot 10^8$  s<sup>-2</sup>. In Table C.1, estimates of the noise parameters of a single channel are listed. The parameter  $a$  was obtained using Eq. (5.7), taking  $\Gamma = 0.7$ ,  $T = 300$  K and  $g_m = 50$  mS. The total capacitance  $C_{\text{tot}}$  is the sum of  $C_{\text{APD}}$ ,  $C_{\text{FET}}$ ,  $C_f$ ,  $C_{\text{tst}}$  and  $C_{\text{stray}}$ . The APD capacitance  $C_{\text{APD}}$  and the FET gate-source capacitance  $C_{\text{FET}}$  are both approximately 10 pF, the CSP feedback capacitance  $C_f = 1.4$  pF and the test capacitance  $C_{\text{tst}} = 1.80$  pF. Assuming a stray capacitance of 3 pF, this results in  $C_{\text{tot}} = 26$  pF. The surface and bulk leakage currents were estimated at 0.4 and 0.02 nA, respectively [86]. The resulting values of  $\beta_1$  and  $\beta_2$  are also listed in Table C.1. It is clear that  $\beta_2 \ll \beta_1$ , a result that is not affected by the omission of  $1/f$  noise components from the analysis, as these would have been included in  $\beta_1$ .



# Bibliography

- [1] D. Townsend, T. Beyer, P. Kinahan, T. Brun, R. Roddy, R. Nutt and L. Byars, "The SMART scanner: a combined PET/CT tomograph for clinical oncology," in *Nuclear Science Symposium, 1998. Conference Record. 1998 IEEE*, vol. 2, pp. 1170–1174 vol.2, 1998.
- [2] Y. Shao, K. Farahani, R. B. Slates, R. W. Silverman, K. Meadors, A. Bowery and S. Siegel, "Development of a PET detector system compatible with MRI/NMR systems," *IEEE Transactions on Nuclear Science*, vol. 44, pp. 1167–1171, 1997.
- [3] Y. Shao, S. R. Cherry, K. Farahani, K. Meadors, S. Siegel, R. W. Silverman and P. K. Marsden, "Simultaneous PET and MR imaging," *Physics in Medicine and Biology*, vol. 42, pp. 1965–1970, 1997.
- [4] C. Catana, Y. B. Wu, M. S. Judenhofer, J. Y. Qi, B. J. Pichler and S. R. Cherry, "Simultaneous acquisition of multislice PET and MR images: Initial results with a MR-compatible PET scanner," *Journal of Nuclear Medicine*, vol. 47, pp. 1968–1976, 2006.
- [5] K. Wienhard, M. Dahlbom, L. Eriksson, C. Michel, T. Bruckbauer, U. Pietrzyk and W. D. Heiss, "The ECAT EXACT HR - performance of a new high-resolution positron scanner," *Journal of Computer Assisted Tomography*, vol. 18, pp. 110–118, 1994.
- [6] M. Defrise, P. E. Kinahan, D. W. Townsend, C. Michel, M. Sibomana and D. F. Newport, "Exact and approximate rebinning algorithms for 3-D PET data," *IEEE Transactions on Medical Imaging*, vol. 16, pp. 145–158, 1997.
- [7] K. Lange and R. Carson, "EM reconstruction algorithms for emission and transmission tomography," *Journal Of Computer Assisted Tomography*, vol. 8, pp. 306–316, 1984.
- [8] H. M. Hudson and R. S. Larkin, "Accelerated image-reconstruction using ordered subsets of projection data," *IEEE Transactions on Medical Imaging*, vol. 13, pp. 601–609, 1994.

- [9] C. S. Levin and E. J. Hoffman, "Calculation of positron range and its effect on the fundamental limit of positron emission tomography system spatial resolution," *Physics in Medicine and Biology*, vol. 44, pp. 781–799, 1999.
- [10] S. DeBenedetti, C. Cowan, W. Konneker and H. Primakoff, "On the angular distribution of two-photon annihilation radiation," *Physical Review*, vol. 77, pp. 205–212, 1950.
- [11] Y. Jean, H. Nakinishi, L. Hao and T. Sandreczki, "Anisotropy of free-volume-hole dimensions in polymers probed by positron-annihilation spectroscopy," *Physical Review B*, vol. 42, pp. 9705–9708, 1990.
- [12] H. H. Barrett, D. W. Wilson and B. M. W. Tsui, "Noise properties of the EM algorithm. I. Theory," *Physics in Medicine and Biology*, vol. 39, pp. 833–846, 1994.
- [13] D. W. Wilson, B. M. W. Tsui and H. H. Barrett, "Noise properties of the EM algorithm. II. Monte Carlo simulations," *Physics in Medicine and Biology*, vol. 39, pp. 847–871, 1994.
- [14] J. Qi and R. Leahy, "Resolution and noise properties of MAP reconstruction for fully 3-D PET," *IEEE Transactions on Medical Imaging*, vol. 19, pp. 493–506, 2000.
- [15] S. C. Strother, M. E. Casey and E. J. Hoffman, "Measuring PET scanner sensitivity: relating countrates to image signal-to-noise ratios using noise equivalent counts," *IEEE Transactions on Nuclear Science*, vol. 37, pp. 783–788, 1990.
- [16] J. S. Karp, M. E. Daube-Witherspoon, E. J. Hoffman *et al.*, "Performance standards in positron emission tomography," *The Journal of Nuclear Medicine*, vol. 12, pp. 2342–2350, 1991.
- [17] Y. F. Yang, Y. C. Tai, S. Siegel, D. F. Newport, B. Bai, Q. Z. Li, R. M. Leahy and S. R. Cherry, "Optimization and performance evaluation of the MicroPET II scanner for in vivo small-animal imaging," *Physics in Medicine and Biology*, vol. 49, pp. 2527–2545, 2004.
- [18] D. Clément, R. Frei, J. Loude and C. Morel, "Development of a 3D position sensitive scintillation detector using neural networks," in *IEEE Nuclear Science Symposium and Medical Imaging Conference Record*, vol. 3, pp. 1448–1452, IEEE, 1998.
- [19] P. Bruyndonckx, S. M. A. Léonard, J. Liu, S. P. K. Tavernier, P. Szupryczynski and A. Fedorov, "Study of spatial resolution and depth of interaction of APD-based PET detector modules using light sharing schemes," *IEEE Transactions on Nuclear Science*, vol. 50, pp. 1415–1419, 2003.

- [20] D. J. van der Laan, *Modelling monolithic scintillation detectors for positron emission tomography*, Ph.D. thesis, Delft University of Technology, 2008.
- [21] N. L. Christensen, B. E. Hammer, B. G. Heil and K. Fetterly, "Positron emission tomography within a magnetic-field using photomultiplier tubes and lightguides," *Physics in Medicine and Biology*, vol. 40, pp. 691–697, 1995.
- [22] A. P. Jeavons, R. A. Chandler and C. A. R. Dettmar, "A 3D HIDAC-PET camera with sub-millimetre resolution for imaging small animals," *IEEE Transactions on Nuclear Science*, vol. 46, pp. 468–473, 1999.
- [23] V. Chepel, V. Solovov, J. van der Marel, M. I. Lopes, P. Crespo, L. Janeiro, D. Santos, R. F. Marques and A. J. P. L. Policarpo, "The liquid Xenon detector for PET: Recent results," *IEEE Transactions on Nuclear Science*, vol. 46, pp. 1038–1044, 1999.
- [24] Y. Okada, T. Takahashi, G. Sato, S. Watanabe, K. Nakazawa, K. Mori and K. Makishima, "CdTe and CdZnTe detectors for timing measurements," *IEEE Transactions on Nuclear Science*, vol. 49, pp. 1986–1992, 2002.
- [25] A. Drezet, O. Monnet, F. Mathy, G. Montemont and L. Verger, "CdZnTe detectors for small field of view positron emission tomographic imaging," *Nuclear Instruments and Methods in Physics Research A*, vol. 571, pp. 465–470, 2007.
- [26] C. van Eijk, "Inorganic scintillators in medical imaging," *Physics in Medicine and Biology*, vol. 47, pp. R85–R106, 2002.
- [27] J. S. Huber, W. W. Moses, W. F. Jones and C. C. Watson, "Effect of lu-176 background on singles transmission for LSO-based PET cameras," *Physics in Medicine and Biology*, vol. 47, pp. 3535–3541, 2002.
- [28] E. J. Hoffman, M. E. Phelps, N. A. Mullani, C. S. Higgins and M. M. TerPogossian, "Design and performance-characteristics of a whole-body positron transaxial tomograph," *Journal Of Nuclear Medicine*, vol. 17, pp. 493–502, 1976.
- [29] C. L. Melcher and J. S. Schweitzer, "Cerium-doped lutetium oxyorthosilicate: a fast, efficient new scintillator," *IEEE Transactions on Nuclear Science*, vol. 39, pp. 502–502, 1992.
- [30] *Hamamatsu Technical Data Sheet R7600U-200-M4*, 2008.
- [31] *Hamamatsu Technical Data Sheet R3292-02*, 1998.
- [32] *Hamamatsu Technical Data Sheet R2486-01*, 2001.

- [33] R. Pani, A. Pergola, R. Pellegrini, A. Soluri, G. DeVincentis, S. Filippi, G. Di-Domenico, A. DelGuerra and F. Scopinaro, "New generation position-sensitive PMT for nuclear medicine imaging," *Nuclear Instruments & Methods In Physics Research Section A-Accelerators Spectrometers Detectors And Associated Equipment*, vol. 392, pp. 319–323, 1997.
- [34] H. Kyushima, H. Shimoi, A. Atsumi, M. Ito, K. Oba and Y. Yoshizawa, "The development of flat panel pmt," in *Nuclear Science Symposium Conference Record, 2000 IEEE*, vol. 1, pp. 7/3–7/7 vol.1, 2000.
- [35] J. de Haas, P. Dorenbos and C. van Eijk, "Measuring the absolute light yield of scintillators," *Nuclear Instruments and Methods in Physics Research A*, vol. 537, pp. 97–100, 2005.
- [36] B. J. Pichler, M. S. Judenhofer, C. Catana, J. H. Walton, M. Kneilling, R. E. Nutt, S. B. Siegel, C. D. Claussen and S. R. Cherry, "Performance test of an LSO-APD detector in a 7-T MRI scanner for simultaneous PET/MRI," *Journal of Nuclear Medicine*, vol. 47, pp. 639–647, 2006.
- [37] J.-B. Mosset, *Développement d'un module de détection phoswich LSO/LuYAP pour le prototype de caméra à positrons ClearPET*, Ph.D. thesis, Ecole Polytechnique Fédérale de Lausanne, 2006.
- [38] R. J. McIntyre, "Multiplication noise in uniform avalanche diodes," *IEEE Transactions on Electron Devices*, vol. 13, pp. 164–168, 1966.
- [39] R. McIntyre, "The distribution of gains in uniformly multiplying avalanche photodiodes: theory," *Electron Devices, IEEE Transactions on*, vol. 19, pp. 703–713, 1972.
- [40] K. M. van Vliet, L. M. Rucker and A. Friedmann, "Theory of carrier multiplication and noise in avalanche devices. II. Two-carrier processes," *IEEE Transactions on Electron Devices*, vol. ED-26(5), pp. 752–764, 1979.
- [41] W. Shockley and W. T. Read, "Statistics of the recombinations of holes and electrons," *Physical Review*, vol. 87, pp. 835–842, 1952.
- [42] C. Allier, *Micromachined Si-well scintillator pixel detectors*, Ph.D. thesis, Delft University of Technology, 2001.
- [43] P. D. Cutler, S. R. Cherry, E. J. Hoffman, W. M. Digby and M. E. Phelps, "Design-features and performance of a PET system for animal research," *Journal of nuclear medicine*, vol. 33, pp. 595–604, 1992.
- [44] S. R. Cherry, Y. Shao, R. W. Silverman *et al.*, "MicroPET: A high resolution PET scanner for imaging small animals," *IEEE Transactions on Nuclear Science*, vol. 44, pp. 1161–1166, 1997.

- [45] A. F. Chatziioannou, S. R. Cherry, Y. P. Shao, R. W. Silverman, K. Meadors, T. H. Farquhar, M. Pedarsani and M. E. Phelps, "Performance evaluation of MicroPET: A high-resolution lutetium oxyorthosilicate PET scanner for animal imaging," *Journal of Nuclear Medicine* Chatziioannou 1999, vol. 40, pp. 1164–1175, 1999.
- [46] Y. C. Tai, A. F. Chatziioannou, S. Siegel, J. Young, D. Newport, R. N. Goble, R. E. Nutt and S. R. Cherry, "Performance evaluation of the MicroPET P4: a PET system dedicated to animal imaging," *Physics in Medicine and Biology*, vol. 46, pp. 1845–1862, 2001.
- [47] C. Knoess, S. Siegel, A. Smith *et al.*, "Performance evaluation of the MicroPET R4 PET scanner for rodents," *European Journal of Nuclear Medicine and Molecular Imaging*, vol. 30, pp. 737–747, 2003.
- [48] Y. C. Tai, A. F. Chatziioannou, Y. Yongfeng, R. W. Silverman, K. Meadors, S. Siegel, D. F. Newport, J. R. Stickel and S. R. Cherry, "MicroPET II: design, development and initial performance of an improved MicroPET scanner for small-animal imaging," *Physics in Medicine and Biology*, vol. 49, pp. 1519–1539, 2003.
- [49] Y. C. Tai, A. Ruangma, D. Rowland, S. S., D. F. Newport, P. L. Chow and R. Laforest, "Performance evaluation of the MicroPET Focus: a third generation MicroPET scanner dedicated to animal imaging," *The Journal of Nuclear Medicine*, vol. 46, pp. 455–463, 2005.
- [50] J. Qi, R. M. Leahy, S. R. Cherry, A. Chatziioannou and T. H. Farquhar, "High-resolution 3D Bayesian image reconstruction using the microPET small-animal scanner," *Physics in Medicine and Biology*, vol. 43, pp. 1001–1013, 1998.
- [51] N. Orita, H. Murayama, H. Kawai, N. Inadama and T. Tsuda, "Three-dimensional array of scintillation crystals with proper reflector arrangement for a depth of interaction detector," *IEEE Transactions on Nuclear Science*, vol. 52, pp. 8–14, 2005.
- [52] M. Abreu, J. Aguiar, F. Almeida *et al.*, "Design and evaluation of the Clear-PEM scanner for positron emission mammography," *IEEE Transactions on Nuclear Science*, vol. 53, pp. 71–77, 2006.
- [53] K. Ziemons, E. Auffray, R. Barbier *et al.*, "The ClearPET (TM) project: development of a 2nd generation high-performance small animal PET scanner," *Nuclear Instruments and Methods in Physics Research A*, vol. 537, pp. 307–311, 2005.
- [54] K. Ziemons, R. Achten, E. Auffray *et al.*, "The ClearPET Neuro scanner: a dedicated LSO/LuYAP phoswich small animal PET scanner," in *IEEE Nuclear Science Symposium and Medical Imaging Conference Record*, vol. 4, pp. 2430–2433, 2004.

- [55] M. Rey, J.-M. Vieira, J.-B. Mosset, M. Moulin Sallanon, P. Millet, J.-F. Loude and C. Morel, "Measured and simulated specifications of Lausanne ClearPET scanner demonstrator," in *Nuclear Science Symposium Conference Record, 2005 IEEE*, vol. 4, pp. 2070–2073, 2005.
- [56] O. Devroede, S. Tavernier, C. Lemaître, M. Krieguer and P. Bruyndonckx, "Results obtained with the ClearPET(TM) Rodent small animal PET scanner," in *EuroMedIm, 1st European Conference on Molecular Imaging Technology*, 2006.
- [57] P. S. Roldan, E. Chereul, O. Dietzel *et al.*, "Raytest ClearPET (tm), a new generation small animal PET scanner," *Nuclear Instruments & Methods in physics research A*, vol. 571, pp. 498–501, 2007.
- [58] C. Labbé, K. Thielemans, D. Belluzzo *et al.*, "An object-oriented library for 3D PET reconstruction using parallel computing," in H. Evers, G. Glombitza, T. Lehmann and H. Meinzer (Eds.), *Bildverarbeitung für die Medizin 1999: Algorithmen - Systeme - Anwendungen*, Informatik Aktuell, p. 268, Springer Verlag, 1999.
- [59] R. Lecomte, J. Cadorette, P. Richard, S. Rodrique and D. Rouleau, "Design and engineering aspects of a high resolution positron tomograph for small animal imaging," *IEEE Transactions on Nuclear Science*, vol. 41, pp. 1446–1452, 1994.
- [60] C. Woody, A. Kriplani, P. O'Connor *et al.*, "RatCAP: a small, head-mounted PET tomograph for imaging the brain of an awake RAT," *Nuclear Instruments & Methods in Physics Research Section A*, vol. 527, pp. 166–170, 2004.
- [61] D. P. McElroy, W. Pimpl, B. J. Pichler, M. Rafecas, T. Schuler and S. I. Ziegler, "Characterization and readout of MADPET-II detector modules: validation of a unique design concept for high resolution small animal PET," *IEEE Transactions on Nuclear Science*, vol. 52, pp. 199–204, 2005.
- [62] B. J. Pichler, W. Pimpl, W. Buttler, L. Kotoulas, G. Boning, M. Rafecas, E. Lorenz and S. I. Ziegler, "Integrated low-noise low-power fast charge-sensitive preamplifier for avalanche photodiodes in JFET-CMOS technology," *IEEE Transactions on Nuclear Science*, vol. 48, pp. 2370–2374, 2001.
- [63] V. C. Spanoudaki, I. Torres-Espallardo, M. Rafecas and S. I. Ziegler, "Performance evaluation of MADPET-II, a small animal dual layer LSO-APD PET scanner with individual detector read out and depth of interaction information," *Journal of Nuclear Medicine*, vol. 48, p. 39P, 2007.
- [64] M. Rafecas, G. Boning, B. J. Pichler, E. Lorenz, M. Schwaiger and S. I. Ziegler, "A monte carlo study of high-resolution PET with granulated dual-layer detectors," *IEEE Transactions on Nuclear Science*, vol. 48, pp. 1490–1495, 2001.

- [65] B. J. Pichler, F. Bernecker, G. Boning, M. Rafecas, W. Pimpl, M. Schwaiger, E. Lorenz and S. I. Ziegler, "A  $4 \times 8$  APD array, consisting of two monolithic silicon wafers, coupled to a 32-channel LSO matrix for high-resolution PET," *IEEE Transactions on Nuclear Science*, vol. 48, pp. 1391–1396, 2001.
- [66] J. F. Pratte, G. De Geronimo, S. Junnarkar *et al.*, "Front-end electronics for the RatCAP mobile animal PET scanner," *IEEE Transactions on Nuclear Science*, vol. 51, pp. 1318–1323, 2004.
- [67] J. Varela, "A PET imaging system dedicated to mammography," *Radiation Physics and Chemistry*, vol. 76, pp. 347–350, 2007.
- [68] T. M. Cover and P. E. Hart, "Nearest neighbor pattern classification," *IEEE Transactions on Information Theory*, vol. IT13, pp. 21–27, 1967.
- [69] R. Slates, A. F. Chatziioannou, B. Fehlberg, T. Lee and S. R. Cherry, "Chemical polishing of LSO crystals to increase light output," in *IEEE Nuclear Science Symposium and Medical Imaging Conference Record*, vol. 2, pp. 939–942, IEEE, 1999.
- [70] D. J. van der Laan, M. C. Maas, D. R. Schaart, P. Bruyndonckx, S. Léonard and C. W. E. van Eijk, "Using Cramér-Rao theory combined with Monte Carlo simulations for the optimization of monolithic scintillator PET detectors," *IEEE Transactions on Nuclear Science*, vol. 53, pp. 1063–1070, 2006.
- [71] M. C. Maas, D. J. van der Laan, D. R. Schaart, J. Huizenga, J. C. Brouwer, P. Bruyndonckx, S. Léonard, C. Lemaître and C. W. E. van Eijk, "Experimental characterization of monolithic-crystal small animal PET detectors read out by APD arrays," *IEEE Transactions on Nuclear Science*, vol. 53, pp. 1071–1077, 2006.
- [72] P. Bruyndonckx, S. M. A. Léonard, S. P. K. Tavernier, C. Lemaître, O. Devroede, Y. Wu and M. Krieguer, "Neural network-based position estimators for PET detectors using monolithic LSO blocks," *IEEE Transactions on Nuclear Science*, vol. 51, pp. 2520–2525, 2004.
- [73] D. J. van der Laan, M. C. Maas, H. W. A. M. de Jong, D. R. Schaart, P. Bruyndonckx, C. Lemaître and C. W. E. van Eijk, "Simulated performance of a small-animal PET scanner based on monolithic scintillation detectors," *Nuclear Instruments and Methods in Physics Research A*, vol. 571, pp. 227–330, 2007.
- [74] T. Tsuda, H. Murayama, K. Kitamura, T. Yamaya, E. Yoshida, T. Omura, H. Kawai, N. Inadama and N. Orita, "A four-layer depth of interaction detector block for small animal PET," *IEEE Transactions on Nuclear Science*, vol. 51, pp. 2537–2542, 2004.

- [75] J. Seidel, J. J. Vaquero and M. V. Green, "Resolution uniformity and sensitivity of the NIH ATLAS small animal PET scanner: comparison to simulated LSO scanners without depth-of-interaction capability," *IEEE Transactions on Nuclear Science*, vol. 50, pp. 1347–1351, 2003.
- [76] S. Surti, J. S. Karp, A. E. Perkins, R. Freifelder and G. Mühllehner, "Design evaluation of A-PET: a high sensitivity animal PET camera," *IEEE Transactions on Nuclear Science*, vol. 50, pp. 1357–1363, 2003.
- [77] J. A. Correia, C. A. Burnham, D. Kaufman and A. J. Fischman, "Development of a small animal PET imaging device with resolution approaching 1mm," *IEEE Transactions on Nuclear Science*, vol. 46, pp. 631–635, 1999.
- [78] S. Weber, A. Bauer, H. Herzog, F. Kehren, H. Mühlensiepen, J. Vogelbruch, H. H. Coenen, K. Zilles and H. Halling, "Recent results of the TierPET scanner," in *IEEE Nuclear Science Symposium and Medical Imaging Conference Record*, vol. 3, pp. 1603–1607, IEEE, Seattle, WA, USA, 1999.
- [79] A. Del Guerra, G. Di Domenico, M. Scandola and G. Zavatti, "High spatial resolution small animal YAP-PET," *Nuclear Instruments and Methods in Physics Research A*, vol. 409, pp. 537–541, 1998.
- [80] P. M. Bloomfield, R. Myers, S. P. Hume, T. J. Spinks, A. A. Lammertsma and T. Jones, "Three-dimensional performance of a small-diameter positron emission tomograph," *Physics in Medicine and Biology*, vol. 42, pp. 389–400, 1997.
- [81] R. Lecomte, J. Cadorette, S. Rodrigue, D. Lapointe, D. Rouleau, M. Bentourkia, R. Yao and P. Msaki, "Initial results from the Sherbrooke avalanche photodiode positron tomograph," *IEEE Transactions on Nuclear Science*, vol. 43, pp. 1952–1957, 1996.
- [82] J. Birks, *The theory and practice of scintillation counting*, Pergamon press, 1964.
- [83] *Geant4 user's guide for application developers*, geant4 7.1 june 2005 edn., 2005.
- [84] E. Gatti, P. F. Manfredi, M. Sampietro and V. Speziali, "Suboptimal filtering of 1/f-noise in detector charge measurements," *Nuclear Instruments & Methods in Physics Research Section A*, vol. 297, pp. 467–478, 1990.
- [85] G. Bertuccio and A. Pullia, "A method for the determination of the noise parameters in preamplifying systems for semiconductor radiation detectors," *Review of Scientific Instruments*, vol. 64, pp. 3294–3298, 1993.
- [86] J. B. Mosset, S. Saladino, J. F. Loude and C. Morel, "Characterisation of arrays of avalanche photodiodes for small animal positron emission tomography," *Nuclear Instruments & Methods in Physics Research Section A*, vol. 504, pp. 325–330, 2003.



- [87] M. Moszynski and B. Bengtson, "Status of timing with plastic scintillation detectors," *Nuclear Instruments and Methods*, vol. 158, pp. 1–31, 1979.
- [88] C. Fiorini, A. Gola, A. Longoni, F. Perotti and L. Struder, "Timing properties of silicon drift detectors for scintillation detection," *IEEE Transactions on Nuclear Science*, vol. 51, pp. 1091–1097, 2004.
- [89] M. C. Maas, D. J. van der Laan, C. W. E. van Eijk, P. Bruyndonckx, C. Lemaître and D. R. Schaart, "Model analysis of the point spread function of monolithic scintillator PET detectors," To be published.
- [90] D. J. van der Laan, D. R. Schaart, M. C. Maas, P. Bruyndonckx, C. Lamaitre and C. W. E. van Eijk, "Spatial resolution in position-sensitive scintillation detectors: statistics and noise," 2008, to be submitted.
- [91] M. C. Maas, D. J. van der Laan, D. R. Schaart, J. Huizenga, J. C. Brouwer, P. Bruyndonckx, S. Léonard, C. Lemaître and C. W. E. van Eijk, "Experimental characterization of novel small animal PET detector modules based on scintillation crystal blocks read out by APD arrays," in *Nuclear Science Symposium Conference Record, 2004 IEEE*, vol. 5, pp. 2942–2946, 2004.
- [92] J. Boisvert, J. Montroy, L. Jostad, B. Zhou and M. Szawlowski, "Improved large-area avalanche photodiodes for scintillation detection in calorimetry," in *Nuclear Science Symposium, 1996. Conference Record., 1996 IEEE*, vol. 1, pp. 16–20 vol.1, 1996.
- [93] M. Goyot, B. Ille, P. Lebrun and J. P. Martin, "Performances of a preamplifier silicon photodiode readout system associated with large BGO crystal scintillators," *Nuclear Instruments and Methods in Physics Research A*, vol. 263, pp. 180–187, 1988.
- [94] M. Kapusta, P. Crespo, D. Wolski, M. Moszynski and W. Enghardt, "Hamamatsu S8550 APD arrays for high-resolution scintillator matrices readout," *Nuclear Instruments & Methods in Physics Research Section A*, vol. 504, pp. 139–142, 2003.
- [95] P. Dorenbos, J. T. M. de Haas and C. W. E. van Eijk, "Non-proportionality in the scintillation response and the energy resolution obtainable with scintillation crystals," *Nuclear Science, IEEE Transactions on*, vol. 42, pp. 2190–2202, 1995.
- [96] B. Carrigo, "Quality control of APDs," LIP, Lisbon, Portugal, 2006, private communication.
- [97] J. P. Pansart, "Avalanche photodiodes for particle detection," *Nuclear Instruments & Methods in Physics Research Section A*, vol. 387, pp. 186–193, 1997.
- [98] M. Moszynski, M. Szawlowski, M. Kapusta and M. Balcerzyk, "Large area avalanche photodiodes in scintillation and X-rays detection," *Nuclear Instruments & Methods in Physics Research Section A*, vol. 485, pp. 504–521, 2002.

- [99] A. Ochi, Y. Nishi and T. Tanimori, "Study of a large area avalanche photodiode as a fast photon and a soft X-ray detector," *Nuclear Instruments & Methods in Physics Research Section A*, vol. 378, pp. 267–274, 1996.
- [100] S. Agostinelli, J. Allison, K. Amako *et al.*, "GEANT4 - a simulation toolkit," *Nuclear Instruments and Methods in Physics Research A*, vol. 506, pp. 250–303, 2003.
- [101] S. Jan, G. Santin, D. Strul *et al.*, "GATE: a simulation toolkit for PET and SPECT," *Physics in Medicine and Biology*, vol. 49, pp. 4543–4561, 2004.
- [102] M. C. Maas, D. R. Schaart, D. J. van der Laan, H. T. van Dam, J. Huizenga, J. C. Brouwer, P. Bruyndonckx, C. Lemaître and C. W. E. van Eijk, "Signal to noise ratio of APD-based monolithic scintillator detectors for high resolution PET," *IEEE Transactions on Nuclear Science*, vol. 55, pp. 842–852, 2008.
- [103] B. J. Pichler, E. Lorenz, R. Mirzoyan, W. Pimpl, F. Roder, M. Schwaiger and S. I. Ziegler, "Performance test of a LSO-APD PET module in a 9.4 Tesla magnet," in *IEEE Nuclear Science Symposium and Medical Imaging Conference Record*, vol. 2, pp. 1237–1239, IEEE, 1997.
- [104] V. C. Spanoudaki, D. P. McElroy and S. I. Ziegler, "An analog signal processing ASIC for a small animal LSO-APD PET tomograph," *Nuclear Instruments and Methods in Physics Research A*, vol. 564, pp. 451–462, 2006.
- [105] E. Albuquerque, P. Bento, C. Leong *et al.*, "The Clear-PEM electronics system," *Ieee Transactions On Nuclear Science*, vol. 53, pp. 2704–2711, 2006.
- [106] D. P. McElroy, M. Hoose, W. Pimpl, V. Spanoudaki, T. Schuler and S. I. Ziegler, "A true singles list-mode data acquisition system for a small animal PET scanner with independent crystal readout," *Physics in Medicine and Biology*, vol. 50, pp. 3323–3335, 2005.
- [107] P. Bruyndonckx, C. Lemaître, D. van der Laan, M. Maas, D. Schaart, O. Devroede, M. Krieguer and S. Tavernier, "Comparison of nonlinear position estimators for continuous scintillator detectors in PET," in *Nuclear Science Symposium Conference Record, 2006 IEEE*, 2006.
- [108] C. Lemaître, P. Bruyndonckx, O. Devroede, M. Krieguer, S. Tavernier, D. van der Laan, M. Maas and D. Schaart, "Automated calibration method for parallax corrected positioning algorithms in monolithic scintillators," in *Nuclear Science Symposium Conference Record, 2006 IEEE*, 2006.
- [109] E. V. D. van Loef, P. Dorenbos, C. W. E. van Eijk, K. Kramer and H. U. Gudel, "High-energy-resolution scintillator:  $\text{Ce}^{3+}$  activated  $\text{LaBr}_3$ ," *Applied Physics Letters*, vol. 79, pp. 1573–1575, 2001.

- [110] J. S. Karp, S. Surti, M. E. Daube-Witherspoon and G. Muehllehner, "Benefit of time-of-flight in PET: Experimental and clinical results," *Journal of Nuclear Medicine*, vol. 49, pp. 462–470, 2008.
- [111] W. W. Moses, "Recent advances and future advances in time-of-flight PET," *Nuclear Instruments and Methods in Physics Research A*, vol. 580, pp. 919–924, 2007.
- [112] P. Buzhan, B. Dolgoshein, E. Garutti *et al.*, "Timing by silicon photomultiplier: A possible application for TOF measurements," *Nuclear Instruments and Methods in Physics Research A*, vol. 567, pp. 353–355, 2006.
- [113] T. Levin, J. P. Petrucci, M. S. Portnoy and J. Rudess, "Liquid tension experiment," *Magna Carta*, 1998.
- [114] L. Györfi and Z. Györfi, "On the nonparametric estimate of *a posteriori* probabilities of simple statistical hypotheses," in I. Csiszar and P. Elias (Eds.), *Topics in Information Theory*, pp. 298–308, North-Holland, 1977.
- [115] L. Györfi and Z. Györfi, "Upper bound on asymptotic error probability of K-nearest neighbor rule for multiple classes," *IEEE Transactions on Information Theory*, vol. 24, pp. 512–514, 1978.



# Nomenclature

## List of symbols

Below follows a list of the most important symbols used in this work. Some symbols are doubly defined; their meaning should be clear from the context. Throughout the thesis, vectors and matrices are set in bold typeface, while scalar quantities are set in regular typeface. The components of subscripted vector quantities carry the same subscript as that quantity; for example:  $\mathbf{x}_b = (x_b, y_b)$ . The units of the quantities are listed where applicable. Dimensionless quantities are explicitly marked by ‘–’ symbols; symbols that do not have dimensions (such as functions) and those whose dimensions vary depending on their context have no indication of units.

Symbol	Unit	Description
$\alpha^2$	–	Excess scintillation photon variance factor
$\alpha, \beta$	$\text{m}^{-1}$	Ionisation coefficients for electrons and holes
$\beta_1$	–	Combined components of electronic noise not amplified in APD
$\beta_2$	–	Component of electronic noise amplified in APD
$\varphi$	rad	azimuthal angle
$\gamma_0$	–	spatial distribution of energy deposition centroids for zero-width photon beam
$\gamma_{0,r}$	–	$\gamma_0$ in reference data
$\gamma_{0,t}$	–	$\gamma_0$ in test data
$\gamma_b$	–	spatial distribution of energy deposition centroids for realistic photon beam
$\gamma_{b,r}$	–	$\gamma_b$ in reference data
$\gamma_{b,t}$	–	$\gamma_b$ in test data
$\eta$	–	Photon detection efficiency
$\lambda$	m	Wavelength
$\mu$	$\text{m}^{-1}$	Total attenuation coefficient
$\mu_p$	$\text{m}^{-1}$	Attenuation coefficient for photoelectric absorption
$\mu_C$	$\text{m}^{-1}$	Attenuation coefficient for Compton interaction
$\theta$	rad	polar angle of incidence

$\rho$	$\text{kg/m}^3$	Density
$\sigma$		Standard deviation
$\sigma_{PSF}^*$	mm	PSF width expressed as sample standard deviation of the histogram calculated using bins with $> 1\%$ of the peak amplitude
$\sigma_A$	ns	Timing uncertainty of APD
$\sigma_P$	ns	Timing uncertainty of PMT
$\tau$	$\mu\text{s}$	Shaping time constant
$\tau_d$	ns	Differentiation time constant of TFA
$\tau_i$	ns	Integration time constant of TFA
$\Gamma$	–	FET channel form factor
$\Sigma$		Covariance matrix of Gaussian distribution $N_\Sigma$
$\Upsilon$		PSF contribution due to discretisation of reference coordinates
$\Phi$	$\text{s}^{-1}$	Photon flux
$a$	$\text{V}^2/\text{Hz}$	coefficient of series white noise
$a_f$	$\text{V}^2$	coefficient of series $1/f$ noise
$b$	$\text{A}^2/\text{Hz}$	coefficient of parallel white noise
$b_f$	$\text{C}^2$	coefficient of parallel $f$ -proportional noise
$b$	–	Background contribution to PSF for a single test coordinate
$d_b$	mm	Beam diameter (FWHM)
$d_{b,r}$	mm	Beam diameter in reference data (FWHM)
$d_{b,t}$	mm	Beam diameter in test data (FWHM)
$g_m$	$\text{A/V}$	FET transconductance
$k_b$	$\text{J/K}$	Boltzmann's constant ( $\approx 1.38 \cdot 10^{-23} \text{ J/K}$ )
$n_{\text{ref}}$	–	Number of reference events per beam position
$q$	C	Elementary charge ( $\approx 1.602 \cdot 10^{-19} \text{ C}$ )
$r$		Radial coordinate
$x, y$		Cartesian coordinates
$x', y'$		Cartesian coordinates projected on LOR
$\mathbf{x}_b, \hat{\mathbf{x}}_b$		True and estimated beam position
$\mathbf{x}_c$		Energy deposition centroid coordinate
$\mathbf{x}'_c$		Energy deposition centroid coordinate corresponding to measured light distribution
$\mathbf{x}_e, \hat{\mathbf{x}}_e$		True and estimated entry point positions
$\mathbf{x}_r$		Beam position of a reference event
$\Delta x_r, \Delta y_r$	mm	$x$ and $y$ spacing between adjacent coordinates in reference data
$\mathbf{x}_t$		Beam position of a test event
$A_1 - A_3$	–	Constants characteristic of amplifier shaping network
$B$	–	Background contribution to PSF for a set of test coordinates
$C_f$	F	Feedback capacitance
$C_{\text{tot}}$	F	Total input capacitance
$E_{\text{th}}$	keV	Energy threshold
$I_l$	A	Total leakage current
$I_{lb}$	A	APD bulk leakage current

$I_g$	A	FET gate leakage current
$I_{ls}$	A	APD surface leakage current
$J$	–	Excess noise factor
$L$	–	Number of nearest neighbours
$M$	–	APD gain
$N_e$	$e^-$	Number of electrons at APD output
$N_{ph}$	ph	Number of scintillation photons
$N_{ref}$	–	Total number of events in reference data set
$N_\sigma$	–	1D Gaussian distribution with standard deviation $\sigma$
$N_\Sigma$	–	2D Gaussian distribution with covariance matrix $\Sigma$
$PSF_{00}$		Point spread function for zero-width beams in both reference and test data
$PSF_{0b}$		Point spread function for a zero-width beam in the reference data and a realistic beam in the test data
$PSF_{b0}$		Point spread function for a realistic beam in the reference data and a zero-width beam in the test data
$PSF_{bb}$		Point spread function for realistic beams in both reference and test data
$\widehat{PSF}_{00}$		Estimate of $PSF_{00}$
$R$	$s^{-1}$	Rate of random coincidences
$R_f$	$\Omega$	Feedback resistance
$S$	$s^{-1}$	Rate of scattered coincidences
$S_r$		Residual sum of squares
$T$	$s^{-1}$	Rate of true coincidences
$T$	$^{\circ}C$	Temperature
$V$	V	Bias voltage
$V_{50}$	V	Bias voltage at $M = 50$
$\Delta V$	V	$V - V_{50}$
$Z_{eff}$	–	Effective atomic number

## Abbreviations

1D, 2D, 3D	1-dimensional, 2-dimensional, 3-dimensional
3D-RP	3D reprojection
ADC	Analog-to-digital converter
APD	Avalanche photodiode
ASIC	Application specific integrated circuit
BOLD	Blood oxygen level dependent
C.R.	Cramér-Rao
CFD	Constant fraction discriminator
CFOV	Centre of the field of view

CSP	Charge-sensitive preamplifier
CT	Computed tomography
DAQ	Data acquisition
DOI	Depth of interaction
ENC	Equivalent noise charge
ENF	Excess noise factor
FBP	Filtered backprojection
FDG	2-fluoro-2-deoxy-D-glucose
FET	Field effect transistor
FORE	Fourier rebinning
FOV	Field of view
FWHM	Full width at half maximum
FWTM	Full width at tenth maximum
JFET	Junction field effect transistor
LAAPD	Large area avalanche photodiode
LED	Light emitting diode
LOR	Line of response
LSB	Least significant bit
LSO	Lutetium oxyorthosilicate
LuAP	Lutetium aluminium perovskite
LYSO	Lutetium yttrium oxyorthosilicate
MC-ADC	Multi-channel analog-to-digital converter
MLEM	Maximum likelihood expectation maximisation
MRI	Magnetic resonance imaging
MRSI	Magnetic resonance spectroscopic imaging
NECR	Noise equivalent count rate
OSEM	Ordered subsets expectation maximisation
PCB	Printed circuit board
PEM	Positron emission mammography
PET	Positron emission tomography
PMMA	Polymethyl methacrylate
PMT	Photomultiplier tube
PSF	Point spread function
PS-PMT	Position-sensitive photomultiplier tube
QE	Quantum efficiency
SiPM	Silicon photomultiplier
SNR	Signal-to-noise ratio
SPECT	Single photon emission computed tomography
TAC	Time to amplitude converter
TFA	Timing filter amplifier
TOF	Time-of-flight
UV	Ultraviolet



# Summary

## **Monolithic scintillator detectors for high resolution positron emission tomography**

Positron emission tomography (PET) is a technique for imaging physiological processes *in vivo*. This is achieved by labelling specific biomolecules, designed to accumulate in locations where the process of interest is taking place, with a radioactive isotope emitting positrons. When such a radiotracer is injected into a subject, the positrons emitted annihilate with atomic electrons in the tissue surrounding the emission site. This process results in two annihilation photons with an energy of 511 keV, travelling in nearly opposite directions. This pair of photons can be collected by a ring of detectors surrounding the subject. When two such photons are detected simultaneously ('in coincidence'), it can be assumed that they originated from the same annihilation process. In that case, the locations where both photons were detected provide information on the line on which the annihilation took place (the 'line of response', LOR). By collecting a sufficiently large number of such LORs, the 3-dimensional distribution of the concentration of the radiotracer within the subject can be estimated.

Recent years have shown a marked increase of the use of PET in clinical and preclinical research. The advent of mouse genomics has caused a strong increase of the number of studies performed with this animal in preclinical biomolecular research, calling for dedicated PET systems with high spatial resolution and high sensitivity. The research presented in this thesis focuses on a new type of detector that allows a strong increase of the scanner sensitivity, while maintaining an image resolution comparable to that of modern high-resolution PET systems.

The detectors investigated in this thesis consist of a monolithic piece of scintillation material (LSO:Ce or LYSO:Ce), coupled on one or two sides to arrays of avalanche photodiodes (APDs). The entry point of an incident annihilation photon on the front surface of the detector is estimated from the distribution of scintillation light emitted in the interaction(s) of the photon with the crystal on the

APDs. This is done using a statistical computer algorithm.

The research presented in this thesis had three primary aims: (1) to experimentally characterise the spatial resolution, energy resolution and timing resolution obtainable with the detectors, in order to assess their utility in high-resolution PET systems, (2) to analyse the dependence of these detector performance on physical quantities such as the scintillator light yield and the APD gain and noise properties, in order to optimise the performance of the current detectors and to facilitate the design of future detectors based on a similar concept, and (3) to predict the performance of a small animal PET system based on these detectors.

Chapter 3 introduces the methodology that has been used throughout this thesis to characterise the detectors. A measurement setup is described which allows scanning the detectors through a narrow beam of 511 keV photons in various directions and at various angles of incidence. The beam is created using a  $^{22}\text{Na}$  positron source and a second detector in coincidence with the detector under investigation. Using the experimental setup, distributions of scintillation light over the APD arrays can be collected at known entry points of the 511 keV photons on the detector front surface. These light distributions can serve as reference data to a statistical algorithm based on the so-called nearest neighbour method, that uses these data to estimate the entry points corresponding to unknown light distributions. The spatial resolution of the detector is estimated by comparing the estimated entry points of a large set of events with their known, true entry points, and creating a histogram of the positioning errors. This histogram represents an estimate of the detector point spread function (PSF). The detector energy and timing resolutions are determined from the sum of all APD channels in each event.

An overview of the performance of the detectors is presented in Chapter 4. An intrinsic detector spatial resolution of 1.05 mm FWHM is shown to be feasible, after correction for the influence of the  $\sim 0.9$  mm FWHM measurement beam. This is comparable to the spatial resolution of detectors in modern high-resolution systems. A comparison is presented between detectors with various crystal surface finishes and readout geometries, including detectors with a trapezoidal shape. The spatial resolution measured with these detectors, which can be placed in a PET ring with a minimum of dead space, maximising the scanner sensitivity, is almost the same as with rectangular detectors. The correction for depth-of-interaction (DOI) of the annihilation photons is tested by measuring the spatial resolution as a function of the angle of incidence. The spatial resolution is found to be essentially angle-independent for angles up to  $30^\circ$ . For a scanner, this means that the usual tradeoff between detector thickness and spatial resolution is removed. The scanner sensitivity can thus be maximised without degrading

the image resolution towards the edges of the field of view (FOV). The measured energy resolutions of  $\sim 11\%$  FWHM and the coincidence timing resolution of 2.8 ns indicate that efficient rejection of scattered and random coincidences is possible with these detectors.

In Chapter 5, an analysis is presented of the influence of signal variances on the detector energy, timing and spatial resolutions. This is done by modelling the signal to noise ratio (SNR) applicable to each of these detector characteristics in terms of physical quantities such as the scintillator light yield, the APD gain and the noise characteristics of the frontend electronics. It is demonstrated that the energy resolution is mainly determined by the relative variance of the number of scintillation photons created per event, while the gain and excess noise factor of the APD and the electronic noise play a less important role. In contrast, the SNR applying to the spatial resolution is mainly determined by the APD excess noise factor and electronic noise. The timing resolution primarily depends on the scintillation light yield and the electronic noise on the timing signal. A strong dependence of the timing resolution on the APD gain is observed. This dependence is explained using a model describing the electronic noise as a function of properties of the detector-amplifier system, such as the input capacitance of the APDs and preamplifiers, leakage currents and the filters used for pulse shaping.

Chapter 6 describes an analysis of the point spread function (PSF) of the detectors. A simple model of the PSF is derived, which accounts for the spatial distribution of the energy deposited by the annihilation photons within the scintillator, as well as for the influences of statistical signal fluctuations and electronic noise. A detailed validation of the model is performed through comparison with measured detector PSFs. The model is shown to describe the measured PSFs well at the noise levels found in our experiments. It is furthermore demonstrated how the model can be used to quantify the influence of a finite-diameter test beam of annihilation photons on measured detector PSFs, and how a correction for this influence can be made. Combining this model with Monte Carlo simulations of the detectors furthermore enables a more detailed analysis of the relation between the spatial resolution and physical quantities such as the scintillator light yield and the amplification and noise characteristics of the APDs and the front-end electronics.

A study of the performance of small-animal PET systems based on monolithic scintillator detectors is presented in Chapter 7. This is done by Monte Carlo simulations using measurements of the PSFs and other detector properties as input. The scanners investigated consist of 1 or 4 rings with an inner diameter of 123.8 mm and an axial extent of 19.5 mm, each containing 32 detectors of 20 mm thick LSO. The system resolution of the 1-ring scanner is estimated in 2D, both

for ideal mathematical point sources without positron range or photon acollinearity, and for realistic  $\varnothing 0.5$  mm  $^{18}\text{F}$  sources. Very little degradation of the system resolution towards the edge of the field of view of the scanner is observed in either case. Images of a simulated  $^{18}\text{F}$ -filled micro-Derenzo hot rod phantom reconstructed with an OSEM algorithm show that rods with a diameter of 2.4 mm can be well resolved. The sensitivity for coincident detection at low count rates is estimated at 21% at the centre of the FOV of a 4-ring scanner with trapezoidally shaped detectors, substantially higher than the 3–4% reported for current state of the art systems. The NECR calculated for this system is also high, reaching 2000 kcps at an activity of 70 MBq in a  $\varnothing 36 \times 67$  mm<sup>3</sup> water-filled phantom.

The image resolution attained in this preliminary study may be improved by further optimising the currently used reconstruction algorithm, or by selecting a more sophisticated reconstruction method. Furthermore, improvements of the image resolution could be reached by optimising the detector geometry. This should be chosen such that the relative number of annihilation photons entering a detector close to the crystal edge is minimised, as the position estimation procedure is less accurate at these locations. The image quality could also be improved by removing artefacts that have been observed on the measured PSFs. An explanation for these artefacts has thus far not been found.

Building a prototype PET system based on monolithic scintillator detectors requires overcoming a number of technical challenges. An integrated solution for the front-end electronics should be designed, as well as a new data acquisition architecture. A faster algorithm should be used to estimate the entry points of the incident annihilation photons, and a method should be developed to efficiently collect reference data for this purpose. If these challenges can indeed be overcome, a PET system could be developed which produces images with a high resolution and a significantly improved signal to noise ratio compared to existing systems.

*Marnix C. Maas,  
November 2008*

# Samenvatting

## Monolithische-scintillatordetectoren voor hoge-resolutie positron emissie tomografie

Positron emissie tomografie (PET) is een techniek waarmee fysiologische processen *in vivo* in beeld kunnen worden gebracht. Daartoe worden specifieke biomoleculen, ontwikkeld om zich te verzamelen op plaatsen waar het te onderzoeken fysiologische proces plaatsvindt, verbonden met een radioactief isotoop dat positronen uitzendt. Wanneer een dergelijke radiotracer in een subject is geïnjecteerd, annihilieren de uitgezonden positronen met de atomaire elektronen in het weefsel in de omgeving van de tracer. Daarbij ontstaan twee annihilatiefotonen met een energie van 511 keV, die in vrijwel tegenovergestelde richting worden uitgezonden. Dit fotonenpaar kan worden opgevangen in een ring van detectoren rondom het subject. Wanneer twee dergelijke fotonen tegelijkertijd ('coincident') worden waargenomen, kan verondersteld worden dat ze afkomstig zijn van het zelfde annihilatieproces. In dat geval geven de locaties waar beide fotonen gedetecteerd zijn informatie over de lijn waarop de positron-electron-annihilatie heeft plaatsgevonden (de 'line of response', LOR). Met het verzamelen van een voldoende groot aantal van deze LORs kan met behulp van een computerberekening de 3-dimensionale verdeling van de concentratie van de radiotracer in het subject geschat worden.

Het gebruik van PET in klinisch en preklinisch onderzoek heeft de laatste jaren een grote vlucht genomen. Met name door de opkomst van het gebruik van muizen voor preklinisch biomoleculair onderzoek is een vraag ontstaan naar PET-systemen met een groot plaatsoplossend vermogen en een hoge gevoeligheid. Het onderzoek dat geleid heeft tot dit proefschrift richtte zich op een nieuw type detector, waarmee een sterke verbetering van de gevoeligheid van het PET-systeem gehaald kan worden, terwijl de plaatsresolutie vergelijkbaar blijft met die van moderne hoge-resolutie PET-systemen.

De detectoren die centraal staan in dit proefschrift bestaan uit een mono-

lithisch stuk scintillatiemateriaal (LSO:Ce of LYSO:Ce), dat aan een of twee kanten wordt uitgelezen door een matrix van fotodiodes met interne versterking ('avalanche photodiodes', APDs). Het intreepunt van een binnenvallend annihilatiefoton op het voorvlak van de detector wordt door middel van een statistisch computeralgoritme geschat uit de verdeling over de APDs van het scintillatielicht dat ontstaat bij de interactie(s) van dit foton met het kristal.

Het onderzoek gepresenteerd in dit proefschrift had drie primaire doelen: (1) het experimenteel karakteriseren van de plaatsresolutie, de energieresolutie en de tijdsresolutie van de detectoren om hun geschiktheid voor hoge-resolutie PET na te gaan, (2) het analyseren van de afhankelijkheid van deze detectoreigenschappen van fysische grootheden, zoals de lichtopbrengst van de scintillator en de versterkings- en ruiseigenschappen van de APDs, om de prestaties van de huidige detectoren te optimaliseren en het ontwerp van toekomstige versies van deze detectoren te vergemakkelijken, en (3) het voorspellen van de prestaties van een PET-systeem gebaseerd op dit type detectoren.

Hoofdstuk 3 behandelt de meetmethoden die gebruikt zijn in dit proefschrift. Voor de experimentele karakterisatie van de detectoren is een meetopstelling gebouwd, waarin de detectoren in verscheidene richtingen en onder verscheidene hoeken door een smalle bundel 511 keV fotonen gescand kunnen worden. De bundel wordt gecreëerd met behulp van een  $^{22}\text{Na}$ -positronenbron en een tweede detector in coïncidentie met de onderzochte detector. Met behulp van de meetopstelling kunnen verdelingen van scintillatielicht over de APDs worden opgenomen bij bekende intreepunten van de 511 keV fotonen op het detectorvoorvlak. Deze lichtverdelingen kunnen dienen als referentiedata voor een statistisch algoritme gebaseerd op de z.g. naaste-nabuurmethode, dat met behulp hiervan het intreepunt behorend bij een onbekende lichtverdeling kan schatten. De plaatsresolutie van de detector wordt bepaald door de geschatte intreepunten van een grote verzameling events te vergelijken met hun bekende, werkelijke intreepunten, en een histogram te maken van de positioneringsfouten. Dit histogram geeft een schatting van de point spread functie (PSF) van de detectoren. De energie- en de tijdsresoluties van de detectoren worden bepaald uit de som van alle APD-signalen in elk event.

In Hoofdstuk 4 wordt een overzicht gegeven van de prestaties van de detectoren. Er wordt aangetoond dat een intrinsieke plaatsresolutie van de detectoren van 1.05 mm 'full width at half maximum' (FWHM) haalbaar moet zijn, na correctie voor de invloed van de  $\sim 0.9$  mm FWHM meetbundel. Dit is vergelijkbaar met de plaatsresolutie van detectoren in moderne hoge-resolutiescanners. Een vergelijking wordt gemaakt tussen verschillende detectorontwerpen, met inbegrip van detectoren met een trapezoïde vorm. Met dergelijke detectoren, die in

een PET ring kunnen worden geplaatst met een minimum aan dode ruimte zodat de gevoeligheid van de scanner gemaximaliseerd wordt, wordt vrijwel de zelfde plaatsresolutie gemeten als met rechthoekige detectoren. De correctie voor de diepte van interactie van de annihilatiefotonen wordt getest door de plaatsresolutie te meten als functie van de hoek van inval. Er wordt gevonden dat de plaatsresolutie vrijwel onafhankelijk is van de hoek van inval, voor hoeken tot minstens  $30^\circ$ . Voor een scanner betekent dit dat de gewoonlijke afweging tussen detector-diepte en plaatsresolutie komt te vervallen. Hierdoor kan de gevoeligheid van de scanner gemaximaliseerd worden, zonder dat de resolutie van het gereconstrueerde beeld naar de rand van het beeldveld ('field of view', FOV) verslechtert. De energieresoluties van rond de 11% FWHM en tijdsresoluties van 2.8 ns voor coïncidente detectie die daarnaast zijn gemeten duiden erop dat een efficiënte onderdrukking van verstrooide en toevallige coïncidenties mogelijk is met deze detectoren.

In Hoofdstuk 5 wordt een analyse gepresenteerd van de invloed van signaalvarianties op de energie-, tijd- en plaatsresolutie van de detectoren. Dit wordt gedaan aan de hand van modellen van de signaal-ruisverhouding geldend voor elk van deze detectorkarakteristieken, in termen van fysische grootheden zoals de lichtopbrengst van de scintillator en de versterkings- en ruiseigenschappen van de APDs en het elektronische uitleessysteem. Uit de analyse volgt dat de energieresolutie van de onderzochte detectoren voornamelijk bepaald wordt door de relatieve variantie in het aantal scintillatiefotonen dat per geabsorbeerd annihilatiefoton wordt geproduceerd, terwijl de versterking en de excess noise factor van de APD en de elektronische ruis een kleinere rol spelen. In tegenstelling daarmee blijkt de signaal-ruisverhouding die betrekking heeft op de plaatsresolutie juist het sterkst bepaald te worden door de excess noise factor en de elektronische ruis. De tijdsresolutie hangt voornamelijk af van de elektronische ruis op het tijdsignaal en de lichtopbrengst van de scintillator. Er wordt waargenomen dat de tijdsresolutie sterk afhangt van de versterkingsfactor van de APDs. Dit wordt in overeenstemming gebracht met een model dat de elektronische ruis beschrijft als functie van eigenschappen van het detector-versterkersysteem, zoals de ingangscapaciteit van de APDs en voorversterkers, lekstromen en het gebruikte versterkerfilter.

Hoofdstuk 6 beschrijft een nadere analyse van de plaatsresolutie van de detectoren aan de hand van hun z.g. 'point spread function (PSF)'. Er wordt een afleiding gepresenteerd van een simpel model, dat de ruimtelijke distributie van energiedeposities die plaatsvinden bij de absorptie van een annihilatiefoton in het scintillatiekristal, en de invloeden van statistische signaalfluctuaties en elektronische ruis in rekening brengt. Een gedetailleerde validatie van dit model wordt uitgevoerd aan de hand van vergelijkingen met gemeten PSFs. Er wordt gevonden

dat het model de gemeten PSFs goed beschrijft bij de ruisniveaus die gebruikelijk zijn in onze experimenten. Verder wordt gedemonstreerd hoe het model gebruikt kan worden om de invloed van een testbundel met eindige diameter en divergentie op de gemeten PSF te kwantificeren, en hoe voor deze invloed gecorrigeerd kan worden. Combinatie van dit model met gedetailleerde Monte Carlosimulaties van de detectoren biedt de mogelijkheid om in meer detail het verband tussen de plaatsresolutie en fysische grootheden zoals de lichtopbrengst van de scintillator en de versterkings- en ruiseigenschappen van de APDs en het elektronische uitleessysteem te bestuderen.

In Hoofdstuk 7 wordt een verkennende studie gepresenteerd die is gedaan om de prestaties van hoge-resolutie PET-systemen gebaseerd op monolithische detectoren te schatten. Dit wordt gedaan met behulp van Monte-Carlosimulaties, die gemeten PSFs en andere eigenschappen van de detectoren als input gebruiken. Simulaties zijn gedaan van scanners bestaande uit 1 of 4 ringen met een binnendiameter van 123.8 mm en een axiale lengte van 19.5 mm, elk met 32 detectoren van 20 mm dik LSO. De systeemresolutie van de 1-rings scanner is geschat in 2D, zowel voor ideale mathematische puntbronnen zonder positrondracht of fotonacollineariteit, als voor realistische  $\text{Ø}0.5 \text{ mm } ^{18}\text{F}$ -bronnen. In beide gevallen werd zeer weinig verslechtering van de systeemresolutie waargenomen richting de rand van het beeldveld. Uit een 2D-beeld van een gesimuleerd micro-Derenzo hot-rod-fantoomgevuld met  $^{18}\text{F}$ , gereconstrueerd met een iteratief OSEM algoritme, blijkt dat elementen met een diameter van 2.4 mm nog goed op te lossen zijn. De gevoeligheid voor coïncidente detectie bij lage teltempi ten gevolge van een puntbron in het centrum van het FOV van een 4-rings scanner met trapezoidvormige detectoren wordt geschat op 21%, beduidend hoger dan de 3–4% die in moderne hoge-resolutiesystemen gehaald worden. Ook de NECR die geschat wordt voor dit systeem is zeer hoog, met 2000 kcps bij een activiteit van 70 MBq in een  $\text{Ø}36 \times 67 \text{ mm}^3$  water-fantoom.

De beeldkwaliteit behaald in deze verkennende studie zou wellicht verbeterd kunnen worden door het gebruikte reconstructiealgoritme verder te optimaliseren, of een geschikter reconstructiealgoritme te kiezen. Verder zou de beeldresolutie verbeterd kunnen worden door een optimalisatie van de detectorgeometrie. Deze zou zo gekozen moeten worden dat relatief minder annihilatiefotonen intreden in de buurt van een detectorrand, waar de positionering onnauwkeuriger is. Een verdere verbetering van de beeldkwaliteit kan wellicht gehaald worden door de artefacten die waargenomen zijn op de PSFs van de detectoren te verminderen. Een verklaring voor deze artefacten is echter nog niet gevonden.

Voor het bouwen van een prototype PET-scanner gebaseerd op deze detec-



toren moet nog een aantal technische uitdagingen overwonnen worden. Er moet een geïntegreerde oplossing voor de frontend-electronica ontworpen worden, evenals een nieuwe architectuur de data-acquisitie. Er zal gebruik moeten worden gemaakt van een ander, sneller algoritme om de intreepunten van de invallende fotonen te bepalen, en er moet een methode ontwikkeld worden om op efficiënte wijze referentiedata voor dit doel te vergaren. Indien deze uitdagingen inderdaad overwonnen worden, kan hiermee een scanner ontwikkeld die beelden levert met een hoge resolutie en een significant verbeterde signaal-ruisverhouding ten opzichte van gangbare systemen.

*Marnix C. Maas,  
November 2008*



# Acknowledgements

Even though traditionally this is one of the parts of a thesis that people read first, it is the last written – in the spirit of the relief that comes when the storm subsides. It is with great pleasure that I express my gratitude to the many people who have directly and indirectly contributed to the creation of this thesis.

First of all, I gratefully acknowledge my promotor Carel van Eijk for his guidance, for fruitful discussions and for his positive attitude. My second promotor, Freek Beekman, has had a stimulating influence on my progress during the final six months of writing. Freek, thank you for everything. As my supervisor, Dennis Schaart has played an essential role in my research. Dennis, I have learned a lot from you, thank you for your guidance and for all your time and effort. I reserve a special word of gratitude to Rob Hollander, for his input and his interest in my work.

Throughout my thesis research period, dr. Peter Bruyndonckx of the Free University of Brussels has always been available with helpful advice and discussions. Peter, thank you very much. Special thanks also to dr. Hugo de Jong of the University Medical Centre in Utrecht for performing the image reconstructions presented in Chapter 7.

Without any doubt, Jan van der Laan is the person who contributed most to the creation of this work. Jan, thank you very much for all the time spent together, the discussions, your advice, ideas, help, and generally for being my partner-in-crime.

Jan Huizenga and Johan de Haas, the unfathomable depths of your knowledge have been essential to any (feeble) attempt at experimentation I ever undertook during my period in the group. Thank you very much for everything. Hans Brouwer, thank you for your excellent work and all our great conversations. Many thanks also to Martijn de Boer and Folkert Geurink for all your help, and to José Buurman for your organisational support. Herman van Dam and Stefan Seifert, thank you – above all – for your many questions.

In-house workshops and design offices are a blessing for any instrumentation group. René Gommers, thank you very much for helping me design my equip-

ment. René den Oudsten, Kees Langelaan and all the others at the workshop, thank you for building it and for all your in-between time.

I would also like to extend my gratitude to my other colleagues at the institute: Danang, Greg, Pjotr, Mélanie, Mirko, Jacob, Adrie, Alastair, Romee, Pieter, Erik, Rob, Victor, Niels and David, for all the coffee and lunch table banter, volleyball karate-chops, dinners, etc. Candice, thank you very much for being the driving force behind many social (group) activities. Xander, very special thanks to you: not only for being a great colleague, but also for providing the group with its most valuable asset ever (yes, it is inflatable).

At the Netherlands Cancer Institute, I have had the pleasure of meeting a special, passionate group of people, who have shown me new perspectives on working in physics. I would first of all like to thank my supervisors Corine van Vliet and Christoph Schneider, for your support and your patience with me. Carmen, Marloes, Thijs, Ferrie, Karin, Martijn, Mine, Anke and all the others, thank you for being great colleagues and for providing such a friendly atmosphere.

Throughout the years, I have regularly stood in wonder of the great number of exceptional people that I found myself surrounded with. I feel extremely privileged to be able to call many of these people my friends.

Pepijn, thank you for your uniqueness, your generosity, for always being there when I needed you, for your ‘Abbink acties’, and for everything else. Dhiradj, thank you for being a wonderful friend, for the many excellent times shared, for being the constant factor in my Delft life, and for time and again bringing me what your name promises.

The boys & girls of the DGW group provide each other with an extraordinary sense of ‘home’, even years after having dispersed all over the country and far beyond. Bart, Freek, Michiel, Christian, Mónica, Chris, Sandra, Mark, Mathijs, Martin and Marieke, thank you for the countless (in)activities together and your warm friendship and support.

It is always a great pleasure to meet people at work who end up making the transition from colleague to friend. Enrica, your strength and persistence are as exemplary as they are beyond belief; thank you for everything. Andreas, thank you for our endless discussions which taught me to always see things from yet another point of view, and for being a great friend. Andrea and Alessandra, thank you for the nice activities, discussions, dinners, and everything else. Susana, thank you for your uncompromising originality, your friendship and support. Antonia, thank you for the many nice ‘away’ lunch chats; Thea, thank you for brightening up my early-morning moods.

Through one person, one sometimes meets many new friends: Aura, Aurèle,

Julien, François, Irene and Didier, thank you for the many excellent dinners, games, parties, jungle speed nights, Sinterklaas evenings, cooking competitions, etc. that have had a huge (positive) impact on my sanity-o-meter. Calvin, thank you very much, not only for being part of all of this as well, but also for your amazing creative input and skill. Special thanks to Steffi and Nikki, for risking life & limb in pursuit of your modelling careers. Tahira, thank you for being the instigator of all of this; thank you for helping me find, and love, my dribble, and thank you for your incredible spirit and friendship.

Luke and Janneke, your energetic and joyful way of life has always had an infectious influence on me; thank you very much. Pieter and Margriet, thank you very much for your priceless friendship and support.

The city of Delft attracts so many people from abroad that it sometimes makes you forget you're still in The Netherlands. Cristina and César, thank you for introducing me to the joys and values of the international diversity that has become such an important aspect of my life. Thank you for your warmth and invaluable friendship. Vanesa, Casper, Paul, Jorge and Aletta, thank you for your friendship and support. To the 'mafia española': Dani, Dionne, Alfonso, Alejandra, Ramón, Paloma, Iciar, Dani and all the others, thank you for the countless parties, dinners and activities enjoyed together.

PhD theses can have quite an unforgiving way of confronting people with who they themselves, and their partners, are. I am very grateful to Yohana, for all the happy times together and for everything I have learned since. To her family, for their acceptance and for the beautiful inside-view of their culture they have given me.

These acknowledgments can only end with the beginning: my family. I am very grateful to all my aunts, uncles and cousins for their love and support. Frits and Ellen, thank you for helping me through tough times; Jos en Marja, thank you for your never-ending belief.

Lieve Saskia, bedankt voor je eindeloze liefde, steun, interesse en enthousiasme. Wichor, bedankt dat je zo'n fantastische partner bent voor mijn zusje.

Lieve Mam, lieve Pap, hoe bedankt een mens zijn ouders? Met de zelfde vanzelfsprekendheid en onvoorwaardelijkheid als waarmee jullie je liefde aan ons geven.

Dank jullie wel.



# Curriculum Vitae

Marnix Maas was born on April 19, 1977 in Utrecht, The Netherlands. After obtaining his secondary school degree from the Utrechts Stedelijk Gymnasium, he started a Master's Degree in Applied Physics at the Faculty of Applied Sciences of the Delft University of Technology. It was there that his interests in imaging science were stirred, resulting in his graduation at the Optics research group of the same faculty. His Master's project focused on improving the design of a Retinal Scanning Display (RSD), a device that projects images directly into the eye using low-intensity scanning lasers. He went on to apply his optical experience at a startup company, Zernike Systems, developing a scanning-laser fundus camera, a device that creates images of the inside surface of the human eye. After a short period with Zernike Systems, he found a PhD position at the Interfaculty Reactor Institute, now Reactor Institute Delft. His research there, aimed at the development of new detectors for high-resolution positron emission tomography (PET), led to the writing of this thesis. Currently, he works at the Radiotherapy department of the Netherlands Cancer Institute – Antoni van Leeuwenhoek hospital in Amsterdam, The Netherlands. His activities there focus on the application of advanced magnetic resonance imaging (MRI) techniques in radiation therapy.

## List of publications

M. C. Maas, D. R. Schaart, D. J. van der Laan, H. T. van Dam, J. Huizenga, J. C. Brouwer, P. Bruyndonckx, C. Lemaître and C. W. E. van Eijk, "Signal to noise ratio of APD-based monolithic scintillator detectors for high resolution PET," *IEEE Trans. Nucl. Sci.*, vol. 55, pp. 842–852, 2008.

M. C. Maas, D. R. Schaart, D. J. van der Laan, P. Bruyndonckx, C. Lemaître, F. J. Beekman and C. W. E. van Eijk, "Monolithic scintillator PET detectors with intrinsic depth-of-interaction correction," *submitted for publication*.

M. C. Maas, D. J. van der Laan, C. W. E. van Eijk, P. Bruyndonckx, C. Lemaître and D. R. Schaart, "Model analysis of the point spread function of monolithic scintillator detectors for high resolution PET," *in preparation*.

D. J. van der Laan, M. C. Maas, H. W. A. M. de Jong, D. R. Schaart, P. Bruyndonckx, C. Lemaître and C. W. E. van Eijk, "Simulated performance of a small-animal PET scanner based on monolithic scintillation detectors," *Nucl. Instrum. Meth. Phys. Res. A*, vol. 571, pp. 227–330, 2007.

M. C. Maas, D. J. van der Laan, D. R. Schaart, J. Huizenga, J. C. Brouwer, P. Bruyndonckx, S. Léonard, C. Lemaître and C. W. E. van Eijk, "Experimental characterization of monolithic-crystal small animal PET detectors read out by APD arrays," *IEEE Trans. Nucl. Sci.*, vol. 53, pp. 1071–1077, 2006.

D. J. van der Laan, M. C. Maas, D. R. Schaart, P. Bruyndonckx, S. Léonard and C. W. E. van Eijk, "Using Cramér-Rao theory combined with Monte Carlo simulations for the optimization of monolithic scintillator PET detectors," *IEEE Trans. Nucl. Sci.*, vol. 53, pp. 1063–1070, 2006.

M. C. Maas, D. R. Schaart, D. J. van der Laan, H. T. van Dam, J. Huizenga, J. C. Brouwer, P. Bruyndonckx, C. Lemaître and C. W. E. van Eijk, "Signal to noise ratio of monolithic scintillator detectors for small animal PET," *2006 IEEE Nucl. Sci. Symp. Conf. Rec.*, vol. 5, pp. 3027–3031.

D. J. van der Laan, M. C. Maas, H. W. A. M. de Jong, D. R. Schaart, P. Bruyndonckx, C. Lemaître and C. W. E. van Eijk, "Spatial resolution in position-sensitive monolithic scintillation detectors," in *2006 IEEE Nucl. Sci. Symp. Conf. Rec.*, vol. 4, pp. 2506–2510.



M. C. Maas, D. J. van der Laan, D. R. Schaart, P. Bruyndonckx, C. Lemaître and C. W. E. van Eijk, “Performance of APD-based monolithic-crystal detectors for small animal PET”, *2005 IEEE Nucl. Sci. Symp. Conf. Rec.*, vol. 4, pp. 2017–2021.

M. C. Maas, D. J. van der Laan, D. R. Schaart, J. Huizenga, J. C. Brouwer, P. Bruyndonckx, S. Léonard, C. Lemaître and C. W. E. van Eijk, “Experimental characterization of novel small animal PET detector modules based on scintillation crystal blocks read out by APD arrays,” *2004 IEEE Nucl. Sci. Symp. Conf. Rec.*, vol. 5, pp. 2942–2946.





